CHARACTERIZATION OF NANOFIBERS PRODUCED BY ELECTROSPINNING FOR BIOMEDICAL APPLICATIONS

Reyda Akdemir

UNIVERSITAT ROVIRA i VIRGILI

Characterization of nanofibers produced by electrospinning for biomedical applications

Reyda Akdemir

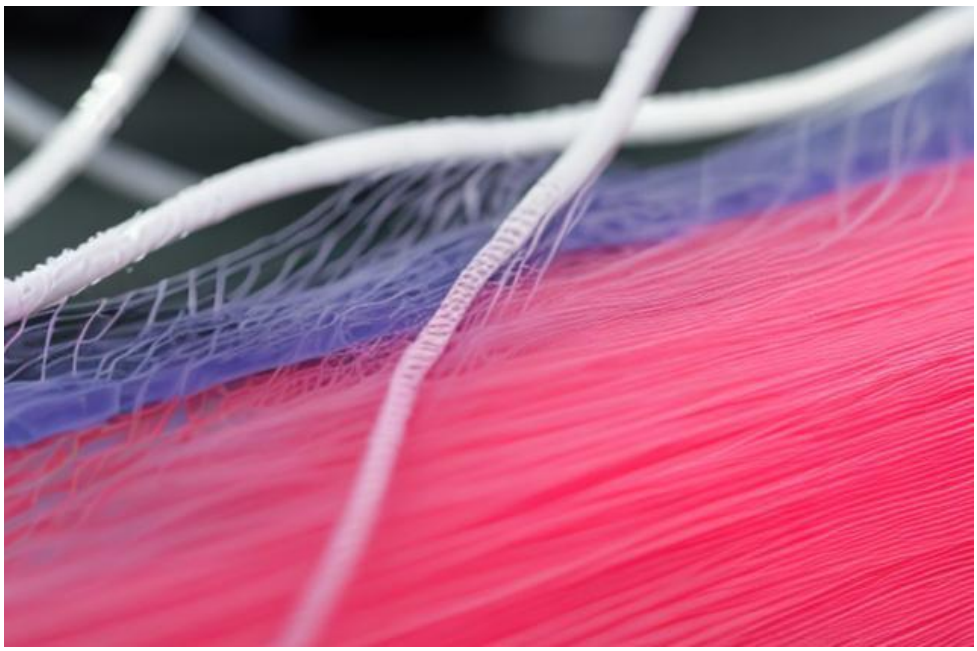

DOCTORAL THESIS

UNIVERSITAT ROVIRA I VIRGILI
CHARACTERIZATION OF NANOFIBERS PRODUCED BY ELECTROSPINNING FOR BIOMEDICAL APPLICATIONS
Reyda Akdemir

Characterization of nanofibers produced by electrospinning for biomedical applications

Reyda Akdemir

DOCTORAL THESIS

Supervised by Dr. Joan Rosell-Llompart

Tarragona, Spain

2023

The research presented in this thesis was carried out with funding from the European Union's Horizon 2020 research and innovation programme under the Marie Sklodowska-Curie grant agreeement No. 713679 and from the Universitat Rovira i Virgili URV.

UNIVERSITAT ROVIRA i VIRGILI

Department of Chemical Engineering
Droplets, intErfaces, and floWs laboratory
Campus Sescelades
Av. dels Països Catalans, 26
43007 Tarragona, Spain

FAIG CONSTAR que aquest treball, titulat "Characterization of nanofibers produced by electrospinning for biomedical applications", que presenta la Sra. Reyda Akdemir per a l'obtenció del títol de Doctor, ha estat realitzat sota la meva direcció al Departament d'Enginyeria Química d'aquesta universitat.

HAGO CONSTAR que el presente trabajo, titulado "Characterization of nanofibers produced by electrospinning for biomedical applications", que presenta la Sra. Reyda Akdemir para la obtención del título de Doctor, ha sido realizado bajo mi dirección en el Departamento de Ingeniería Química de esta universidad.

I STATE that the present study, entitled "Characterization of nanofibers produced by electrospinning for biomedical applications.", presented by Md. Reyda Akdemir for the award of the degree of Doctor, has been carried out under my supervision at the Department of Chemical Engineering of this university.

El director de la tesi doctoral

Tarragona, 1 de setembre de 2023

Joan Rosell Llompart - DNI 35039930M (TCAT)

Firmado digitalmente por Joan Rosell Llompart - DNI 35039930M (TCAT)
Fecha: 2023.08.31 22:29:29 +02'00'

Acknowledgments

First and foremost, I am immensely thankful to my supervisor, Dr. Joan Rosell-Llompart, for his unwavering support and invaluable guidance throughout the entire duration of my research. His expertise, insights, and constructive feedback have been instrumental in shaping the direction and quality of this thesis. I also thank Dr. Silvia De la Flor López for sharing her expertise and equipment for tensile testing. A special mention goes to Dr. Anthony Weiss who hosted me in his tissue engineering group at the University of Sydney. Thank you for giving me an opportunity in your lab and for sharing your knowledge with me.

I am also thankful to my colleagues and DEW members who provided stimulating discussions and shared their insights, especially Dr. Nikolas Sochorakis; your help will not be forgotten.

My appreciation extends to my mom for supporting my career and being my best friend, and to my brother who always helped me in every possible way. I also thank my beloved friend Camilo for reading my thesis with his journalist's eyes and giving me feedback on the structure.

Last but not least, I am grateful to the master's students I supervised during my PhD: Havvagul Ermis, Tamer Ben Hassan, and Paula Martinez. I learned a lot with them, and their contributions were integral to the success of my work.

Thank you.

List of Events Attended

1. SantanderX | Launch-Babson College-Entrepreneurship school (April 11-June 27, 2023) *(Boston, USA)*
2. Proof of Concept Training Program 2023 (January-May) *(Barcelona, Spain)*
3. PuzzleX "Quantum World" attendance 2022 *(Barcelona, Spain)*
4. Secondment-Research Stay at the University of Sydney (2021) under Prof. Anthony Weiss (Weiss Lab) *(Sydney, Australia)*
5. "A toolbox for improving creative thinking" URV course (2021) *(Tarragona, Spain)*
6. Master's thesis supervision (Havvagul Ermis) "Mechanical properties of aligned PCL nanofibers" (2018- 2019) *(Tarragona, Spain)*
7. Master's thesis supervision (Paula Martínez Cánovas) "Porosity determination of electrospun fibers by microscopy techniques" (2019-2020) *(Tarragona, Spain)*
8. Master's thesis supervision (Tamer Ben Hassan) "Porosity determination of polystyrene (PS) nanofibers by microscopy techniques" (2021-2022) *(Tarragona, Spain)*
9. Tissue Engineering and Regenerative Medicine (TERMIS) Membership
10. Aerogels Cost Action Membership
11. Attendance in TERMIS 2021 (*Maastricht, The Netherlands*)
12. Oral Presentation in the European Workshop on Electrohydrodynamic Atomization and Electrospinning *(Naples, Italy, 2021)*
13. Poster presentation in TERMIS congress *(Rhodes, Greece, 2019)*
14. Poster presentation in NanoBioMed *(Barcelona, Spain, 2019)*
15. Attendance in International Symposium on Encapsulation Technology 2018 *(Tarragona, Spain)*
16. Certificate of European Researcher's Night for doing a workshop in nanochemistry for kids *(Tarragona, Spain, 2019)*
17. Poster presentation on Doctoral Day at Universitat Rovira i Virgili (2019)
18. Certificate of organizer and poster presentation in the European Electrohydrodynamic Atomization Workshop at URV *(Tarragona, Spain, 2019)*
19. "The literature review process in Science & Technology" course (2019) *(Tarragona, Spain)*
20. "Using posters to communicate research" course (2019) *(Tarragona, Spain)*
21. "Presentation skills" course (2021) *(Tarragona, Spain)*

Abbreviations

AFM: atomic force microscopy
ASTM: American society for testing and materials
DMA: dynamic mechanical analyzer
DMF: dimethylformamide
ECM: extra cellular matrix
FESEM: field emission scanning electron microscope
FPV: fractional pore volume
HV: high voltage
ID: inner diameter
IFP: individual fiber porosity
NSIPS: non-solvent induced phase separation
NFES: near field electrospinning
OD: outer diameter
PCL: polycaprolactone
PGS: poly (glycerol sebacate)
PMMA: poly(methyl methacrylate)
PS: polystyrene
PPE: personal protective equipment
RH: relative humidity
ROI: region of interest
SEM: scanning electron microcopy
SERS: surface enhanced Raman spectroscopy
TGA: thermogravimetric analysis
TEM: transmission electron microscopy
TE: tropoelastin
TIPS: thermally induced phase separation
XRD: x-ray diffraction

Contents

List of Publications

1) Akdemir, R., Ermis H., De la Flor, S., Rosell-Llompart J. (2023). *Macromolecules*, Facile uniaxial tensile testing of poly-ε-caprolactone (PCL) nanofibers- ***submitted to ACS Macromolecules.***

2) Wang, Z., Mithieux, S. M., Vindin, H., Wang, Y., Zhang, M., Liu, L., Zbinden, J., Blum, K. M., Yi, T., Matsuzaki, Y., Oveissi, F., Akdemir, R., Lockley, K. M., Zhang, L., Ma, K., Guan, J., Waterhouse, A., Pham, N. T. H., Hawkett, B. S., Weiss, A. S. (2022). Rapid Regeneration of a Neoartery with Elastic Lamellae. *Advanced Materials*, *34*(47), 2205614. doi.org/10.1002/adma.202205614

Summary

Chapter 1 Electrospinning is a versatile and innovative technique used to produce ultrafine fibers with diameters ranging from nanometers to micrometers. It involves the application of an electric field to a polymer solution or melt, resulting in the formation of continuous fibers that are collected on a grounded target. These fibers possess a high surface area-to-volume ratio and can exhibit unique properties, making them highly attractive for various applications. I will discuss the fundamentals, types, applications, advantages, and challenges of electrospinning in this chapter.

Chapter 2 This chapter describes all the electrospinning setups and special configurations used in this thesis. We have worked with different materials and fibers alignments. Each case required a specific configuration. We had purpose-made setups for randomly oriented fibers, aligned fibers and single fiber collection.

Chapter 3 In this chapter, we propose a new method for individual fiber porosity (IFP) determination based on annealing the nanofiber in order to collapse the pores and compare our results to the ones in the electrospinning literature. IFP experiments were done for poly(ε-caprolactone) (PCL) and polystyrene fibers (PS). In this new technique, we focused on microscopy techniques (SEM and AFM) for individual fiber porosity determination. SEM images were used to determine the cross-sectional area of the nanofiber before annealing. AFM and volume computation tools were used to determine the cross-sectional area of annealed fibers. We computed the porosity relying on the formula Porosity=Void fraction of the fiber/Total volume of the fiber.

Chapter 4 In this chapter, we propose a new method for tensile modulus determination, which is connected to Chapter 3 since individual fiber porosity influences the mechanical properties of fibers. The results of Chapter 3 were used in tensile modulus determination in this chapter. In summary, we ran two

independent experiments with the same parameters to produce aligned PCL fibers. Each experiment consisted of 10 tensile testing runs. We computed the "true" cross-section of the PCL fibers in order to exclude the area of the voids between fibers, which allowed us to estimate the tensile modulus of an individual fiber. Eventually, we compared our results with the individual fiber works in electrospinning literature, as well as the bulk PCL tensile testing data in literature.

Chapter 5-In this thesis, I will mostly target the tissue engineering applications as a final application. Tissue engineering, a multidisciplinary field that aims to regenerate or repair damaged tissues and organs, has greatly benefited from electrospun fibers. Their unique characteristics, including high porosity, high surface area, and the ability to mimic the extracellular matrix (ECM), make them well-suited for tissue engineering applications. We mainly focused on vascular scaffold tissue engineering for small diameter blood-vessels. We produced poly (glycerol sebacate) (PGS) /tropoelastin (TE) fibrous scaffolds at different ratios. The multiphoton microscopy images of produced scaffolds were 3D-rendered in order to observe the distribution of PGS and TE throughout the scaffold.

Chapter 1. Introduction

"The important thing is not to stop questioning. Curiosity has its own reason for existence. One cannot help but be in awe when he contemplates the mysteries of eternity, of life, of the marvelous structure of reality. It is enough if one tries merely to comprehend a little of this mystery each day."

— Albert Einstein

Old Man's Advice to Youth: Never Lose a Holy Curiosity. *LIFE Magazine* (2 May 1955) p. 64

1.1. Introduction to electrospinning and (nano)fibers

Fibers, in the form of either continuous or non-continuous filaments, are both found abundantly in nature and can be produced from synthetic or natural polymers, as well [1, 2, 3]. Natural fibers are materials that are derived from plants, animals, and minerals. Some examples for natural fibers are silk, wool, linen, cotton, bamboo, coir, ramie, and sisal. These fibers have been used for thousands of years to create products for human use. Cotton is perhaps one of the most well-known natural fibers. It is derived from the cotton plant's seed fibers and is widely used in the textile industry. Flax fibers come from the stem of the flax plant, and they are used to produce linen, a durable and breathable fabric. Wool is a natural fiber derived from the fleece of sheep and other animals like goats (cashmere, mohair), rabbits (angora), and alpacas. Silk is another example of natural fibers produced by animals, in this case, silkworm cocoons.

Figure 1.1 shows examples of natural fibers as plants, in bundles, and their SEM surfaces. SEM images of some other natural fibers are shown in Figure 1.2.

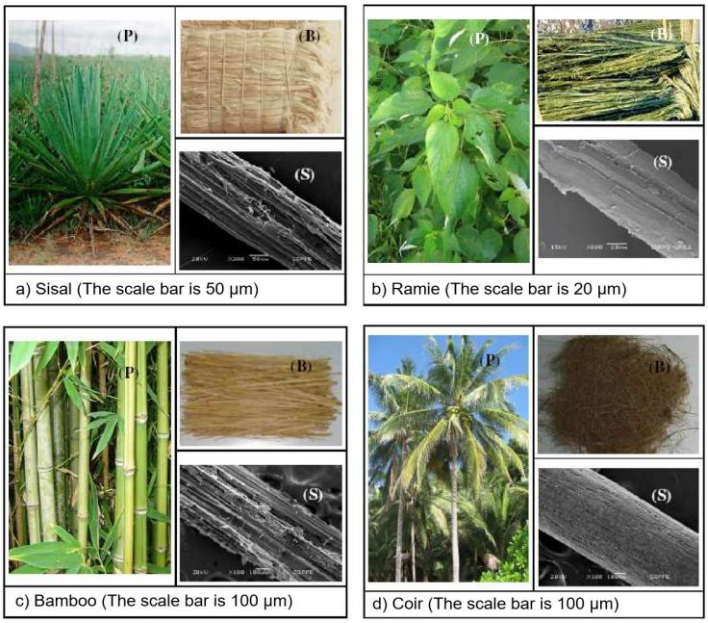

Figure 1.1. Examples of natural fibers. Illustration of a plant (P); a bundle (B) and SEM surface (S) Adapted from Ref. [3].

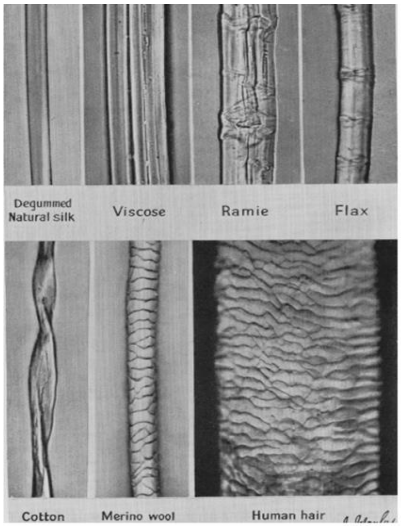

Figure 1.2. A selection of photomicrographs of textile fibers at x400 magnification. Adapted from Ref. [4].

It is possible to see examples of fibers all around us in our daily lives. One familiar example is the masks we used during the recent COVID19 pandemic (Figure 1.3a). The masks are made of fibers that filter out large particles in the air when the

wearer breathes in. A zoom-in image is shown in Figure 1.3b. Moreover, fibers play a crucial role in the design and functionality of protective clothing. Fibers with high tensile strength and abrasion resistance (such as Kevlar®) are used in protective clothing to shield against mechanical hazards such as cuts, abrasions, and punctures. These "super tough" Kevlar® fibers often used in bulletproof vests or other high wear resistance required applications in aerospace, automotive, and sports [5,6,7]. These fibers help prevent physical damage to the wearer. Figure 1.3c shows protective gloves made of Kevlar® fibers.

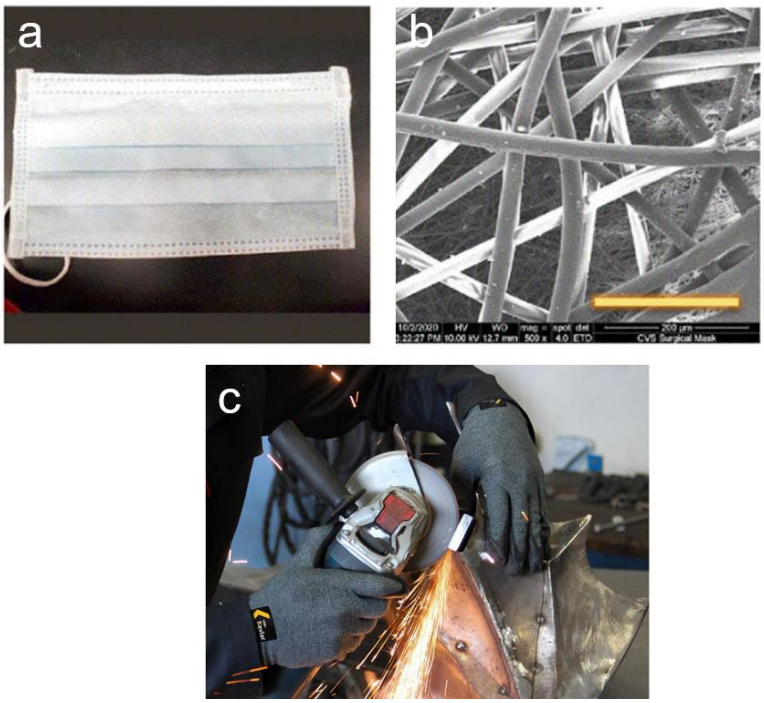

Figure 1.3. a) Surgical mask, b) Zoom-in image of the surgical mask, the scale bar is 200 µm. Adapted from Ref. [8] c) DuPont™ protective gloves made of Kevlar® fibers (Image property of DuPont).

The history of fibers goes back to ancient times. Silkworm cultivation began in 2700 BC and fragments of cotton articles dating back to 5000 BC. These natural components were used in the production of fabrics and clothes. Eventually, these natural examples of fibers served as a source of inspiration for man-made fibers.

Different techniques were introduced for making fibers from natural and synthetic materials. Throughout history, the first attempts relied on either the extrusion of a liquid or electrostatic attraction to form a filament. In 1600, the first record of the electrostatic attraction of a liquid was observed by William Gilbert. Christian Friedrich Schönbein produced highly nitrated cellulose in 1846, which was in fiber form. In 1887 Charles Vernon Boys described the process in a paper on nanofiber manufacture. John Francis Cooley filed the first electrospinning patent in 1900 [9]. The first spindle (based on extrusion) was invented in the 1880s in order to make fabrics from cotton and wool, and it became commercialized in 1911. Since then, spindle technology gathered much attention in polymer science. The first synthetic fiber from nylon was produced by the company DuPont™ in 1938 and immediately caught the public's attention [10]. This technology relied on extruding the fiber, winding it on bobbins, putting a finish on it, and knitting it into stockings on machines made to knit silk (Figure 1.4).

Figure 1.4. A photo of the first nylon fiber and the DuPont™ nylon stocking commercial in 1938.

One of the most used techniques nowadays is the electrohydrodynamic phenomenon for producing fibers called *electrospinning* (Figure 1.5a), where nanofibers are produced by the elongation of a liquid driven by electrostatic forces (Figure 1.5b). Electrospun nanofibers typically range from a few nanometers to several hundred nanometers (Figure 1.5c). In electrospinning, elongation of a liquid drop relies on the electric field, electrostatic forces overcome the surface tension and form the fibers. Solution electrospinning can be divided into many

subsections such as conventional electrospinning, near-field electrospinning, co-axial electrospinning, needleless electrospinning, etc.

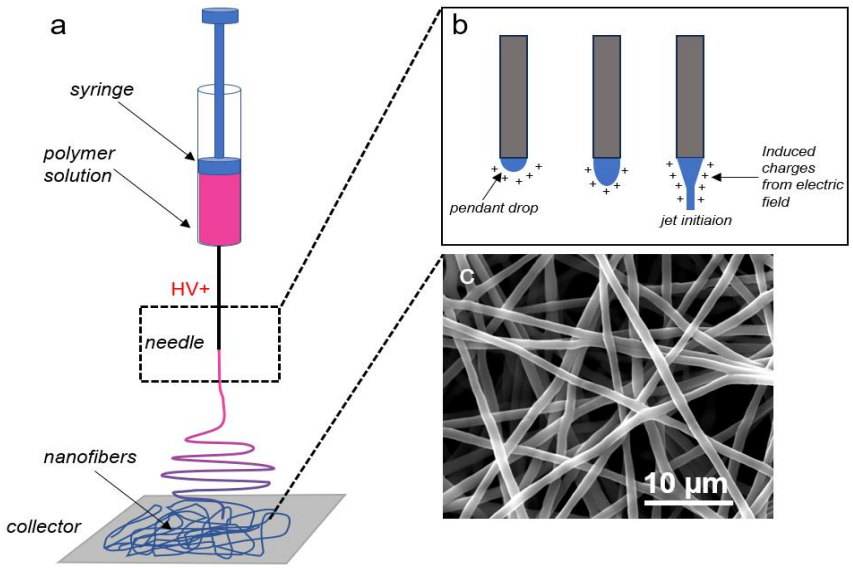

Figure 1.5. a) Electrospinning technique b) jet initiation by electric field c) randomly oriented electrospun nanofibers

Although known for decades in the 20th century, electrospinning launched polymer nanofibers into the broader realms of nanotechnology and materials science since 1990. In 1993, the term "electrospinning" was officially documented in the Web of Science, attributed to a conference paper authored by Darrell H. Reneker. This paper emphasized the exceptional attributes of electrospinning as a manufacturing method, along with the distinctive structure of nanofibers produced through this process [11]. The chronological evolution of electrospinning is shown in Figure 1.6. Among all the other fiber and filament production techniques, electrospinning has rapidly become a low-cost, broadly applicable, versatile method that manufactures fibers on a laboratory bench, to serve diverse needs ranging from materials science and technology to life sciences and clinical medicine. The high ratio of surface area to mass and porous structure are the primary characteristics of nanofibers and are very advantageous in many applications [12].

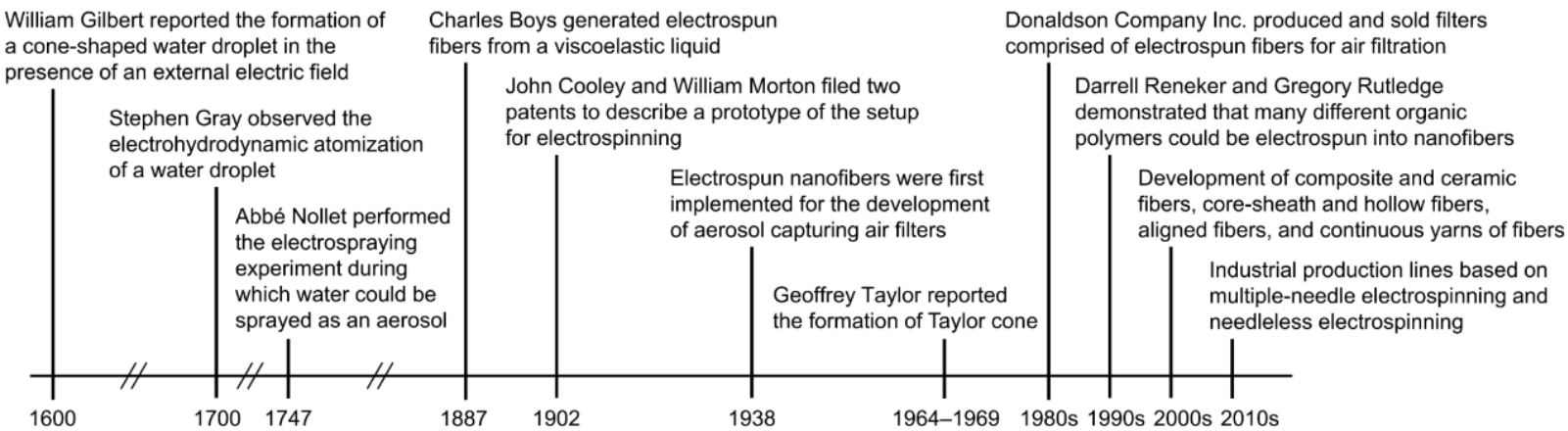

Figure 1.6. Chronological evolution of electrospinning. Adapted with permission from Ref. [10].

1.2. Other techniques for producing nanofibers

Even though we used solution electrospinning in our experiments, it is useful to review other competitive methods to improve the ways in which it is unique. To begin, it is important to note that no single spinning technique is universally the best for all applications. Each technique has its own advantages and limitations, and the choice of technique depends on factors such as the desired properties of the fibers, the material being used, the required production scale, and the specific application's requirements. Other spinning techniques, such as wet spinning (Figure 1.7a), melt spinning (Figure 1.7b), solution blow spinning (Figure 1.8a), electro-blowing (Figure 1.8b), and solution spinning, also have their own merits depending on the context in which they are applied.

Melt spinning is a process where the melted polymer is discharged from the spinneret. The discharged fiber undergoes a quenching and drawing process in order to give the desired fiber form. Similarly, melt blowing is a fabrication method of micro- and nanofibers where a polymer melt is extruded through small nozzles surrounded by high-speed blowing gas [13, 14]. Solution blow spinning follows a similar procedure; however, a polymer solution is used instead of a polymer melt (Figure 1.8) [15]. In these methods, there is *no use of electric fields*.

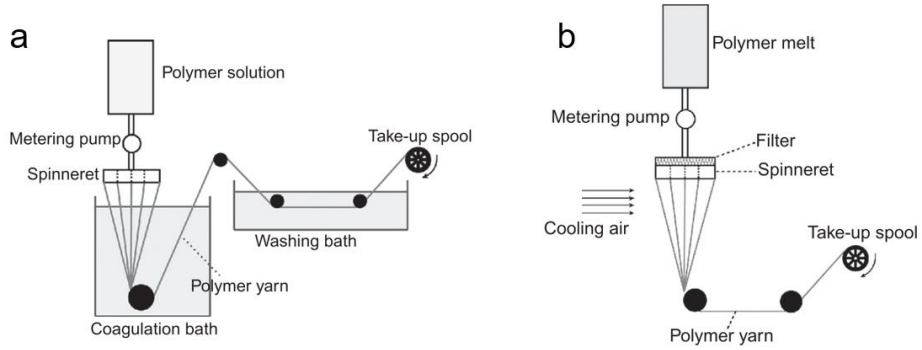

Figure 1.7. Illustration of wet spinning (a) and melt spinning (b) Adapted from Ref. [16]

Solution blow spinning is like melt blowing in that both processes use a gas jet to aid in the extension of the spinning jet. However, melt blowing uses only the drawing force from the gas jet to stretch the fiber while electro-blowing (Figure

1.8b) relies more on electrostatic repulsion to stretch the fiber with the gas jet facilitating solution drawing at the initial phase [17].

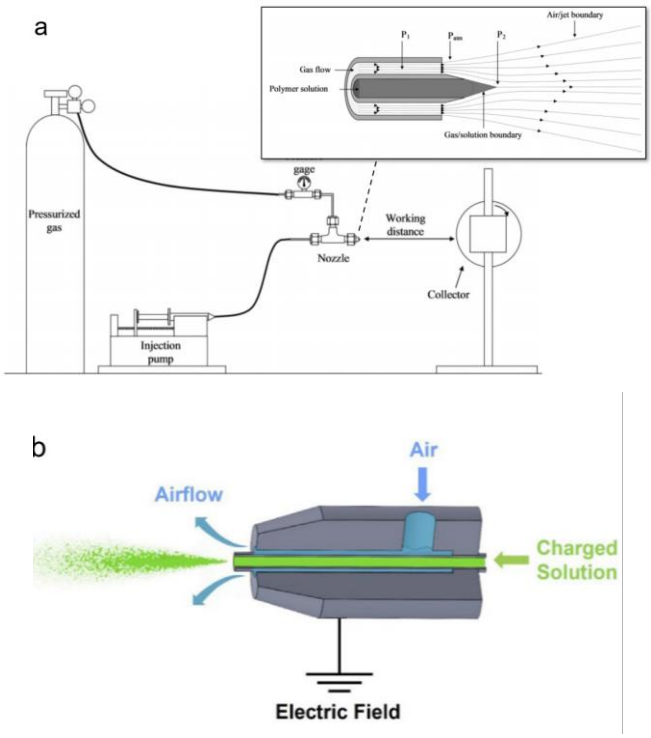

Figure 1.8. a) Solution blow spinning setup. The inset shows a zoom-in image of the spinneret. Adapted with permission from Ref. [15]. b) Electro-blowing hybrid forces. Adapted from Ref. [18].

In terms of fiber characteristics, melt-blown fibers have a highly porous and random structure due to the turbulent air streams used during processing. Melt-spun fibers typically have a smooth and uniform surface. They exhibit a solid, continuous structure. Solution-blown and electro-blown fibers can exhibit a range of morphologies, from smooth and uniform to irregular and textured, depending on polymer-solvent interactions and processing conditions.

1.2.1. What makes electrospun nanofibers so special?

- Large surface area: Nanofibers made by electrospinning possess an extremely high surface area-to-volume ratio. This increased surface area allows for enhanced interactions with surrounding environments, making nanofibers suitable for applications such as filtration, sensing, and drug delivery. The large surface area enables efficient adsorption, catalytic reactions, and molecular interactions [19, 20, 21].
- High porosity: Nanofibers typically have a porous structure, which allows for the transport of fluids, gasses, and nutrients. The porous nature of nanofibers is particularly advantageous in filtration applications, as it enables efficient separation and removal of particles, bacteria, or contaminants from liquids or gasses. *(Chapter 3 provides a more extensive explanation regarding the porosity of nanofibers.)*
- Mechanical strength: Despite their small diameter, nanofibers can exhibit remarkable mechanical strength. They can withstand tensile forces and maintain structural integrity, making them suitable for use in applications where strength and durability are crucial, such as in tissue engineering scaffolds or reinforcement materials for composites. *(Chapter 4 provides a more extensive explanation of the mechanical properties of nanofibers.)* There are several studies claiming there is a "nano-size effect" in nanofibers, meaning, the tensile modulus increases with the fiber diameter decreases [22, 23]. It is discussed in the literature that below 100 nm this effect becomes more drastic.
- Tailorable properties: Nanofibers can be manufactured by electrospinning from a wide range of materials, including polymers, ceramics, metals, and composites. This material versatility allows for the tailoring of nanofiber properties to meet specific requirements. By selecting different materials and adjusting the fabrication parameters, characteristics such as mechanical strength, porosity, surface chemistry, and biocompatibility can be customized.

- Versatility: Nanofibers can be loaded with bioactive molecules, such as drugs or growth factors, and used as drug delivery systems. The high surface area and porous structure of nanofibers enable the controlled release of these substances, providing sustained and localized therapeutic effects. This controlled drug delivery approach can improve treatment efficacy and minimize side effects [24]. Nanofibers find applications also in energy storage, environmental remediation, and sensing. For example, they can be used in supercapacitors and batteries to improve energy storage capacity and efficiency. They can also be functionalized to selectively capture pollutants or facilitate catalytic reactions for environmental remediation [25, 26, 27]. Functionalized nanofibers are used in many fields such as drug delivery, water filtration, biomedical applications, energy storage and protective clothing, and give very promising results (Figure 1.9).

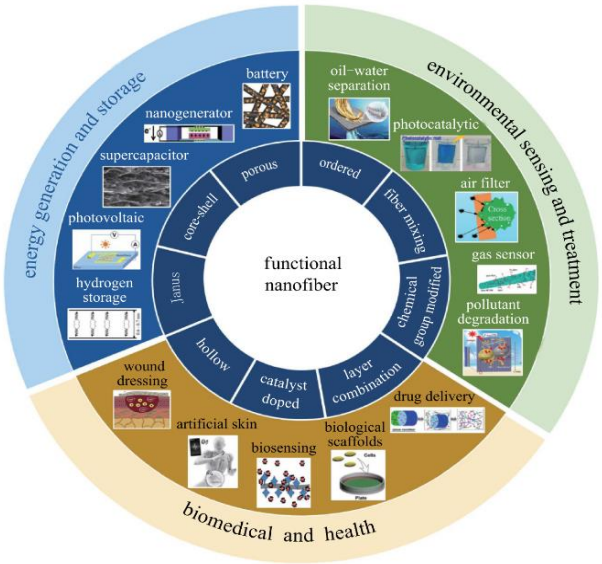

Figure 1.9. Functional nanofibers and their applications. Adapted from Ref. [28].

Nanofibers have gained significant attention in biomedical fields, particularly in tissue engineering and regenerative medicine. The nanoscale architecture of the fibers closely mimics the extracellular matrix (ECM) of natural tissues, facilitating

cell adhesion, proliferation, and differentiation. Nanofiber scaffolds provide a supportive environment for cell growth and tissue regeneration [29]. *(Chapter 5 provides a more comprehensive explanation of the biomedical applications of nanofibers.)* Many examples of fibers (and nanofibers) can be frequently encountered in the human body. Therefore, tissue engineering and regenerative medicine take great advantage of electrospinning techniques. Fabrication of biomedical scaffolds by electrospinning has been becoming popular in the last century in order to improve tissue regeneration. In tissue engineering, it is important to mimic the morphology of the natural tissue to create the proper environment for the cells to regenerate. These artificial fibrous structures are called "scaffolds" and they help promote cell growth. For example, one of the most important components of bones is collagen fibers as shown in Figure 1.10. In this example, we can see the fibrous nature of collagen and tropocollagen.

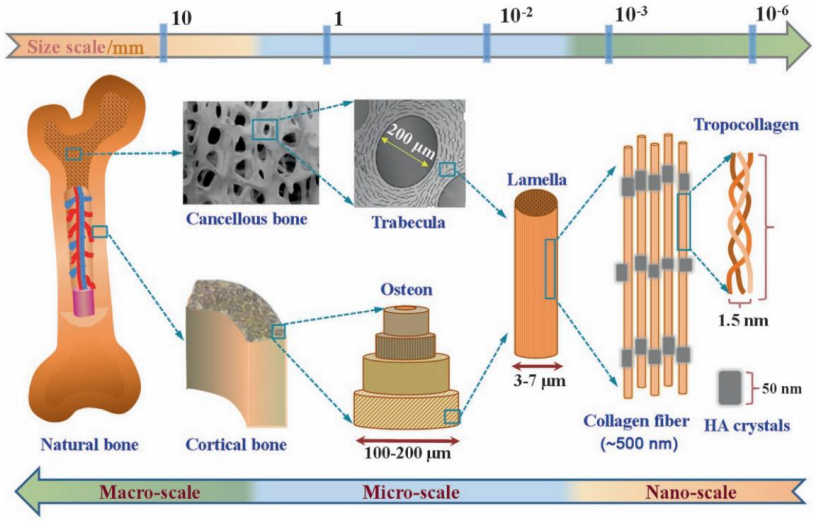

Figure 1.10. Illustration of collagen fibers in bone. Adapted from Ref. [30].

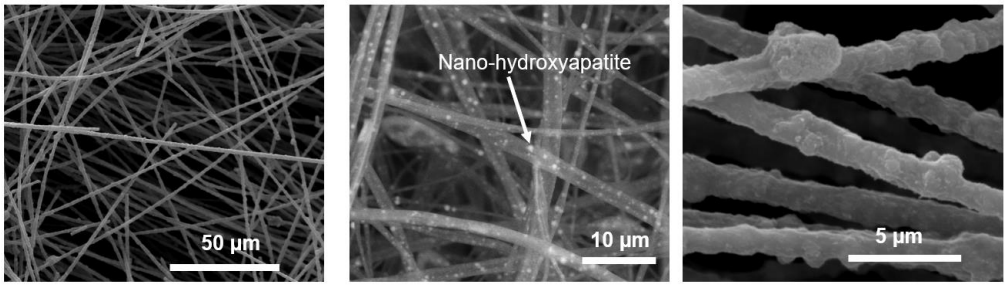

Figure 1.11. PMMA fibers incorporated with hydroxyapatite nanoparticles for bone tissue engineering applications (prepared by us).

As an example, Figure 1.11 shows nanofibers suitable for bone repair. This scaffold consists of polymeric nanofibers (PMMA) and nano-hydroxyapatite (nHA) which is a derivative of calcium phosphate that is naturally found in your teeth and bones. It is claimed that the incorporation of nHA can promote cell growth throughout the nanofibrous scaffold [31, 32, 33].

1.3. Fundamentals of solution electrospinning technique

1.3.1. Principles of Electrospinning, Taylor Cone, Jet Evolution

Electrospinning involves an electrohydrodynamic process, during which a liquid droplet is electrified to generate a jet, followed by stretching and elongation to generate nanofibers.

During the electrospinning process, the electric field overcomes the surface tension in the liquid extruded from the spinneret. As the applied voltage increases, the electrical force overcomes the surface tension force, causing the droplet to deform into a conical shape (Figure 1.12a). This conical shape is known as the Taylor cone, from which a charged jet is ejected. When a high voltage is applied to a droplet of polymer solution or melt at the tip of the needle, several forces come into play. These forces mainly include the electrical force, surface tension, and viscous drag. The electric field causes charge accumulation at the droplet's surface, leading to the formation of a charged layer and to the repulsion of like charges. This charged layer generates a strong electric field that counteracts the

surface tension of the droplet. The forces playing a role in jet initiation are illustrated in Figure 1.12b.

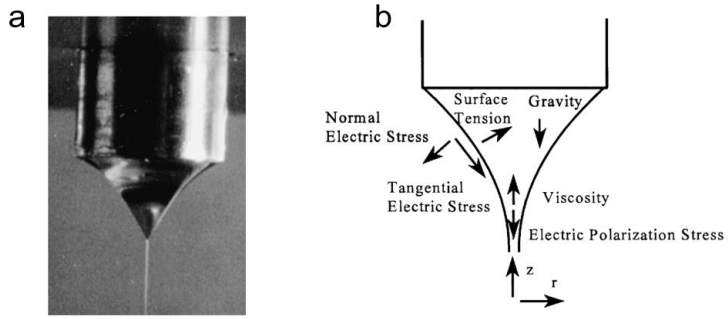

Figure 1.12. a) The experimental cone shape b) Formation of a Taylor cone and jet initiation and forces acting on a liquid jet in the presence of an electric field. Adapted with permission from Ref. [34].

Depending on the solution properties and experimental parameters, the jet can undergo (Figure 1.13a): (i) a breakup (in which case, we call it electrospray) by the Rayleigh instability, (ii) beading mode (Figure 1.13b), which results in beaded fibers or (iii) create a continuous jet without a breakup which results in electrospinning.

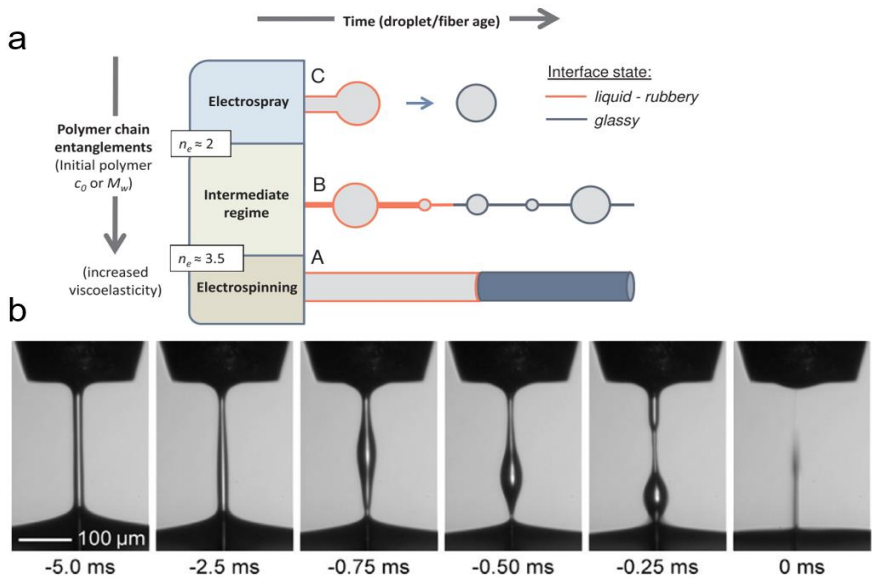

Figure 1.13. a) Different scenarios of polymeric jet breakup resulting in different microstructures as the solvent evaporates**.** Adapted with permission from Ref. [35]. B) Breakup process in the beading mode that causes beaded fibers. Adapted with permission from Ref. [36].

Different fiber morphologies obtained by different electrospinning jet-modes are shown in Figure 1.14.

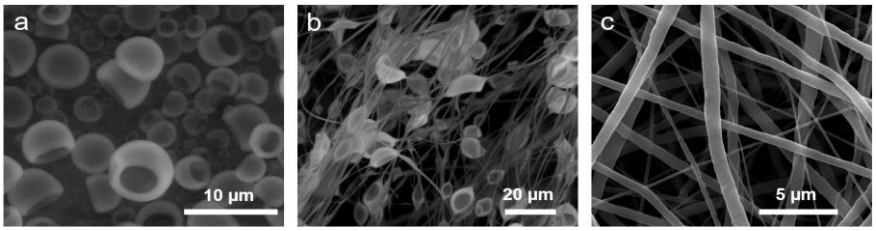

Figure 1.14. PMMA a) nanoparticles b) beaded nanofibers c) nanofibers (produced by us)

Typically, in electrospinning, the jet initially extends in a straight line and then undergoes vigorous whipping motion as the result of so-called bending instabilities (Figure 1.15). As the jet stretches into finer diameters, it leads to the deposition of fibers on the collector [12, 37].

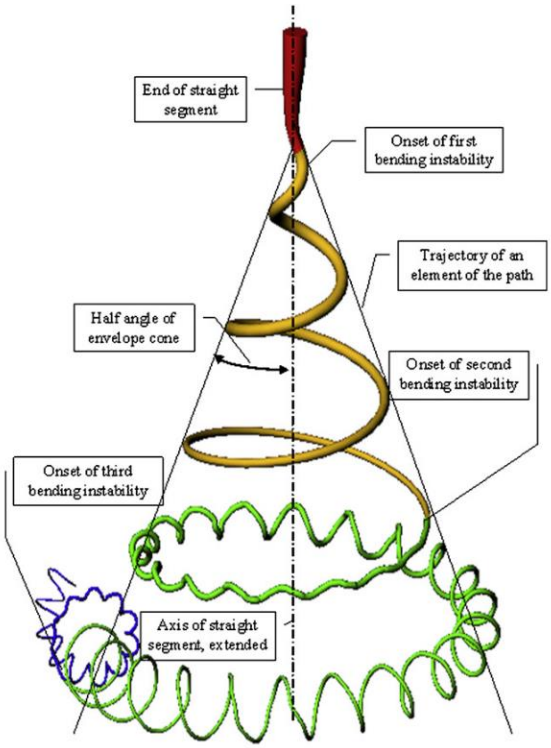

Figure 1.15. A diagram that shows electrical bending instabilities. Adapted with permission from Ref. [12].

The formation of the Taylor cone is a critical step in the electrospinning process as it signifies the transition from a (large) liquid drop to a continuous jet of polymer solution or melt. The stretching of the jet leads to the thinning of the jet. The increase in surface area caused by the stretching also accelerates its solidification by promoting solvent evaporation (mass transfer) in solution electrospinning or cooling (heat transfer) in melt electrospinning, resulting in the formation of fine fibers.

Understanding the Taylor cone is important for controlling the electrospinning process and optimizing the production of high-quality fibers. It is named after Geoffrey Ingram Taylor, a British physicist who first mathematically described this phenomenon in 1964 [38]. He characterized the Taylor cone by an angle of 49.3. The angle of the Taylor cone has been independently confirmed by Larrondo and Manley [39], who observed experimentally that the semi-vertical cone angle just before jet formation is 50°. However, in another publication, an angle of 33.5° was reported for the Taylor cone instead of the previously mentioned 49.3° [40].

The electric field induces a charge on the droplet's surface, counteracting the effects of surface tension and causing the droplet to change from a spherical to a conical shape. Once the intensity of the electric field (V) reaches a critical value (V_c), the electrostatic forces surpass the surface tension of the polymer solution, resulting in the ejection of a liquid jet from the tip of the Taylor cone. The point of highest charge density is located at the cone's tip, serving as the initiation point for the jet. Taylor determined that V_c (in kilovolts) can be calculated using the formula:

$$V_c = 4\left(\frac{H^2}{L^2}\right)\left(ln\frac{2L}{R} - 1.5\right)(0.117\pi R\gamma)$$

where H represents the air-gap distance, L is the length of the capillary tube, R denotes the radius of the tube and γ represents the fluid's surface tension (N/m) [41].

Understanding the interplay between these factors allows for the control and manipulation of the Taylor cone, enabling the production of desired fiber characteristics. Various factors, such as solution concentration, field strength, flow rate, jet velocity, and shear rate, have a significant impact on the electrospinning process. In the case of low molecular weight fluids, the decay rate of an electrostatically driven jet's radius depends on the flow rate of the polymer solution. When the flow rate is slow, the jet radius rapidly decreases [42].

The following QR shows an example video of the Taylor Cone formation in our experiment.

1.3.2. Roles of viscosity, concentration, molecular weight, and fiber formation

Viscosity, concentration, molecular weight, polymer chain entanglements, and fiber formation are all important factors that affect the electrospinning process and the resulting nanofibers produced.

Viscosity is a measure of a liquid's resistance to flow, and it is a critical parameter in electrospinning. A higher viscosity can make it more difficult for the electrospinning solution to form a stable jet, resulting in thicker fibers with lower surface area. On the other hand, lower viscosity solutions tend to form thinner fibers with higher surface area. However, too low viscosity results in jet breakup, thus electrospray. Therefore, selecting the appropriate viscosity and polymer chain entanglements for the electrospinning solution is crucial for achieving the desired fiber morphology and properties. (As shown in Figure 1.13a)

For homogenous polymeric solutions, the well-known Huggins Equation describes the solution viscosity as a function of polymer concentration:

$$\eta_{sp}\,[c] = [\eta]c + k_H\,[\eta]c^2 + \ldots$$

where η_{sp} (c) is the specific viscosity that is a measure of the resistance to flow exhibited by a fluid or material when subjected to shear stress. In simpler terms, specific viscosity quantifies how easily a material flows when a force is applied to it. [η] is the intrinsic viscosity (a measure of a solute's contribution to the viscosity of a solution), c is the polymer concentration, and k_H is the Huggins coefficient. [η]c is referred to as the Berry number, B_e[43]. The significance of the Berry number arises from the fact that for a solution to have chain entanglements, $B_e > 1$. In dilute solutions, where polymer chains do not overlap each other (Figure 1.16), B_e can, at best, be unity ($B_e \sim 1$). The critical chain overlap concentration, c*, is the crossover concentration between the dilute and the semi-dilute concentration regimes. Without the chain crossover, it is not possible to form fibers but particles, as shown in Figure 16. The critical chain overlap, c*, can be expressed as:

$$c^* \sim \frac{N}{\langle R^2 \rangle^{3/2}} \sim \frac{1}{[\eta]}$$

where N is the number of monomers and $\langle R \rangle$ is end-to-end distance. it is clear that $c^*[\eta] \sim 1$ in the dilute solution limit, thereby suggesting the criteria, $c^* \sim 1/[\eta]$, as a means of evaluating c* (this criterion is the same as that discussed above with regard to $B_e \sim 1 = c \sim 1/[\eta]$ in the dilute solution limit). Hence, *M* being molecular weight and N_{av} is the Avogadro number the calculation of c* from chain dimensions:

$$c^* = \frac{3M}{4\pi \langle R^2 \rangle^{3/2} N_{av}}$$

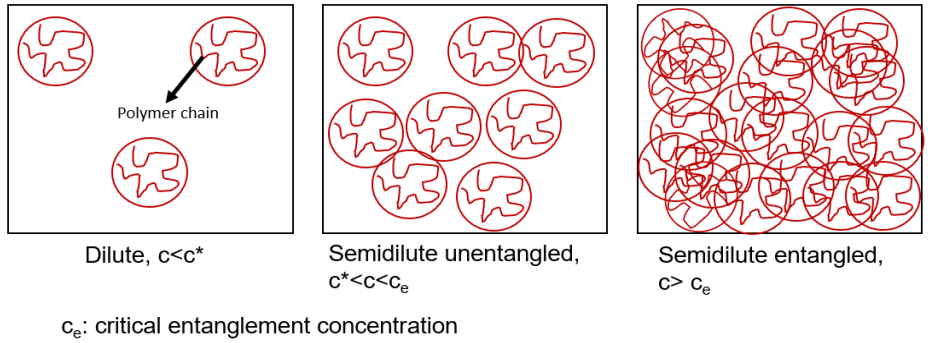

Figure 1.16. Physical representation of the three solution regimes, (a) dilute, (b) semi-dilute unentangled, and (c) semi-dilute entangled. Inspired by Ref. [44].

Molecular weight is also a significant factor in electrospinning, as it affects the chain entanglement and intermolecular forces within the polymer solution. Generally, higher molecular weights lead to more entanglement and stronger intermolecular forces, resulting in thicker and more uniform fibers. Conversely, lower molecular weights can result in thinner fibers with increased porosity (Figure 1.17). Therefore, the choice of molecular weight must be carefully considered to achieve the desired fiber properties [44].

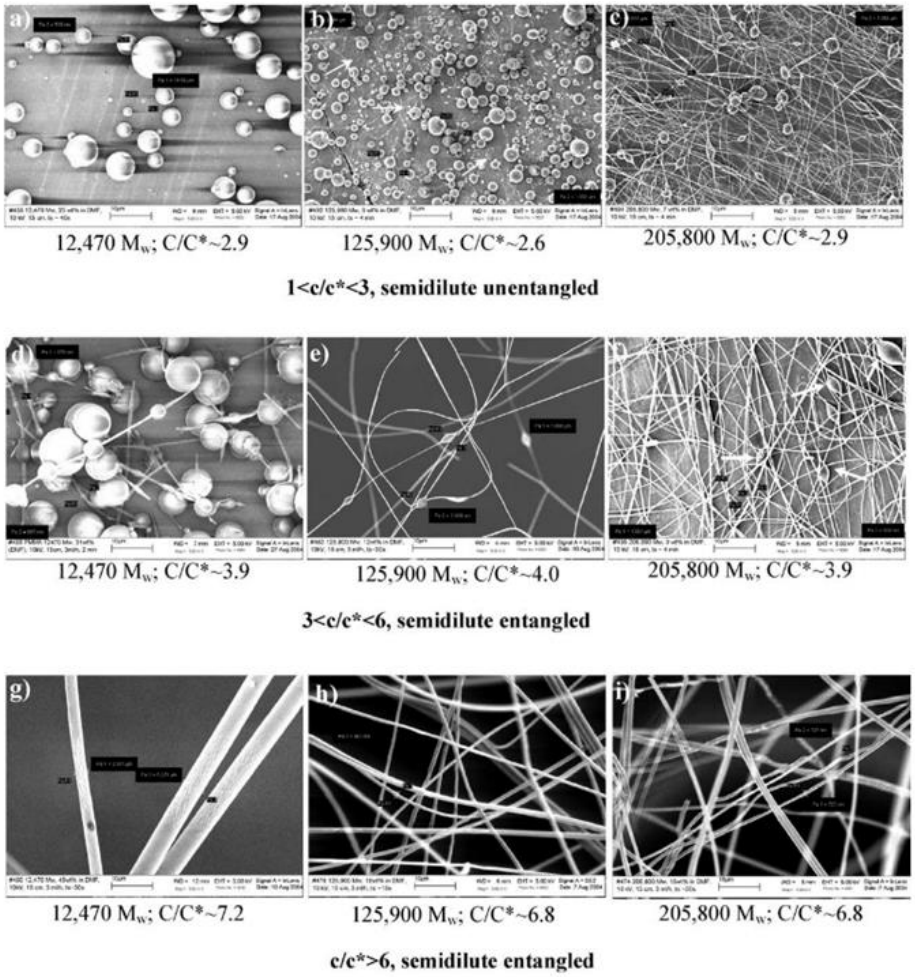

Figure 1.17. SEM micrographs of PMMA electrospun from solutions in the semi-dilute unentangled and entangled regimes for the three synthesized MW grades 12,470, 125,900, and 205,800. All micrographs have the same magnification and the scale bars in the micrographs correspond to 10 mm. Adapted with permission from Gupta et al [44].

Moreover, fiber formation is influenced by several parameters, including the electrospinning voltage, solution conductivity, and environmental conditions such as temperature and humidity. A higher voltage can generate a more stable jet, resulting in finer and more uniform fibers. However, too high a voltage can cause branching or beading of the fiber, leading to a less uniform fiber structure, or even electrical breakdown of the surrounding gas (typically air). Additionally, environmental conditions such as temperature and humidity can affect the

electrospinning process, typically by altering the surface tension and viscosity of the solution [44, 12]. For example, high humidity can potentially lead to slower solvent evaporation. This extended drying time could result in decreased fiber diameter and changes in fiber morphology [45]. On the other hand, rapid solvent evaporation causes phase separation into polymer-rich and solvent-rich domains. Water molecules can cause polymer precipitation on the surface and leave the fiber with internal pores as in the PS/DMF case [46, 47]. (Explained later in detail in Chapter 3) In another case, a water-soluble polymer or a polymer that can be made more flexible by water plasticization, the uptake of water by the jet causes a delay in the solidification process. This delay can occur either due to the slower evaporation of water or due to the plasticizing effect of water on the polymer. Consequently, fibers are coarser at low humidity [48].

In summary, electrospinning is a complex process that is influenced by several parameters, including viscosity, concentration, and molecular weight. By carefully controlling these factors, researchers can produce nanofibers with a wide range of properties.

1.4. Types of electrospinning

Most common and versatile electrospinning methods can be listed as needle-based electrospinning, multi-axial electrospinning, bi-component electrospinning, multi-needle electrospinning, and needleless electrospinning.

1.4.1. Conventional Needle-based Electrospinning

In conventional needle-based electrospinning, also known as "far-field electrospinning" or "traditional electrospinning", usually a solution (the solution can be a mixture of several components) goes to a single spinneret and ejects from it by the electric field. This electric field-assisted process ends up forming fibers on a collector. This technique is the most widely used and involves the use of a high voltage to create an electric field that pulls a jet of polymer solution from a syringe or spinneret. The jet undergoes bending and whipping motions as it moves toward the collector, causing the solvent to evaporate and the polymer chains to elongate and solidify into nanofibers. This technique is relatively simple and

versatile, but it can be difficult to control the fiber diameter and morphology [49, 26]. With this technique, the fibers can be deposited in a random or aligned manner depending on the collector type. It can be used in horizontal or vertical configurations (Figure 1.18).

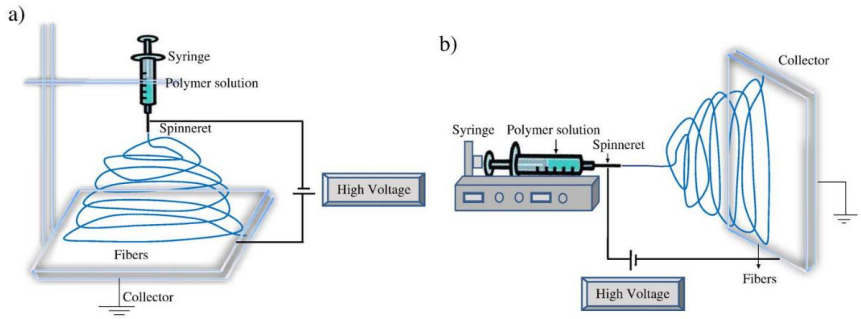

Figure 1.18. Conventional electrospinning a)vertical and b)horizontal design. Adapted with permission from [50].

1.4.2. Near-field Electrospinning

Near-field electrospinning (NFES) is a technique used for positioning electrospun nanofibers with high precision and control over a substrate (usually flat). It involves the use of a small gap between the spinneret and the collection substrate, typically in the range of a few (1-5) millimeters. This proximity allows for enhanced electric field focusing, resulting in the production of nanofibers with reduced diameters and improved alignment compared to conventional electrospinning methods (Figure 1.19) [51, 52]. Liashenko et al. recently showed that fibers can be precisely collected on the mechanical stage (even be printed by stacking nanofibers on top of each other) by using electrodes around the jet (Figure 1.20) [53].

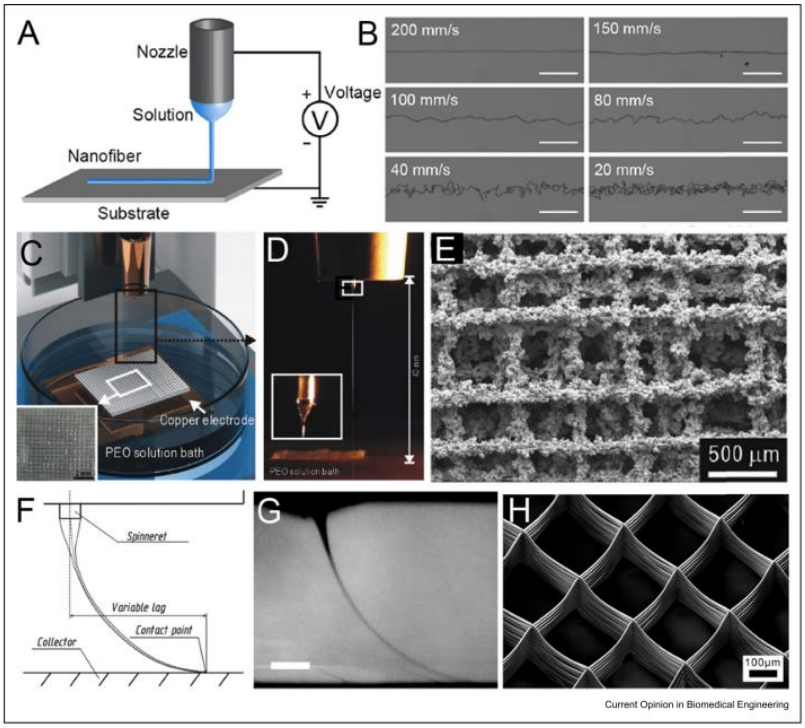

Figure 1.19. Melt electrowriting. Adapted with permission from Ref. [54].

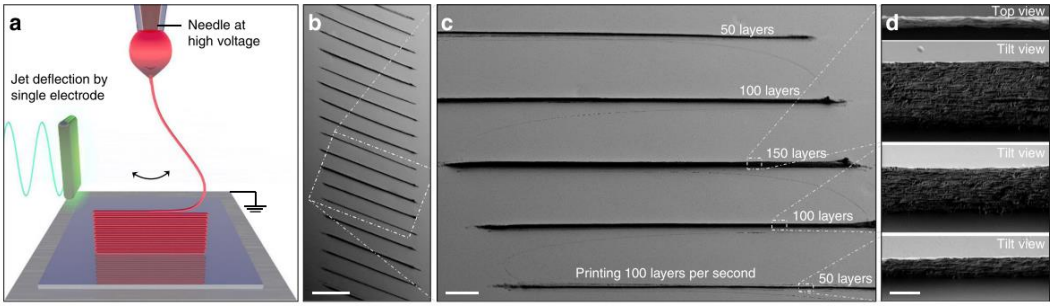

Figure 1.20. Stacking nanofibers on top of each other. Adapted from Ref [53].

1.4.3. Multi-axial Electrospinning

In this technique, two or more concentric needles are used to simultaneously extrude two or more solutions, which are then electrospun together to create a core-shell structure (Figure 1.21). The core and shell materials can be different polymers or even different functional components such as drugs, growth factors, or nanoparticles. This technique can be used to create fibers with different

properties in the core and shell, and it has applications in drug delivery and tissue engineering [55, 56].

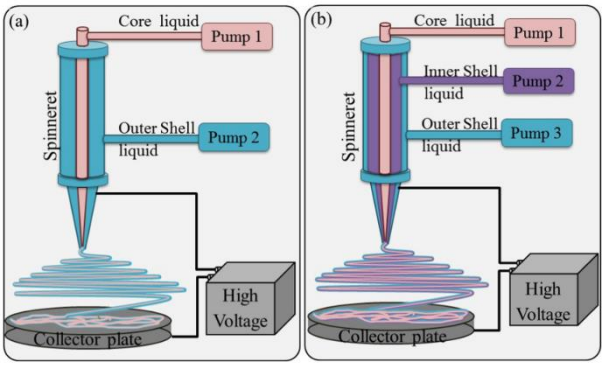

Figure 1.21. Multi-axial electrospinning. Adapted with permission from Ref. [56].

1.4.4. Multi-needle Electrospinning

Multi-needle electrospinning is usually preferred for mass production. An example of the multi-needle electrospinning setup is shown in Figure 1.22, where several needles are placed in a linear array, and fiber is deposited on a moving belt to produce a large nonwoven structure [57, 58].

Figure 1.22. Multi-needle electrospinning. Adapted from Ref. [57].

1.4.5. Needleless Electrospinning

Needleless electrospinning setup consists of a fiber generator (solution bath) where the nanofibers are elongated from, a collector, and a high-power supply.

Needleless electrospinning can indeed be adapted for the mass production of nanofibers, offering advantages such as higher throughput. Fiber generators can be designed in various shapes, as it is shown in Figure 1.23. It is claimed that needleless electrospinning has several advantages such as the conglobation of dopants in the electrospinning solution can easily block the needle spinneret and cease the electrospinning process. In the absence of a capillary spinneret, there will be no nozzle blockage in the needleless electrospinning. It is also claimed that needleless electrospinning can produce uniform and fine fibers. However, if one is working with volatile solvents, evaporation of the solvent in the solution bath can be a limitation.

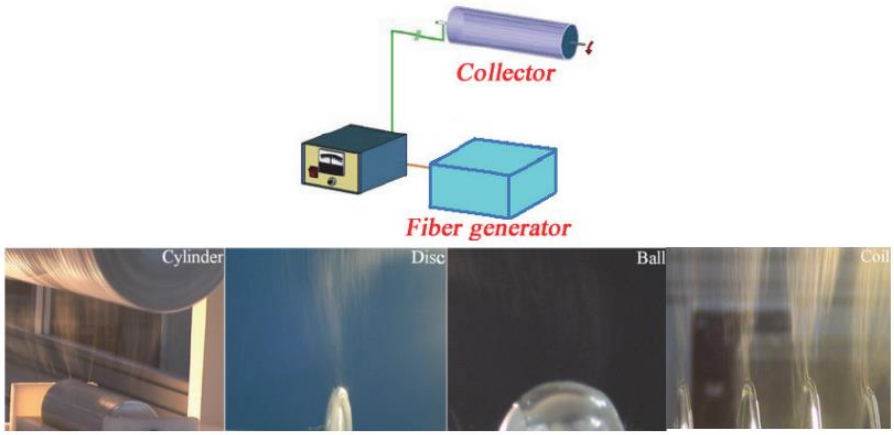

Figure 1.23. Multi-needle electrospinning. Adapted from Ref. [59].

1.5. Types of fiber morphologies and their applications

An electrospun mat is a fibrous material generated through the electrospinning process, where a polymer solution or melt is subjected to an electric field to create ultrafine fibers. These fibers are collected onto a substrate, forming a thin and often non-woven sheet-like structure.

1.5.1. Mat morphologies

The accumulation of fibers on the collector is called a mat. The arrangement of the fibers in the mat can have a strong impact on the mat's properties (e.g.,

mechanical). Two extreme situations can be identified: when fibers are aligned or when they are randomly oriented.

Aligned Nanofibers: Aligned nanofibers are characterized by their parallel arrangement along a specific direction as shown in Figure 1.24a. These fibers demonstrate a high degree of orientation and can be produced through techniques such as electrospinning with controlled collector motion, near-field electrospinning, or using electrodes with gap [47, 53, 60, 61].

Random Nanofiber Mats: Random nanofiber mats are formed when nanofibers are deposited in a disordered manner, resulting in a non-uniform distribution and orientation (Figure 1.24b). This morphology is commonly achieved through traditional electrospinning methods.

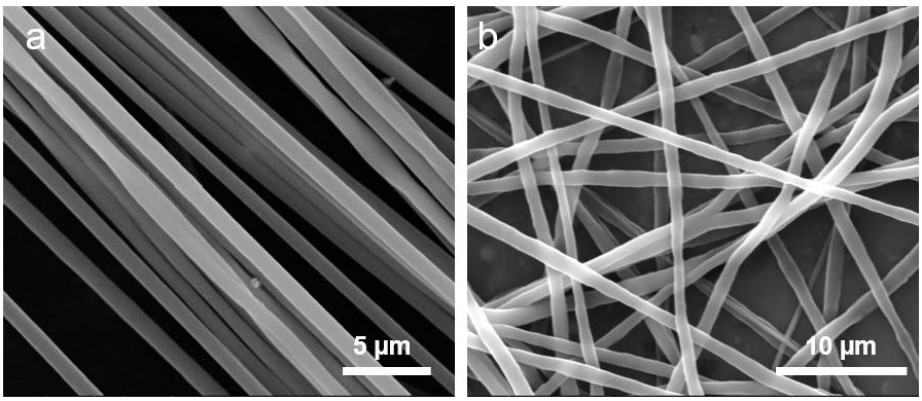

Figure 1.24. Examples of a) aligned fibers and b) random fibers (made of PMMA).

1.5.2. Individual fiber morphologies

Depending on the solution properties, humidity, or experimental conditions, different fiber morphologies can be obtained at individual fiber levels as shown in Figure 1.25. Nanofibers can be produced porous, hollow, beaded, compact, grooved, wrinkled, rough, or smooth. Each of them could be a target morphology for a specific application [62].

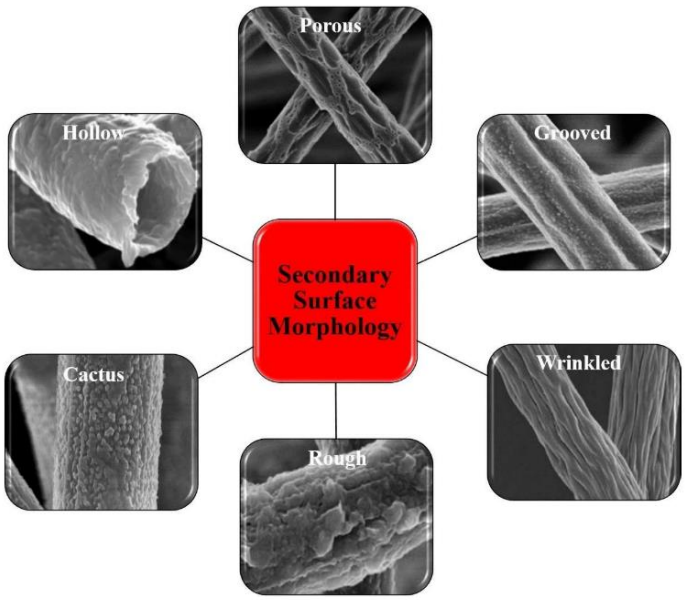

Figure 1.25. Individual fiber morphologies. Adapted with permission from Ref. [62].

Porous fibers

Increasing the porosity and specific surface area of fibers can be accomplished to improve the performance of absorption, catalysis, sensors, and so on. Therefore, porous fibers have presented extensive use in a wide variety of applications. The details of surface and interior porosity in fibers and their application areas are discussed in Chapter 3, in this thesis.

Grooved & wrinkled fibers

There are three grooved fiber formation mechanisms: void-based elongation, wrinkle-based elongation, and collapsed jet-based elongation, as shown in Figure 1.26.

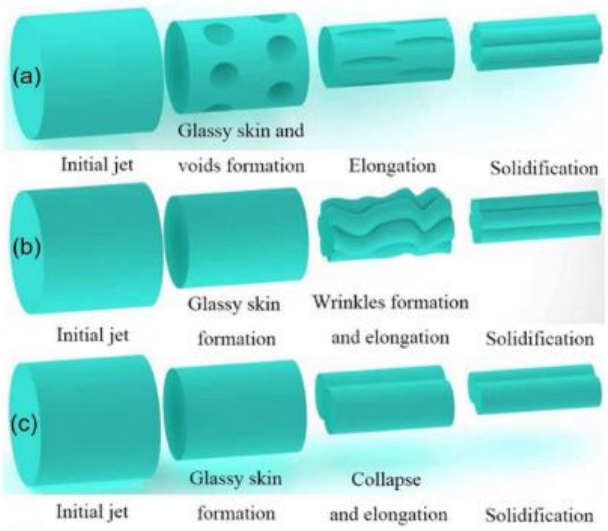

Figure 1.26. Formation of wrinkled and collapsed fibers. Adapted with permission from [62].

We observed this kind of morphology with fibers that are made of PMMA/Acetone (Figure 1.27).

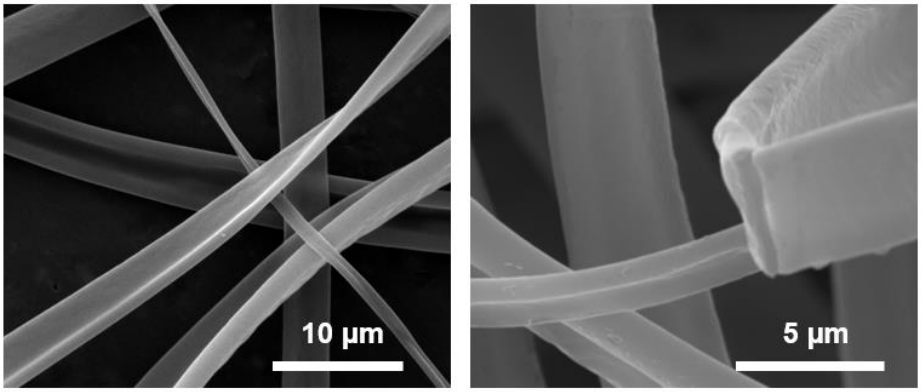

Figure 1.27. PMMA/Acetone ribbon-like fibers prepared by us.

Ribbon-like structures can be advantageous in tissue engineering since cells are more prone to attach and grow on rough surfaces rather than smooth surfaces. It is possible to see some examples of the specific usage of ribbon-like nanofibers in the literature [63, 64].

Hollow fibers

In general, multi-axial electrospinning is used for generating single or multiple-channel hollow fibers. Hollow fibers are great candidates for numerous applications, including gas separation, biomedical, microfluidic, bioreactors and sensors, drug delivery, thermal insulator coolers, energy storage, and much more. An example of hollow fibers is shown in Figure 1.28. Tian et al. did a very thorough review of hollow fibers and their applications. Further information can be found here in Ref. [65].

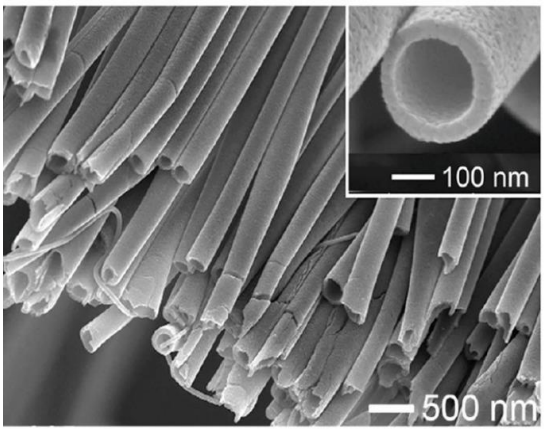

Figure 1.28. Hollow fibers. Adapted from Ref. [11]

1.6. Limitations and Challenges in Electrospinning

Despite significant advancements in the field of electrospinning, several challenges and limitations still exist. This section will highlight the current challenges faced in electrospinning, such as process scalability, fiber alignment control, and reproducibility. Additionally, it will discuss emerging trends and future perspectives in electrospinning research, including the development of advanced electrospinning setups, novel polymers and materials, and the integration of electrospinning with other fabrication techniques. The potential for electrospinning to revolutionize various industries and address societal challenges will be explored.

1.6.1. Scalability

Achieving scalability is important for industrial applications that require large quantities of nanofibers. Here are some key considerations for the scalability of electrospinning:

- Equipment design and modifications: Scalability requires careful design or modification of electrospinning equipment. The equipment should be capable of handling larger production volumes. This may involve increasing the size of the spinneret, collector, or electrospinning chamber. The design should allow for higher flow rates and efficient operation over extended periods.
- Process optimization: Scaling up the electrospinning process involves optimizing various parameters to ensure consistent and high-quality nanofibers. Factors such as solution viscosity, applied voltage, distance between the spinneret and collector, and environmental conditions (e.g., humidity and temperature) need to be controlled and adjusted appropriately. Optimization ensures that the desired fiber properties are maintained during scale-up.
- Material supply and handling: Scalability requires a reliable and continuous supply of materials for electrospinning. When scaling up, larger quantities of polymer solutions or melts may be required. Efficient storage, handling, and delivery systems should be in place to maintain the quality and properties of the materials throughout the process.
- Production rate and throughput: Increasing the production rate and throughput is a key aspect of scalability. Strategies to achieve higher production rates include using multiple spinnerets simultaneously, implementing parallel electrospinning setups, or optimizing the process for faster fiber formation. Improving the process efficiency and reducing the time required for fiber deposition contribute to enhanced scalability.
- Process control and automation: Implementing advanced process control and automation systems aids in scalability. Precise control over parameters such as solution flow rate, electric field strength, and

environmental conditions becomes crucial when dealing with large-scale production. Automation helps maintain consistency and reduces the potential for human errors.

- Quality control and characterization: Scalability should not compromise the quality and performance of the electrospun nanofibers. Adequate quality control measures should be established, including routine characterization of the fiber properties. Regular analysis of fiber diameter, morphology, mechanical properties, and functionality ensures consistency and adherence to specifications.
- Scalability in electrospinning requires a multidisciplinary approach, combining engineering, materials science, and process optimization. Advances in equipment design, process control, and automation are essential for achieving scalable electrospinning systems capable of producing high-quality nanofibers in large quantities to meet the demands of various industrial applications.

1.6.2. Fiber alignment control

Fiber alignment control is an important aspect of electrospinning, as it can significantly influence the mechanical, electrical, and functional properties of electrospun nanofibers. In some applications, it might be necessary to have control over the alignment and it is challenging to actively perfect alignment. Many parameters need to be considered [47, 60].

1.6.3. Reproducibility

In a significant portion of studies focused on electrospinning, the lack of controlled environmental conditions adds complexity to achieving consistent reproduction of experiments. As a result, the existing literature frequently provides inadequate details, contributing to a lack of well-defined and accurate electrospinning parameters.

Reproducibility in electrospinning can be improved by establishing standardized procedures and protocols. This includes documenting the process parameters, such as solution composition, flow rate, applied voltage, and collector

configuration. It is also crucial to have control over relative humidity since it affects the porosity. By following a consistent set of parameters, it becomes easier to reproduce the electrospinning process. reproducibility requires careful characterization and control of the materials used in electrospinning. Additionally, the properties of any additives or functional agents incorporated into the solution should be well characterized and controlled. Regular calibration and maintenance of electrospinning equipment are essential for achieving reproducible results. This includes verifying the accuracy of voltage and flow rate measurements, ensuring proper alignment of components, and checking for wear or damage. Consistent equipment performance contributes to the reproducibility of the electrospinning process.

1.7. Aims and objectives of this thesis

The aim of the thesis is to develop reliable and precise methods for mechanical (tensile) testing of nanofibers (Chapter 4) and individual fiber porosity (IFP) computation (Chapter 3). Both concepts are connected since individual fiber porosity has an influence on overall mechanical properties. For mechanical characterization, we use aligned fibers of nearly identical size and properties and then get collective mechanical behavior to infer the individual fiber properties. For IFP characterization, we focus on microscopy techniques (SEM and AFM). In this technique, the fiber's pores are collapsed by annealing, and the void fraction is computed using the unheated fiber's cross-sectional area. As a field of application of these nanofibers, we targeted tissue engineering where the mechanical properties of nanofibrous scaffolds are critical (Chapter 5). Cells respond differently to materials with different stiffness. Therefore, it is important to get information at individual fiber levels in order to estimate and simulate the overall mechanical properties of fibrous scaffolds.

1.8 Structure of this thesis

Chapter 1 provided a comprehensive overview of electrospinning, encompassing general information, fundamental concepts, various electrospinning types, nanofiber morphologies, and their diverse application areas.

In Chapter 2, an in-depth exploration of the electrospinning setups and unique configurations (co-axial gas flow, collector types) employed in this study will be presented.

Moving on to Chapter 3, the focus will shift towards internally porous fibers and their applications. The chapter will commence with an elucidation of their production methods, followed by several illustrative examples sourced from electrospinning literature. This chapter will provide a detailed description of the techniques and materials used for determining individual fiber porosity in PCL and PS (XRD, FIB, SEM, AFM, volume computation tools). Subsequently, the introduction of a novel method developed by us will take place. A comparative analysis between our method and the established pycnometry technique will also be included.

The forthcoming Chapter 4, first, the existing methods and challenges will be described. Following that, the details of the materials and methods of our new method for the characterization of tensile properties will be explained (sample preparation, mechanical testing, SEM, TGA, tensile modulus computation methods). This methodology will leverage the experimental data gathered in Chapter 3. Eventually, we will also compare our tensile test data with the bulk PCL data obtained from the literature.

Chapter 5 will center on the tissue engineering applications of electrospun fibers, particularly in the context of blood vessel tissue engineering. The process employed for creating a 3D rendering of electrospun nanofibers will be elaborated upon.

1.9. References

[1] Djafari Petroudy, S. R. (2017). Physical and mechanical properties of natural fibers. In *Advanced High Strength Natural Fibre Composites in Construction*. Elsevier Ltd. https://doi.org/10.1016/B978-0-08-100411-1.00003-0

[2] Sanjay, M. R., Arpitha, G. R., Naik, L. L., Gopalakrishna, K., & Yogesha, B. (2016). Applications of Natural Fibers and Its Composites: An Overview. *Natural Resources*, 07(03), 108–114. https://doi.org/10.4236/nr.2016.73011

[3] Monteiro, S. N., Satyanarayana, K. G., Ferreira, A. S., Nascimento, D. C. O., Lopes, F. P. D., Silva, I. L. A., Bevitori, A. B., Inácio, W. P., Bravo Neto, J., & Portela, T. G. (2010). Selection of high strength natural fibers. *Revista Materia*, 15(4), 488–505. https://doi.org/10.1590/S1517-70762010000400002

[4] Patterson, G. (2021). Cellulose before CELL: Historical themes. *Carbohydrate Polymers*, 252, 117182. https://doi.org/10.1016/j.carbpol.2020.117182

[5] Chatzi, E. G., & Koenig, J. L. (1987). Morphology and structure of kevlar fibers: A review. *Polymer-Plastics Technology and Engineering*, 26(3–4), 229–270. https://doi.org/10.1080/03602558708071938

[6] Cheng, M., Chen, W., & Weerasooriya, T. (2005). Mechanical properties of Kevlar® KM2 single fiber. *Journal of Engineering Materials and Technology*, 127(2), 197–203. https://doi.org/10.1115/1.1857937

[7] Qin, J., Guo, B., Zhang, L., Wang, T., Zhang, G., & Shi, X. (2020). Soft armor materials constructed with Kevlar fabric and a novel shear thickening fluid. *Composites Part B: Engineering*, 183(December 2019), 107686. https://doi.org/10.1016/j.compositesb.2019.107686

[8] Pan, J., Harb, C., Leng, W., & Marr, L. C. (2021). Inward and outward effectiveness of cloth masks, a surgical mask, and a face shield. *Aerosol Science and Technology*, 55(6), 718–733. https://doi.org/10.1080/02786826.2021.1890687

[9] Tucker, N., Stanger, J. J., Staiger, M. P., Razzaq, H., & Hofman, K. (2012). The history of the science and technology of electrospinning from 1600 to 1995. *Journal of Engineered Fibers and Fabrics*, 7(3), 63–73. https://doi.org/10.1177/155892501200702s10

[10] Xue, J., Wu, T., Dai, Y., & Xia, Y. (2019). Electrospinning and Electrospun Nanofibers: Methods, Materials, and Applications. *Chemical Reviews*, *119*(8), 5298–5415. https://doi.org/10.1021/acs.chemrev.8b00593

[11] Xue, J., Xie, J., Liu, W., & Xia, Y. (2017). Electrospun Nanofibers: New Concepts, Materials, and Applications. *Accounts of Chemical Research*, *50*(8), 1976–1987. https://doi.org/10.1021/acs.accounts.7b00218

[12] Reneker, D. H., & Yarin, A. L. (2008). Electrospinning jets and polymer nanofibers. *Polymer*, *49*(10), 2387–2425. https://doi.org/10.1016/j.polymer.2008.02.002

[13] Fambri, L., Pegoretti, A., Fenner, R., Incardona, S. D., & Migliaresi, C. (1997). Biodegradable fibres of poly(l-lactic acid) produced by melt spinning. *Polymer*, *38*(1), 79–85. https://doi.org/https://doi.org/10.1016/S0032-3861(96)00486-7

[14]Schmidt, J., Shenvi Usgaonkar, S., Kumar, S., Lozano, K., & Ellison, C. J. (2022). Advances in Melt Blowing Process Simulations. *Industrial and Engineering Chemistry Research*, *61*(1), 65–85. https://doi.org/10.1021/acs.iecr.1c03444

[15] Medeiros, E. S., Glenn, G. M., Klamczynski, A. P., Orts, W. J., & Mattoso, L. H. C. (2009). Solution blow spinning: A new method to produce micro- and nanofibers from polymer solutions. *Journal of Applied Polymer Science*, *113*(4), 2322–2330. https://doi.org/10.1002/app.30275

[16] Qu, H., & Skorobogatiy, M. (2015). *2 - Conductive polymer yarns for electronic textiles* (T. B. T.-E. T. Dias (ed.); pp. 21–53). Woodhead Publishing. https://doi.org/https://doi.org/10.1016/B978-0-08-100201-8.00003-5

[17] Um, I. C., Fang, D., Hsiao, B. S., Okamoto, A., & Chu, B. (2004). *Electro-Spinning and Electro-Blowing of Hyaluronic Acid*. 1428–1436.

[18] Elnabawy, E., Sun, D., Shearer, N., & Shyha, I. (2023). Electro-blown spinning: New insight into the effect of electric field and airflow hybridized forces on the production yield and characteristics of nanofiber membranes. *Journal of Science: Advanced Materials and Devices*, *8*(2), 100552. https://doi.org/10.1016/j.jsamd.2023.100552

[19] Cui, L., Song, Y., Wang, F., Sheng, Y., & Zou, H. (2019). Electrospinning synthesis of SiO2-TiO2 hybrid nanofibers with large surface area and excellent photocatalytic activity. *Applied Surface Science*, *488*(May), 284–292. https://doi.org/10.1016/j.apsusc.2019.05.151

[20] Zhang, Y., Shi, R., Yang, P., Song, X., Zhu, Y., & Ma, Q. (2016). Fabrication of electronspun porous CeO2 nanofibers with large surface area for pollutants removal. *Ceramics International*, *42*(12), 14028–14035. https://doi.org/10.1016/j.ceramint.2016.06.00

[21] Wang, H., Niu, H., Wang, H., Wang, W., Jin, X., Wang, H., Zhou, H., & Lin, T. (2021). Micro-meso porous structured carbon nanofibers with ultra-high surface area and large supercapacitor

electrode capacitance. *Journal of Power Sources*, *482*(August 2020), 228986. https://doi.org/10.1016/j.jpowsour.2020.228986

[22] He, J.-H., Wan, Y.-Q., & Xu, L. (2007). Nano-effects, quantum-like properties in electrospun nanofibers. *Chaos, Solitons & Fractals*, *33*(1), 26–37. https://doi.org/https://doi.org/10.1016/j.chaos.2006.09.023

[23] Wingert, M. C., Jiang, Z., Chen, R., & Cai, S. (2017). Strong size-dependent stress relaxation in electrospun polymer nanofibers. *Journal of Applied Physics*, *121*(1), 15103. https://doi.org/10.1063/1.4973486

[24] Hu, X., Liu, S., Zhou, G., Huang, Y., Xie, Z., & Jing, X. (2014). Electrospinning of polymeric nanofibers for drug delivery applications. *Journal of Controlled Release*, *185*, 12–21. https://doi.org/https://doi.org/10.1016/j.jconrel.2014.04.018

[25] Ahmed, F. E., Lalia, B. S., & Hashaikeh, R. (2015). A review on electrospinning for membrane fabrication: Challenges and applications. *Desalination*, *356*, 15–30. https://doi.org/https://doi.org/10.1016/j.desal.2014.09.033

[26] Huang, Z.-M., Zhang, Y.-Z., Kotaki, M., & Ramakrishna, S. (2003). A review on polymer nanofibers by electrospinning and their applications in nanocomposites. *Composites Science and Technology*, *63*(15), 2223–2253. https://doi.org/https://doi.org/10.1016/S0266-3538(03)00178-7

[27] Kumar, P. S., Sundaramurthy, J., Sundarrajan, S., Babu, V. J., Singh, G., Allakhverdiev, S. I., & Ramakrishna, S. (2014). Hierarchical electrospun nanofibers for energy harvesting, production and environmental remediation. *Energy & Environmental Science*, *7*(10), 3192–3222. https://doi.org/10.1039/C4EE00612G

[28] Chen, X., Cao, H., He, Y., Zhou, Q., Li, Z., Wang, W., He, Y., Tao, G., & Hou, C. (2022). Advanced functional nanofibers: strategies to improve performance and expand functions. *Frontiers of Optoelectronics*, *15*(1), 1–19. https://doi.org/10.1007/s12200-022-00051-2

[29] Rahmati, M., Mills, D. K., Urbanska, A. M., Saeb, M. R., Venugopal, J. R., Ramakrishna, S., & Mozafari, M. (2021). Electrospinning for tissue engineering applications. *Progress in Materials Science*, *117*, 100721. https://doi.org/10.1016/j.pmatsci.2020.100721

[30] Gao, C., Peng, S., Feng, P., & Shuai, C. (2017). Bone biomaterials and interactions with stem cells. *Bone Research*, *5*(May), 1–33. https://doi.org/10.1038/boneres.2017.59

[31] Venugopal, J., Low, S., Choon, A. T., Sampath Kumar, T. S., & Ramakrishna, S. (2008). Mineralization of osteoblasts with electrospun collagen/hydroxyapatite nanofibers. *Journal of*

Materials Science: Materials in Medicine, *19*(5), 2039–2046. https://doi.org/10.1007/s10856-007-3289-x

[32] Ao, C., Niu, Y., Zhang, X., He, X., Zhang, W., & Lu, C. (2017). Fabrication and characterization of electrospun cellulose/nano-hydroxyapatite nanofibers for bone tissue engineering. *International Journal of Biological Macromolecules*, *97*, 568–573. https://doi.org/10.1016/j.ijbiomac.2016.12.091

[33] Novotna, K., Zajdlova, M., Suchy, T., Hadraba, D., Lopot, F., Zaloudkova, M., Douglas, T. E. L., Munzarova, M., Juklickova, M., Stranska, D., Kubies, D., Schaubroeck, D., Wille, S., Balcaen, L., Jarosova, M., Kozak, H., Kromka, A., Svindrych, Z., Lisa, V., … Bacakova, L. (2014). Polylactide nanofibers with hydroxyapatite as growth substrates for osteoblast-like cells. *Journal of Biomedical Materials Research - Part A*, *102*(11), 3918–3930. https://doi.org/10.1002/jbm.a.35061

[34] Hartman, R. P. A., Brunner, D. J., Camelot, D. M. A., Marijnissen, J. C. M., & Scarlett, B. (1999). Electrohydrodynamic atomization in the cone–jet mode physical modeling of the liquid cone and jet. *Journal of Aerosol Science*, *30*(7), 823–849. https://doi.org/10.1016/S0021-8502(99)00033-6

[35] Bodnár, E., Grifoll, J., & Rosell-Llompart, J. (2018). Polymer solution electrospraying: A tool for engineering particles and films with controlled morphology. *Journal of Aerosol Science*, *125*, 93–118. https://doi.org/10.1016/j.jaerosci.2018.04.012

[36] Liu, F., & Chen, C.-H. (2014). Electrohydrodynamic cone-jet bridges: Stability diagram and operating modes. *Journal of Electrostatics*, *72*(4), 330–335. https://doi.org/10.1016/j.elstat.2014.05.004

[37] Aramide, B., Kothandaraman, A., Edirisinghe, M., Jayasinghe, S. N., & Ventikos, Y. (2019). General Computational Methodology for Modeling Electrohydrodynamic Flows: Prediction and Optimization Capability for the Generation of Bubbles and Fibers. *Langmuir*, *35*(31), 10203–10212. https://doi.org/10.1021/acs.langmuir.8b03763

[38] Taylor, G., & A, P. R. S. L. (1964). Disintegration of water drops in an electric field. *Proceedings of the Royal Society of London. Series A. Mathematical and Physical Sciences*, *280*(1382), 383–397. https://doi.org/10.1098/rspa.1964.0151

[39] Larrondo, L., & Manley, R. S. J. (1981). Electrostatic Fiber Spinning From Polymer Melts - 3. Electrostatic Deformation of a Pendant Drop of Polymer Melt. *Journal of Polymer Science. Part A-2, Polymer Physics*, *19*(6), 933–940. https://doi.org/10.1002/pol.1981.180190603

[40] Yarin, A. L., Koombhongse, S., & Reneker, D. H. (2001). Taylor cone and jetting from liquid droplets in electrospinning of nanofibers. *Journal of Applied Physics*, *90*(9), 4836–4846. https://doi.org/10.1063/1.1408260

[41] Garg, K., & Bowlin, G. L. (2011). Electrospinning jets and nanofibrous structures. *Biomicrofluidics*, *5*(1). https://doi.org/10.1063/1.3567097

[42] Deitzel, J. M., Kleinmeyer, J., Harris, D., & Beck Tan, N. C. (2001). The effect of processing variables on the morphology of electrospun. *Polymer*, *42*, 261–272.

[43] Hager, B. L., & Berry, G. C. (1982). Moderately concentrated solutions of polystyrene. I. Viscosity as a function of concentration, temperature, and molecular weight. *Journal of Polymer Science: Polymer Physics Edition*, *20*(5), 911–928. https://doi.org/https://doi.org/10.1002/pol.1982.180200513

[44] Gupta, P., Elkins, C., Long, T. E., & Wilkes, G. L. (2005). Electrospinning of linear homopolymers of poly(methyl methacrylate): Exploring relationships between fiber formation, viscosity, molecular weight and concentration in a good solvent. *Polymer*, *46*(13), 4799–4810. https://doi.org/10.1016/j.polymer.2005.04.021

[45] Pelipenko, J., Kristl, J., Janković, B., Baumgartner, S., & Kocbek, P. (2013). The impact of relative humidity during electrospinning on the morphology and mechanical properties of nanofibers. *International Journal of Pharmaceutics*, *456*(1), 125–134. https://doi.org/10.1016/j.ijpharm.2013.07.078

[46] Demir, M. M. (2010). Investigation on glassy skin formation of porous polystyrene fibers electrospun from DMF. *Express Polymer Letters*, *4*(1), 2–8. https://doi.org/10.3144/expresspolymlett.2010.2

[47] Kiselev, P., & Rosell-Llompart, J. (2012). Highly aligned electrospun nanofibers by elimination of the whipping motion. *Journal of Applied Polymer Science*, *125*(3), 2433–2441. https://doi.org/10.1002/app.36519

[48] Mailley, D., Hébraud, A., & Schlatter, G. (2021). A Review on the Impact of Humidity during Electrospinning: From the Nanofiber Structure Engineering to the Applications. *Macromolecular Materials and Engineering*, *306*(7), 1–25. https://doi.org/10.1002/mame.202100115

[49] Li, D., & Xia, Y. (2004). Electrospinning of nanofibers: Reinventing the wheel? *Advanced Materials*, *16*(14), 1151–1170. https://doi.org/10.1002/adma.200400719

[50] Bhardwaj, N., & Kundu, S. C. (2010). Electrospinning: A fascinating fiber fabrication technique. *Biotechnology Advances*, *28*(3), 325–347. https://doi.org/10.1016/j.biotechadv.2010.01.004

[51] He, X. X., Zheng, J., Yu, G. F., You, M. H., Yu, M., Ning, X., & Long, Y. Z. (2017). Near-Field Electrospinning: Progress and Applications. *Journal of Physical Chemistry C*, *121*(16), 8663–8678. https://doi.org/10.1021/acs.jpcc.6b12783

[52] Teo, W. E., Ramakrishna, S., & A. (2013). Near-field electrospinning: Progress and applications. Nanoscale, 5(1), 83-120.

[53] Liashenko, I., Ramon, A., Cabot, A., & Rosell-Llompart, J. (2021). Ultrafast electrohydrodynamic 3D printing with in situ jet speed monitoring. *Materials & Design*, *206*, 109791. https://doi.org/10.1016/j.matdes.2021.109791

[54] Dalton, P. D. (2017). Melt electrowriting with additive manufacturing principles. *Current Opinion in Biomedical Engineering*, *2*, 49–57. https://doi.org/10.1016/j.cobme.2017.05.007

[55] Yang, Z., Peng, H., Wang, W., & Liu, T. (2010). Crystallization behavior of poly(ε-caprolactone)/layered double hydroxide nanocomposites. *Journal of Applied Polymer Science*, *116*(5), 2658–2667. https://doi.org/10.1002/app

[56] Khalf, A., & Madihally, S. V. (2017). Recent advances in multiaxial electrospinning for drug delivery. *European Journal of Pharmaceutics and Biopharmaceutics*, *112*, 1–17. https://doi.org/10.1016/j.ejpb.2016.11.010

[57] Beaudoin, É. J., Kubaski, M. M., Samara, M., Zednik, R. J., & Demarquette, N. R. (2022). Scaled-Up Multi-Needle Electrospinning Process Using Parallel Plate Auxiliary Electrodes. *Nanomaterials*, *12*(8). https://doi.org/10.3390/nano12081356

[58] Xie, S., & Zeng, Y. (2012). Effects of electric field on multineedle electrospinning: Experiment and simulation study. *Industrial and Engineering Chemistry Research*, *51*(14), 5336–5345. https://doi.org/10.1021/ie2020763

[59] Niu, H., & Lin, T. (2012). Fiber generators in needleless electrospinning. *Journal of Nanomaterials*, *2012*. https://doi.org/10.1155/2012/725950

[60] Han, W. H., Wang, M. Q., Yuan, J. X., Hao, C. C., Li, C. J., Long, Y. Z., & Ramakrishna, S. (2022). Electrospun aligned nanofibers: A review. *Arabian Journal of Chemistry*, *15*(11), 104193. https://doi.org/10.1016/j.arabjc.2022.104193

[61] Li, D., Ouyang, G., McCann, J. T., & Xia, Y. (2005). Collecting electrospun nanofibers with patterned electrodes. *Nano Letters*, *5*(5), 913–916. https://doi.org/10.1021/nl0504235

[62] Zaarour, B., Zhu, L., & Jin, X. (2020). A Review on the Secondary Surface Morphology of Electrospun Nanofibers: Formation Mechanisms, Characterizations, and Applications. *ChemistrySelect*, *5*(4), 1335–1348. https://doi.org/10.1002/slct.201903981

[63] Li, M., Mondrinos, M. J., Gandhi, M. R., Ko, F. K., Weiss, A. S., & Lelkes, P. I. (2005). Electrospun protein fibers as matrices for tissue engineering. *Biomaterials*, *26*(30), 5999–6008. https://doi.org/10.1016/j.biomaterials.2005.03.030

[64] Rnjak-Kovacina, J., Wise, S. G., Li, Z., Maitz, P. K. M., Young, C. J., Wang, Y., & Weiss, A. S. (2012). Electrospun synthetic human elastin:collagen composite scaffolds for dermal tissue engineering. *Acta Biomaterialia*, *8*(10), 3714–3722. https://doi.org/10.1016/j.actbio.2012.06.032

[65] Tian, Y., Wang, Z., & Wang, L. (2021). Hollow fibers: From fabrication to applications. *Chemical Communications*, *57*(73), 9166–9177. https://doi.org/10.1039/d1cc02991f

Chapter 2. Electrospinning Equipment Used

The goal of this chapter is to describe the electrospinning setup used in this thesis, to obtain fibers for the mechanical and porosity tests described in chapters 3 and 4.

In our studies, we used three different purpose-made setups for electrospun nanofiber fabrication: a stationary collector-based setup for randomly oriented fiber, a collector with a shutter for single fiber collection, and setup with wire-drum for aligned fibers collection (Explained in section 2.3). An important part of experimentation is safety; therefore, we addressed this topic in the setup design, as explained in section 2.1.

2.1. Safety considerations

Electrospinning involves working with high voltages, solvents, and potentially hazardous materials. Safety measures and precautions are crucial to ensure the well-being of researchers and prevent accidents. This section will address the safety considerations associated with electrospinning, including electrical safety, chemical hazards, and personal protective equipment (PPE) requirements.

Electrospinning involves the use of high voltages, which can generate static electricity. It is important to make sure to ground yourself and the equipment properly to minimize the risk of electrostatic discharge.

Proper grounding of equipment and personnel is essential to prevent the buildup of static electricity. All components of the electrospinning setup should be grounded. When working with electrospinning setups, safety resistors can play a crucial role in ensuring electrical safety. Safety resistors are often used to bleed off excess charge or limit the current flow in electrical circuits to prevent electrical hazards.

Electrospinning experiments should be performed in a well-ventilated area or under a fume hood to ensure the dispersion of any fumes or particles that may be generated during the process.

Depending on the materials being used, there may be chemical hazards associated with the electrospinning process. It is important to be aware of the properties of

the materials you are working with and follow appropriate handling, storage, and disposal procedures.

2.2. Co-axial gas jacket

In our work we have used various solvents such as acetone, DMF, chloroform, methanol. In the experiments where acetone and chloroform/methanol were used, we needed a co-axial gas jacket saturated with the solvent in order to prevent premature drying on the tip of the needle.

In electrospinning, one of the main challenges is to obtain a steady-state condition, which means having an electrospinning process with no interruptions, and no blockage of the needle by the polymeric solution [1,2,3]. When the solvent evaporates quickly during electrospinning, often polymer will accumulate, eventually clogging the needle, which either stops the entire process or creates unstable electrospinning conditions [4,5].

To avoid this problem, one could use non-volatile solvents. However, that cannot always be the case, and depending on the target application sometimes it is necessary to use volatile solvents.

Larsen et al. suggested a method that makes the process continuous and stable, thereby avoiding the need for periodic clean-up of the needle. In this method, a solvent-saturated co-axial flow tube surrounds the needle and protects the jet from premature drying [6]. They showed the difference in jet formation when co-flow was used. Figure 2.1a shows the electrospinning jet when a solvent-saturated N_2 flow in the jacket was used. Figure 2.1d shows the jet for the same voltage but without co-flow. Panels 2.1b and c, show jet initiation in the presence of co-flow, however, it has not reached the critical voltage to form a Taylor cone.

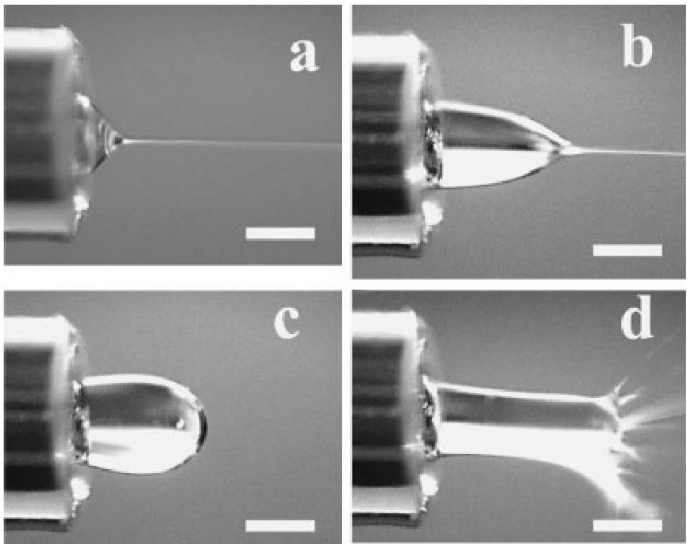

Figure 2.1. Taylor cone structure at the tip of a 10 wt.-% PLA in DCM solution. Applied voltages: a) 1.2, b) 0.8, and c) 0.6 kVcm±1, with a solvent-saturated N_2 flow in the jacket, and d) 1.2 without gas flow in the jacket. The scale bar is 300 μm. Adapted with permission from Ref. [6].

It's important to note that co-axial electrospinning setups can be more complex than traditional single-nozzle electrospinning setups, requiring precise control of both the core solution and the gas flow. Proper design, setup, and control are essential for achieving the desired results (Figure 2.2).

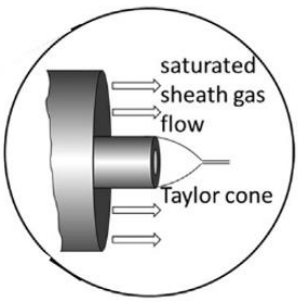

Figure 2.2 Illustration of saturated gas flow around the needle. Adapted with permission from Ref. [7]

Recently, Lübbert and Peukert [7] suggested a new method for co-axial gas jackets where they had a new vial configuration for saturating nitrogen with the solvent (Figure 2.3). This saturation technique enables the saturation of a gas stream to exceptionally high saturation ratios, eliminating the potential for supersaturation

or gas contamination due to droplets (unlike the situation with bubblers/impingers). Additionally, this method is applicable for saturating a gas flow with solvent mixtures. A performance assessment of the saturator arrangement reveals that the saturation ratio upon exiting the third saturator is anticipated to exceed 99%.

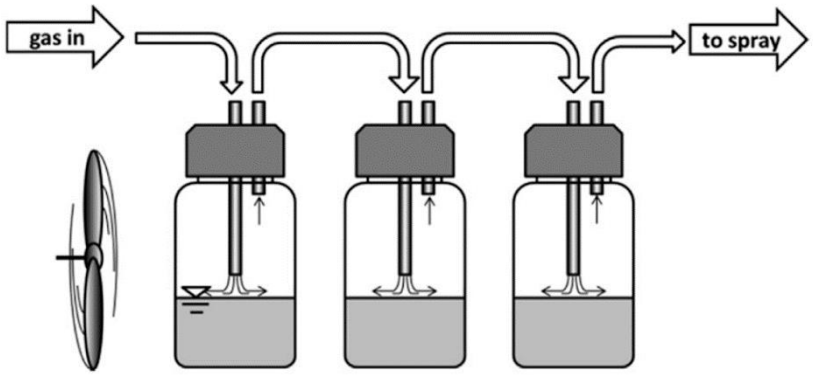

Figure 2.3. The new vial configuration was suggested by Lübbert and Peukert (2018). In our experiments, we used this configuration for co-axial flow. Adapted with permission from Ref. [7].

The co-axial gas flow also helps not only in preventing the polymer solution drying but also in controlling the stretching and alignment of the fibers. This can lead to more uniform and controlled fiber diameters, which is crucial for certain applications. The co-axial gas flow can help stabilize the spinning jet and reduce the occurrence of whipping and other instabilities that can impact fiber uniformity. Therefore, Kiselev and Rosell-Llompart used a co-axial gas flow *without* solvent saturation to shield the meniscus from the ambient air. Since their solvent was non-volatile, drying or clogging was not observed even without solvent saturation in the co-axial gas flow [8].

In our experiments, we clearly saw the difference when co-axial gas flow was used. PCL/(methanol/chloroform) solution dried on the tip of the needle when co-axial gas flow was not used (Figure 2.4a and b). However, we could reach steady-state,

uninterrupted electrospinning when co-axial gas flow was used (Figure 2.4c). In both cases, the voltage is about 15V.

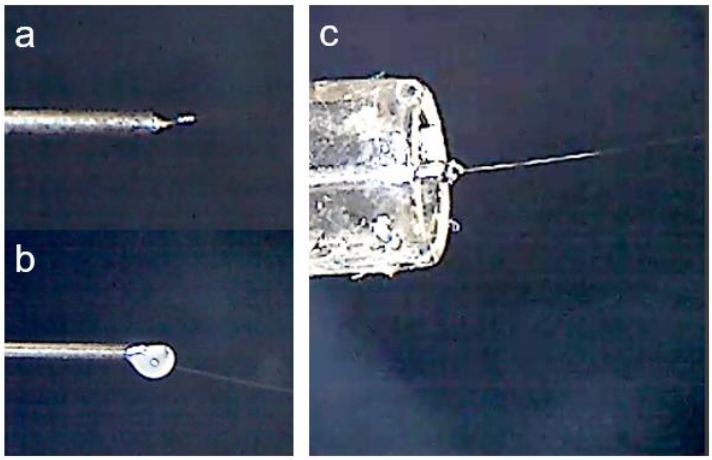

Figure 2.4. a) Polymer solution starting to dry up on the tip. c) Polymer solution accumulates due to the blockage. c) Steady-state electrospinning with co-axial gas flow.

2.3. Electrospinning setups used

2.3.1. Setup for randomly oriented fibers

In some of our experiments, to produce randomly oriented fibers, we used a flat brass collector. The configuration is shown in Figure 2.5. Due to the whipping motion, the fiber lands on the collector in a random manner. We used a syringe pump in a horizontal setting as shown in Figure. The brass collector was covered in Aluminum foil. When needed, we used a solvent-saturated N_2 co-axial flow depending on the solvent system we used. For example, we used it for the experiments done with poly (e-caprolactone) (methanol/chloroform) since the solvent was very volatile. In this case, the gas was saturated only with chloroform. In our polystyrene experiments, we did not use co-flow since the solvent has a high boiling point. We could reach steady state without the gas flow around the needle.

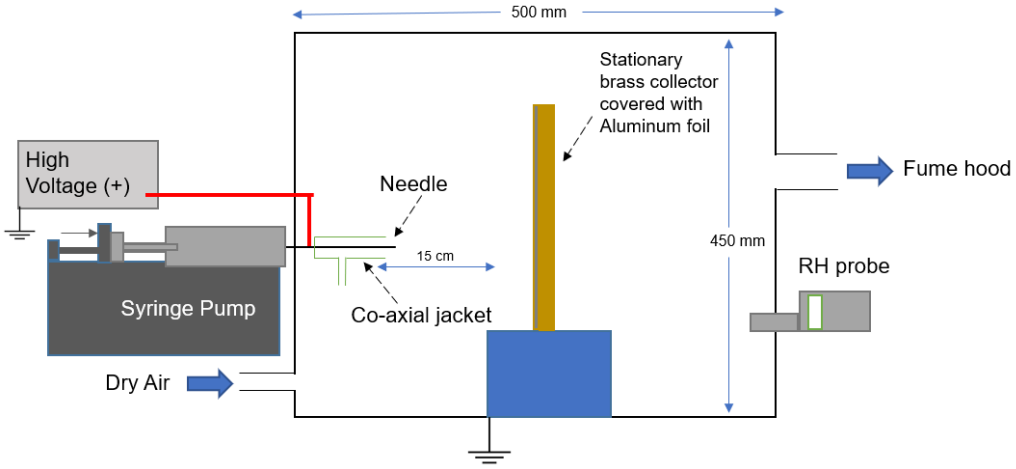

Figure 2.5. Setup with the stationary collector for obtaining randomly oriented fibers.

2.3.2. Setup for single fiber collection

For individual fiber porosity (IFP) determination experiments, we used a purpose-made collector where we can collect individual fibers with minimum manipulation. This collector had a slit where the transient collection occurs (fibers collected before reaching a steady-state electrospinning), and after reaching a steady-state, we open the paper cover and let the "stable" fibers collected on the other part of the collector (Figure 2.6). This way we make sure that all the individual fiber samples we prepare are prepared under the same parameters.

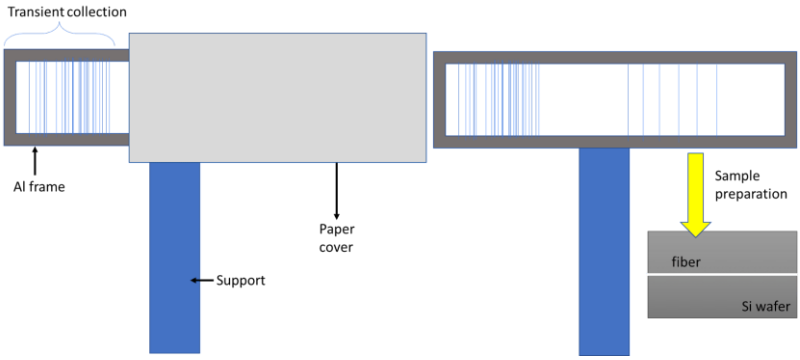

Figure 2.6. Illustration of the single fiber collection

The more detailed images of the purpose-made collector are shown in Figure 2.7 with the slit open and closed, along with accompanying technical drawings.

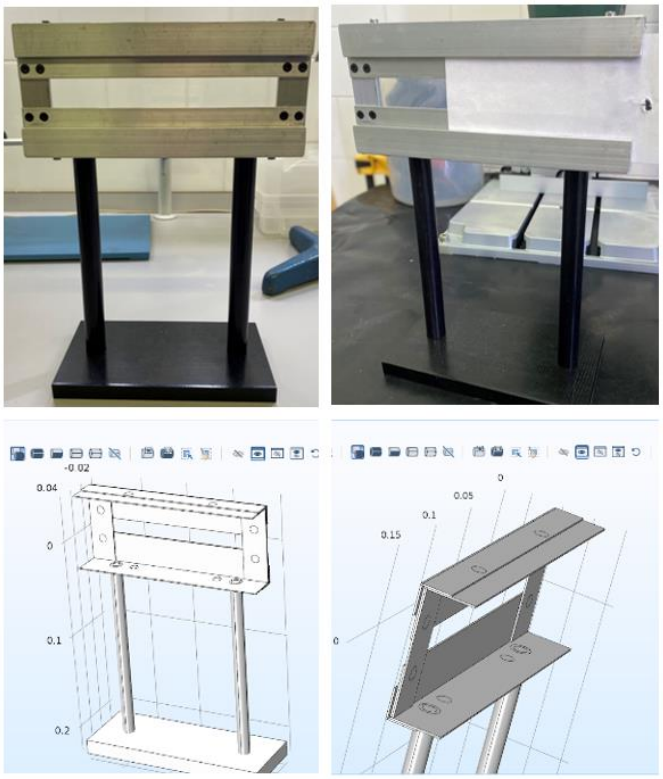

Figure 2.7. Collector design for single fiber collection.

2.3.3. Setup for aligned fibers collection

To collect aligned fibers, we used a drum made of wires that we control from outside the chamber (Figure 2.8). This configuration was chosen instead of the commonly used solid cylinder to facilitate removing the fibers from the wire drum. We also used a back-plate electrode behind the needle, as well as the top electrode, in order to navigate the fibers toward the collector. Two high-voltage supplies were used, one of them was connected to the top electrode, and the other one was connected to both the back electrode and needle. Dry air was sent to the chamber and extracted by a fan. A relative humidity tool was inserted into the chamber through a well-sealed hole. Nitrogen gas was sent to the co-axial gas tube through three vials full of solvent of interest.

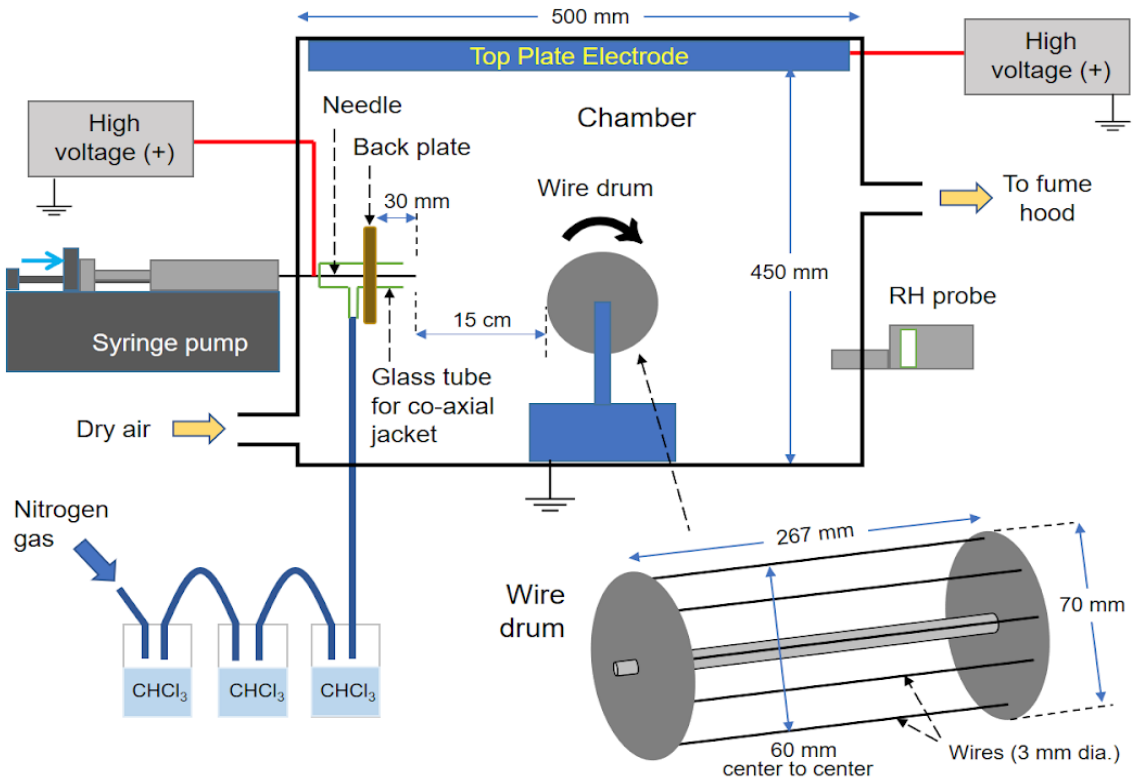

Figure 2.8. Setup for aligned fiber collection.

2.4. References

[1] Reneker, D. H., & Yarin, A. L. (2008). Electrospinning jets and polymer nanofibers. *Polymer*, 49(10), 2387–2425. https://doi.org/10.1016/j.polymer.2008.02.002

[2] Darko, G., Goethals, A., Torto, N., & De Clerck, K. (2016). Steady state electrospinning of uniform polyethersulfone nanofibers using a non-heated solvent mixture. *Applied Nanoscience (Switzerland)*, 6(6), 837–845. https://doi.org/10.1007/s13204-015-0504-9

[3] Van Der Schueren, L., De Schoenmaker, B., Kalaoglu, Ö. I., & De Clerck, K. (2011). An alternative solvent system for the steady state electrospinning of polycaprolactone. *European Polymer Journal*, 47(6), 1256–1263. https://doi.org/10.1016/j.eurpolymj.2011.02.025

[4] Zeng, J., Chen, X., Xu, X., Liang, Q., Bian, X., Yang, L., & Jing, X. (2003). Ultrafine fibers electrospun from biodegradable polymers. *Journal of Applied Polymer Science*, 89(4), 1085–1092. https://doi.org/10.1002/app.12260

[5] Megelski, S., Stephens, J. S., Bruce Chase, D., & Rabolt, J. F. (2002). Micro- and nanostructured surface morphology on electrospun polymer fibers. *Macromolecules*, 35(22), 8456–8466. https://doi.org/10.1021/ma020444a

[6] Larsen, G., Spretz, R., & Velarde-Ortiz, R. (2004). Use of coaxial gas jackets to stabilize Taylor cones of volatile solutions and to induce particle-to-fiber transitions. *Advanced Materials*, 16(2), 166–169. https://doi.org/10.1002/adma.200306021

[7] Lübbert, C., & Peukert, W. (2018). The mass transfer at Taylor cones. *Journal of Aerosol Science*, 123, 39–51. https://doi.org/10.1016/j.jaerosci.2018.05.014

[8] Kiselev, P., & Rosell-Llompart, J. (2012). Highly aligned electrospun nanofibers by elimination of the whipping motion. *Journal of Applied Polymer Science*, 125(3), 2433–2441. https://doi.org/10.1002/app.36519

Chapter 3. Porosity determination of single fibers

3.1. Introduction

3.1.1 Definitions

Porous fibers have a wide range of application areas such as oil absorption, tissue engineering, drug delivery, batteries, etc. [1,2,3,4]. In electrospinning, depending on the solvent system, ambient conditions or processing parameters, internally porous fibers can be obtained [5]. It is important to clarify the difference in types of porosity. While inter-fiber porosity, or "mat porosity" (Figure 3.1a), is defined as the voids between electrospun fibers inside a membrane, intra-fiber (Figure 3.1b) porosity can be classified into two types: surface and internal (or interior) porosity. (Figure 3.1c, d) In electrospinning literature, "intra-fiber" porosity, also known as "interior" or "internal" fiber porosity, has received much less attention than the "mat porosity". The surface porosity includes all the pores in the shell along the length of the fibers and internal porosity involves the porous inside the fibers that can be also called "interior porosity" or "in-fiber porosity" In our experiments, we will call it *individual fiber porosity (IFP)* to make a clear distinction**.** We can formulate it as *porosity = void fraction of the fiber/ total volume of the fiber.*

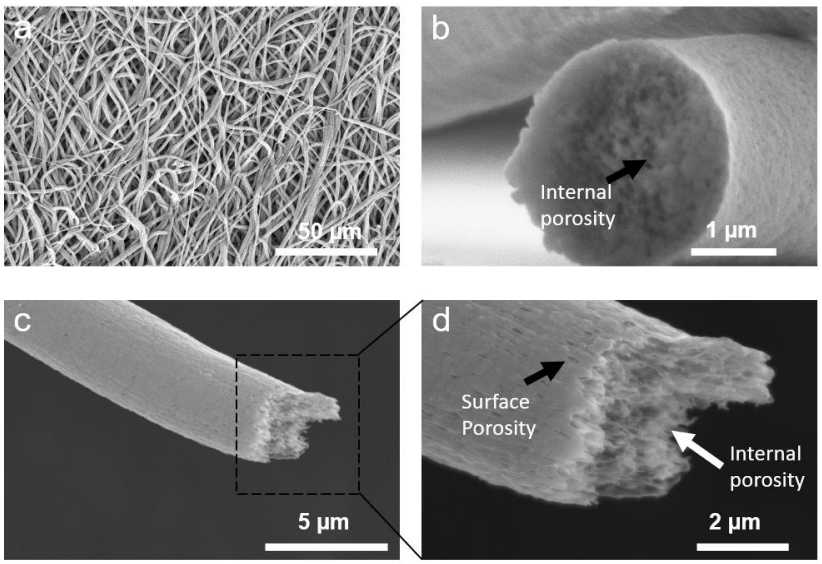

Figure 3.1. a) Mat Porosity b) internal porosity c) fiber with internal and surface porosity d) zoom-in image of (c)

3.1.2. Role of fiber porosity in applications

One of the greatest challenges in recent studies is to determine how to control the internal fiber porosity and demonstrate the influence of pores in specific applications. These applications can be listed as follows:

Oil Sorption

Polymeric fibers produced by electrospinning have been widely used in oil sorption applications due to their high surface area, low cost, and scalability. Nonwoven polypropylene (PP) fibers have been commercially used as oil sorbents due to their oleophilic-hydrophobic properties, however, they suffer from low oil sorption capacity since they are usually made of compact PP fibers. Therefore, finding alternative materials and tailoring the nanoporous structure of the fibers has been an interesting research field. In a study by Lin et al., nanoporous polystyrene fibers were developed and compared to PP fibers, revealing a notable 3-4 times enhancement in sorption capacity [6].

Bandegi and Moghbeli conducted another example of applying porous fibers for oil sorption. They investigated how solvents and humidity influenced the creation of porosity within electrospun nanofibers made from styrene/acrylonitrile copolymer (SAN). The outcome was that porous SAN nanofibers exhibited greater oil absorbency compared to their non-porous counterparts [7].

The advantageous aspect of having both internal and surface porosity for oil adsorption was highlighted by Isık and Demir. They detailed their work on customizing the morphology of individual electrospun fibers to achieve enhanced oil absorption. To this end, they experimented with five varying concentrations of foam-expanded polystyrene (f-PS). Their findings demonstrated that fibers possessing interior porosity and textured surfaces displayed remarkable adsorption capacity [8].

Zaarour et al. contributed to this field through a noteworthy study involving polyvinylidene fluoride (PVDF) nanofibers. By manipulating relative humidity levels and solvent mixture ratios, they generated fibers with diverse surface morphologies such as porous, rough, grooved, and internally porous structures. Notably, fibers with a macro-porous structure exhibited the highest oil absorption capacity [9].

The exploration of ultrahigh oil (silicone oil, pump oil, sunflower oil, and diesel) adsorption capability was undertaken by Chen and Tung. They accomplished various morphologies of polystyrene (PS) electrospun fibers using a one-step electrospinning method with differing solvent/nonsolvent mixture ratios. Additionally, they observed that introducing microscale voids within fiber structures led to rapid adsorption coupled with a high adsorption capability [10].

Photocatalytic activity

A photocatalyst is a material that absorbs light to bring it to a higher energy level and provides such energy to a reacting substance to make a chemical reaction occur. These catalyst powders are easy to aggregate in the effluent, resulting in a laborious separation process after their usage. The inevitable loss of some fine powders during the process can cause contamination. Therefore, immobilizing catalyst powders in electrospun fibers has been an appealing research area. Immobilized catalysts can be made either by mixing the nanoparticles with the electrospinning solution [11] or by coating the electrospun fibers with nanoparticles afterward [12]. One unique property of electrospun fibers is their high inter-fiber porosity which provides an increase in the specific surface area alongside a higher photocatalytic activity. The catalysis field is another profitable field because of the high activity and stability of internally porous nanofibers compared to compact fibers.

Hou et al. produced hierarchically porous TiO_2/SiO_2 fibers (Figure 3.2) in order to enhance the photocatalytic activity, avoiding the separation problems of TiO_2 which tends to aggregate without the fiber matrix. In this study, thanks to the

porous structure, fibers were capable of keeping all the advantages of nanoparticles (high efficiency, low cost, chemical inertness, and high surface area), but also helped to create a uniform spatial TiO_2 distribution [11].

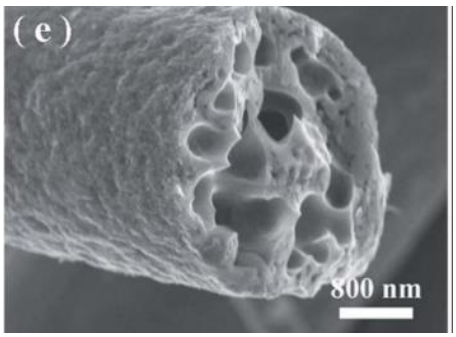

Figure 3.2. Porous TiO_2/SiO_2 fibers for photocatalytic activity. Adapted with permission from Ref. [11].

Ning et al. produced PVDF nanoporous fibers and coated them with Ag nanoparticles. The porous structure of the electrospun fibers facilitates nanoparticle adsorption on the surface [12].

Tissue Engineering

Porous fibers are widely used in tissue engineering and regenerative medicine. The porous morphology of the fibers can change the mechanical properties, water contact angle, and cell attachment. Therefore, several studies have been carried out on these topics.

Previous studies have demonstrated that the modification of the morphology of individual fibers in electrospun scaffolds can directly affect cellular response. Moroni et al. reported that the fibers with nanoporous structure resulted in more spread cells throughout the electrospun mat (Figure 3.3b), whereas cells were aggregated when the fibers were not porous (Figure 3.3a) [13]. Similarly, Liao et al

claimed to enhance the cell adhesion by using nanoporous fibers as a scaffold for bone tissue engineering [14].

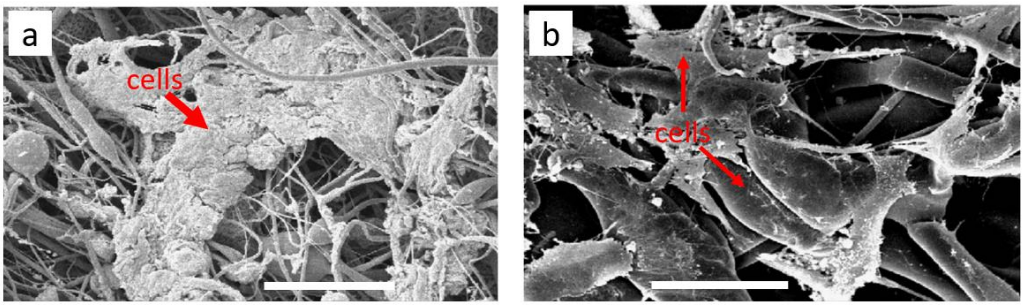

Figure 3.3. Different cell responses to smooth (a) and porous (b) fibers. The scale bar is 50 μm. Adapted with permission from Ref. [13].

Mota et al. reported a published study in the tissue engineering field with the aim to develop electrospun microstructures with a layer-by-layer control for the well-defined internal architecture and external shape of the scaffolds. Referring to the highly porous morphology of the nanofibers, several advantages are found, such as the biodegradation rate, the mass transfer associated with cell metabolism, and the mechanisms regulating cell adhesion and proliferation. All of them are crucial for the enhanced development of the bone scaffolds inside the human body. The resulting scaffolds were composed of aligned fibers with a highly porous morphology, both in the cross-section and on the outer surface [15].

Drug Delivery

Another advantageous application of porous fibers is biodegradable drug delivery owing to the enhancement of diffusion and fluid transport. High surface porosity fibers (or porous fibers) enable modification and control of the wetting processes, adsorption/absorption as well as the release behavior of drugs. Nguyen et al. observed large amounts of drug release from porous fibers compared to those that are not porous [16].

Similarly, Ramos et.al reported that porous fibers are able to release double the amount of drugs compared to non-porous fibers (Figure 3.4) [3].

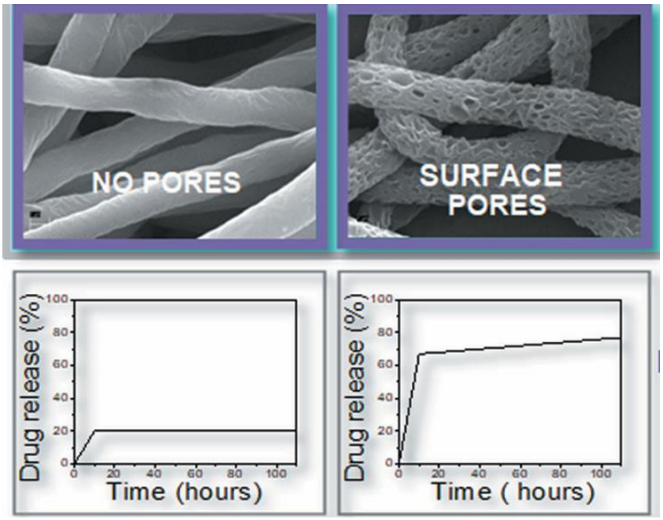

Figure 3.4. The difference in drug release between non-porous fibers and porous fibers. Adapted with permission from Ref. [3]

Lithium-Ion Batteries

Electrospun nanofibers allow rapid transformation of electrons and ions, in addition, the void spaces in the porous nanofibers can effectively buffer the expansion of volume during the process of charging and discharging the electrode material. Therefore, they are good candidates for lithium-ion battery applications. Sabetzadeh et al. reported the crucial role of the highly polyacrylonitrile porous (PAN) nanofibers as separators in order to facilitate and enhance ion migration due to their higher discharge capacity. The high porosity of the porous PAN micro/nanofiber membranes caused excellent electrolyte uptake and led to great ionic conductivity of electrolyte-soaked porous PAN micro/nanofiber membranes [17].

Textile Membranes

Intra-fiber porosity is an important parameter that can directly influence the wicking features of textiles. It is believed that the smaller the size of the pores, the higher the capillary force and wicking rate, and vice versa. Thus, porous fiber structure along with regulated inter-fiber pores would not only lead to high moisture wicking but would also support the rate of evaporation to facilitate the drying process. Hence, it's essential to investigate the effect of inter- and intra-fiber porosity on the moisture management performance of the textiles. Yan et al. reported inter- and intra-fiber porous membranes for enhanced directional moisture transport in a dual layer for sportswear in order to transfer the humidity from the skin to the atmosphere and avoid reverse transport. Porous morphology showed an increased hydrophilicity and higher evaporation rate [18].

Gas Sensing

The paper by Kim et al. (2020) presents a novel approach to improving the performance of a gas sensor by utilizing a nanoporous polymer fiber reinforced with Cellulose Nanocrystals (CNCs). The study focuses on enhancing the sensor's porosity to achieve better sensitivity and response time simultaneously. Traditional attempts to improve these two factors often led to trade-offs, but the introduced CNC-reinforced nanoporous fiber overcomes this challenge. The crystalline and hygroscopic properties of CNCs contribute to the formation of nanoporous structures in the fiber, resulting in increased surface area and improved response time. This innovative approach not only enhances gas sensor performance but also holds promise for broader applications in fields like food fermentation quality control and gas separation membranes. [19].

Biosensing

Biosensing is a field that also benefits from the intra-fiber and surface porosity of electrospun nanofibers. Thereby, Nathani and Sharma published an article about

the increase of sensitivity of porous poly(styrene-block-methyl-methacrylate) for electrochemical biosensors [20].

Another example of wearable sensors for the trace detection of chemical and biological molecules was conducted by Chen et al. The large amounts of holes in the fibers greatly improve the sample collection efficiency of the SERS-active substrate and facilitate the adsorption of analytes on the surface of silver nanowires. The porous structure of fibers facilitates it to be combined with silver nanowires (Figure 3.5) [21].

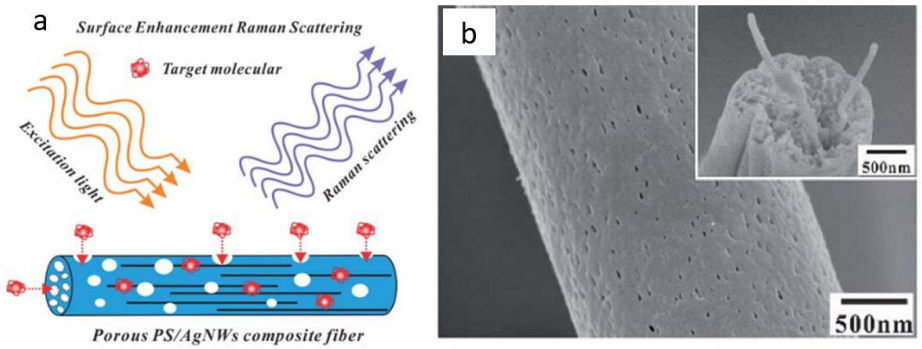

Figure 3.5. Schematic illustration of Ag NWs/PS composite porous fiber used in (Chen 2020). a) target molecules permeating into the surface of Ag NWs from the holes for SERS testing. b) magnified SEM images of the surface and cross-section (inset) of a single composite fiber. Adapted from Ref. [21]

3.1.3. Methodologies to create internally porous electrospun fibers

There are several methods to create porous electrospun fibers such as selective removal of a sacrificial phase, phase separation, solvent/non-solvent mixtures, or co-axial spinning. [22]

Selective Removal

Selective removal is a two-step process in which the post-treatment step is carefully controlled to fully remove the sacrificial phase whilst maintaining the fiber matrix integrity. The sacrificial components can either be salts, silica, or

polymers that can be easily extracted by solvents or removed by other post-treatment methods such as heat treatment or using solvents for the sacrificial phase [23, 24].

Non-solvent-induced phase separation

In non-solvent-induced phase separation (NSIPS), a non-solvent (such as water) is added to the polymer solution. In this process, thermodynamics plays an important role since there is an unstable region, called the demixing gap, where separation in two phases occurs, which result in the formation of porous structure. [25]

Vapor-induced phase separation

In this mechanism, the water, which is a non-solvent vapor, is introduced (dissolved) and mixed inside the fiber (Figure 3.6). Subsequently, the solvent is evaporated, and the phase separation supplies the liquid-liquid demixing due to the concentration of the polymer being thermodynamically unstable and the boiling point of the solvent being higher in comparison with water (slow evaporation of solvent). In this sense, the phase separation carries on a coexistence of polymer-rich and polymer-poor phases [26, 27, 28].

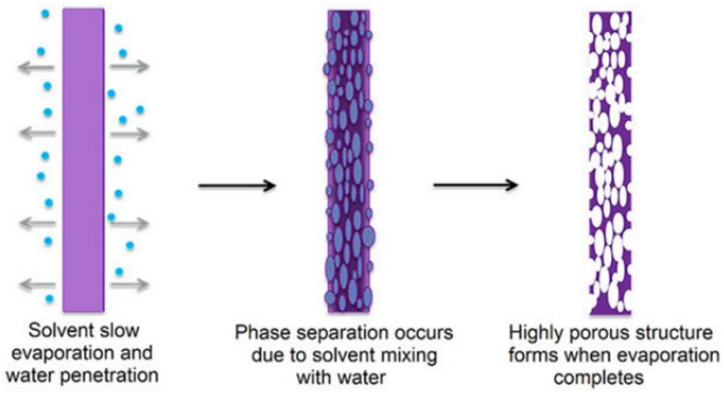

Figure 3.6. Schematic diagram of surface pore formation induced by breath figures mechanism. Adapted from [27].

Thermally-induced phase separation (TIPS)

In the TIPS process, a polymer is dissolved in a high boiling low molecular weight diluent at elevated temperatures and after forming the solution to the desired shape, flat or hollow fiber membrane, it is cooled to induce phase separation. In the final stage of the membrane fabrication, the diluent is extracted by another solvent and then the solvent is removed to produce membrane structure [29].

Co-axial electrospinning

Coaxial electrospinning is a modification of the conventional electrospinning process involving the arrangement of multiple component feed systems simultaneously. One nozzle dispenses the core material, and the other nozzle dispenses the shell material followed by selective removal of the liquid core [30, 31, 32, 33, 34]. This phenomenon leads to obtaining hollow fibers as shown in Figure 3.7.

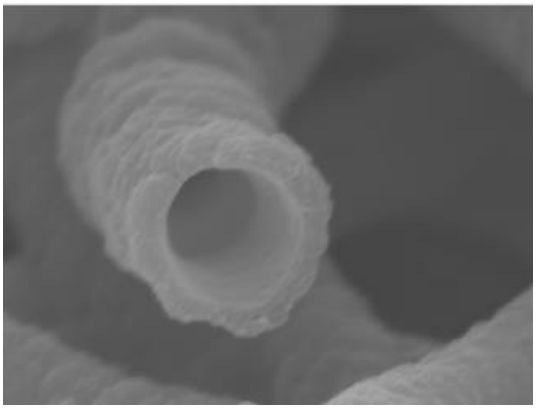

Figure 3.7. Cross-section image of a fiber produced by co-axial electrospinning. Adapted with permission from Ref. [34].

3.1.4. Methodologies to determine the porosity of individual fibers

Image analysis of microtome sliced fibers by TEM

In electrospinning and nanofibers literature, we have found that several attempts have been made to determine the internal porosity of individual fibers numerically. Pai et al reported a technique that is based on Transmission Electron Microscopy (TEM) images of microtome sliced fibers. In their work, they determined the as-spun area and annealed area of polystyrene fibers by using those TEM images (Figure 3.8) [35].

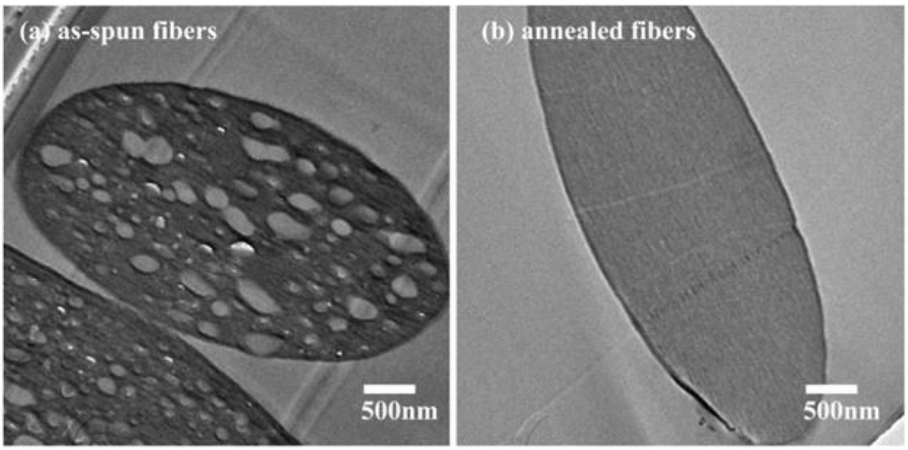

Figure 3.8. Images of microtome sliced fibers. a) as-spun b) annealed fiber. Adapted from Ref. [35].

To do this analysis, the polystyrene fibers were embedded in resin then cut into 60 nm slices by using a microtome. They used two different methods to investigate the internal porosity of polystyrene fibers. *In the first method*, the void volume fraction, was evaluated as $1 - (d_{anneal}^2/d_{as\text{-}spun}^2)$, where $d_{as\text{-}spun}$ is the average diameter of the as-spun fibers and d_{anneal} is the average diameter of the fibers after annealing. *In the second method* for determining void volume fraction, the void fraction was computed based on the shrinkage of the fiber diameter after annealing. Image processing tools were used to set the threshold that distinguishes an image into objects of interest and background based on gray level for the cross-sectional TEM image, and then the area of voids within the fiber can be analyzed. They determine the diameter for each void and the total void volume fraction within the fiber by performing area fraction measurements and comparing the total cross section of voids to that of the fiber.

Similarly, Li et al. determined the surface porosity of polylactic acid fibers using Field Emission Scanning Electron Microscopy (FESEM). They quantified the pores on the surfaces on the fiber by ImageJ, in the end, they determined the surface porosity with the formula surface porosity (%) =sum of pore area/whole fiber area x 100. They tried to correlate the surface porosity of the fiber to its mechanical properties. However, their conclusion was, the mechanical properties do not depend only on surface porosity but also internal porosity [36]. Their conclusion also shows that a robust method to characterize the porosity of individual fibers is needed.

Paraffin Method

Fashandi and Karimi reported another technique to quantify the fractional pore volume (FPV) of electrospun fibers, which we can also call internal porosity. They immersed a large collection of fiber in paraffin, knowing the mass and volume of fibers and paraffin, and they determined the density of fibers. And since the density of material was also known, it was possible to determine the internal porosity [37]. In their study, colorless liquid paraffin was used to calculate the mass density of electrospun fibers. Liquid paraffin was chosen as a matrix due to its non-polar and hydrophobic nature, two essential factors for the complete wetting of polystyrene fibers. In addition, large paraffin molecules are not susceptible to diffuse in the interior porous structure of fibers. The fibers were mixed with liquid paraffin in a glassy vessel of a given volume to form an integrated composite. Knowing the total volume of composite corresponding to the volume of vessel, weight fraction of electrospun fibers (ω_f), and matrix, i.e. paraffin (ω_p), allows one to calculate the density of produced fibers. ρ_f is the density of the fibers and ρ_p is the density of paraffin.

$$\frac{1}{\rho_{mix}} = \frac{\omega_f}{\rho_f} + \frac{\omega_p}{\rho_p}$$

Density of produced fibers can be used to calculate the internal porosity when the compact fiber density is known.

3.2. New method of individual fiber porosity determination based on microscopy techniques (This Work)

In this work, we propose a different method from aforementioned studies, where we combine SEM and AFM techniques. We compute the void fraction (individual fiber porosity) by investigating the fiber cross-sectional area before and after thermal annealing. As-spun fiber area (before annealing) is determined from SEM images and the annealed fiber area is determined by AFM. The idea of this method is based on collecting a single fiber on a silicon wafer and breaking the silicon wafer into two halves. The purpose of breaking the substrate into two halves is to investigate the *same* fiber before and after collapsing the pores by annealing. A simple illustration of the whole process is shown in Figure 3.9. We have chosen both rubbery polymer and glassy polymers to study their porosity. As a rubbery polymer, we chose polycaprolactone (PCL) since it is widely used in tissue engineering, but also, we also studied polystyrene (PS) fibers due to their wide use in electrospinning in general [38, 39, 40, 41, 42, 43].

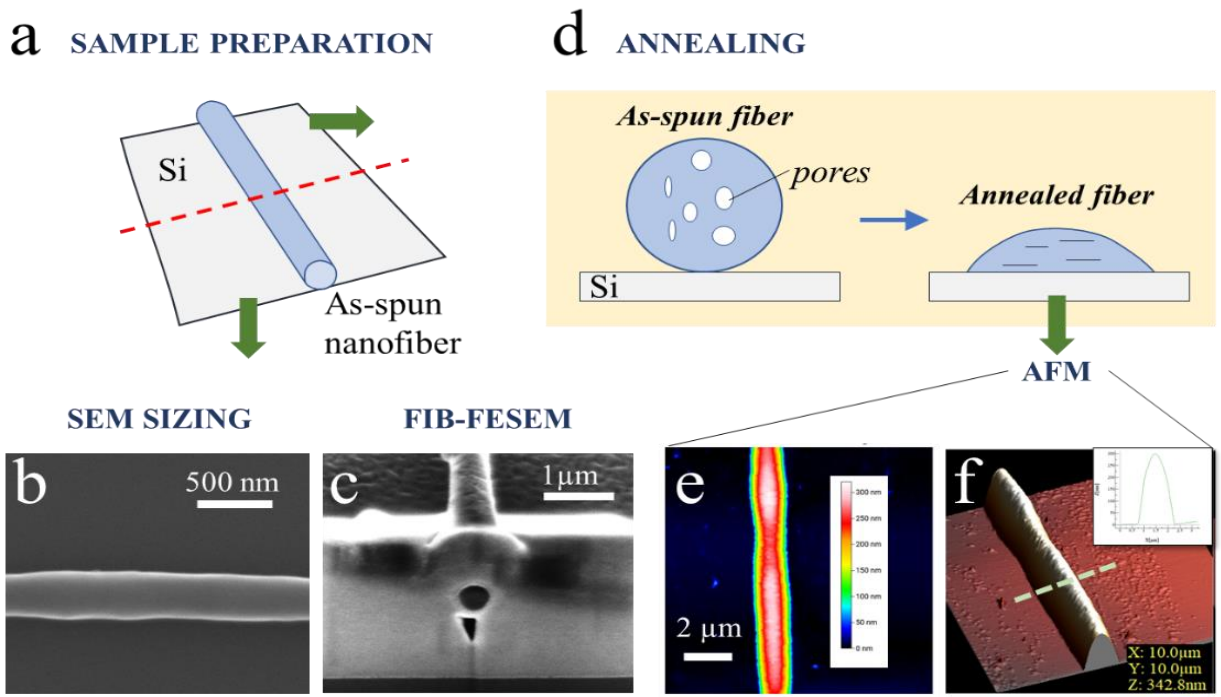

Figure 3.9. Porosity determination by microscopy techniques (This work)

3.3. Results

3.2.1. Porosity determination of polycaprolactone (PCL) fibers

PCL was dissolved in chloroform/methanol (3:1 by volume) and deposited onto a rotating wire drum. (Figure 3.10) The reason why we chose these solvents and collector types is that we wanted to determine the porosity of a specific type of polycaprolactone fibers that are used in Chapter 4 and analyzed mechanically. Therefore, we aimed to reproduce the same experiments. (See Chapter 4 for details) However, it is well known that rotating drums cause an orientation in the polymer chains and change the degree of crystallinity, consequently causing a change in density [44]. Therefore, we did not use this kind of collector type for polystyrene (explained in section 3.5.2). We investigated the crystallization of PCL polymer produced with a rotating wire drum in case it makes a difference in density and, consequently, in porosity computation.

The individual fiber porosity (Φ) is the volume fraction inside the fiber which is occupied by nanovoids and was computed as $\Phi=1-A_{annealed}/A_{as\text{-}spun}$, where $A_{as\text{-}spun}$ is the cross-sectional area of the (circular) electrospun fiber, and $A_{annealed}$ is the area of the (non-circular) fiber after its voids have been thermally collapsed. For this purpose, new samples were prepared by electrospinning only for ~5 s, to get a light fiber collection on the wire drum to obtain isolated fibers easily. It was done under 45-55% RH and at room temperature. After collection, a single fiber was placed on a Si substrate directly from the wire drum by approaching the fibers from behind and picking them individually. The sample was then split into two halves. One half was imaged by SEM and the fiber's width (D_k) was determined at K locations in N images of the same fiber, and used to compute the fiber's average as-spun cross-sectional area $A_{as\text{-}spun}$ as:

$$A_{as-spun} = \frac{1}{N}\sum_{n}^{N}\left(\frac{1}{K}\sum_{k=1}^{K}\frac{\pi D^2}{4}\right)$$

which expresses the averaging of areas ($S_n = \frac{1}{K}\sum_{k=1}^{K}\frac{\pi D^2}{4}$). The fiber width D_k is interpreted as a diameter because the fibers on the Si wafers were circular, as we verified by FIB-FESEM (Figure 3.12). The other half of the Si substrate was annealed and inspected under AFM. Annealing was done to collapse any internal nanovoids possibly present within the fiber by heating on a hot plate above the melting point of the polymer (for 15 minutes at ~70º C), then taken to a Petri dish immediately to cool it down quickly, to minimize the formation of crystalline regions during cooling. Occasionally, the AFM images of annealed fibers revealed texture, which might be due to nanometric crystalline regions embedded in the amorphous matrix. The average annealed fiber area, $A_{annealed}$, was computed by dividing the fiber volume v by its length l.

The process of annealing did not change the fiber length (l) because while the fiber was molten, no corrugations developed along the fiber by the Rayleigh-Plateau instability [45]. Such liquid motions are driven by the surface tension stresses at the fiber/air interface, while viscous and contact stresses slow them down.

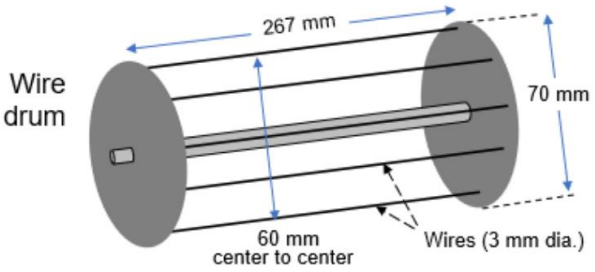

Figure 3.10. Wire drum used in PCL individual fiber porosity determination study.

XRD

First, we investigated the commercial PCL beads we purchased from Sigma Alrich (semicrystalline, which has approximately %50 degree of crystallinity). We run XRD measurements on the beads as received and after annealing in order to see whether annealing has an influence on the crystallinity.

2D diffractograms of aligned fibers were made using a Bruker-AXS D8-Discover diffractometer equipped with a parallel incident beam (Göbel mirror), vertical θ-θ goniometer, XYZ motorized stage, and with a GADDS (General Area Diffraction System). An X-ray collimator system close-to-the-sample allows to analyze areas of 500 μm. The X-ray diffractometer was operated at 40 kV and 40 mA to generate $Cu_{k\alpha}$ radiation. The VÅNTEC-500 GADDS detector was placed at 9 cm from the sample. The exposure time was 1900 s per *frame*. Aligned fibers were glued to a ring-shaped support, which was then placed into the diffractometer to perform the analysis in transmission mode. 1D diffractograms were obtained with a Bruker-AXS D8-Advance diffractometer with vertical theta-theta goniometer, incident- and diffracted-beam Soller slits of 2.5°, a fixed 0.5° receiving slit, and an automatic Air-scattering knife on the sample surface. The angular 2θ range was between 5° and 80°. The data were collected with an angular step of 0.02° at a step/time of 0.5 s. Cuk_{α} radiation was obtained from a copper X-ray tube operated at 40 kV and 40 mA. Diffracted X-rays were detected with a PSD detector LynxEye-XE-T with an opening angle of 2.94°. Aligned fibers were deposited on a low-background support (Si (510)) which was then placed into the diffractometer to perform the analysis in reflection mode.

A sample of aligned fibers was specifically electrospun for the XRD analyses under the same conditions as the mechanical test ones. 2D diffractograms were collected to interpret the molecular orientation in the fibers. Two discrete diffraction arcs in the aligned samples (Figure 3. 11a) showed that the crystal planes in the nanofibers were oriented in a specific direction in the fiber. The azimuthal angles between the centers of both diffraction arcs and the fiber axis were approximately

90°, indicating that the angles between the poles of the (110) and (200) crystal planes and the fiber axis were orthogonal. The diffraction pattern is an arc, not a point, due to the (expected) dispersion in orientation angles of the crystals. 1D Diffractograms were used to investigate the degree of crystallinity, crystal lattice, and crystallite size in the fibers. The fibers displayed (110) and (200) diffraction peaks at 21.6° and 23.9°, respectively (Figure 3.11b). Figure 3.11c represents the lattice and crystallite configuration with respect to the fiber. The crystal structure of PCL is orthorhombic with the following unit cell parameters: a = 7.496 Å, b = 4.974 Å, and c = 17.26 Å. [46] The unit cell contains two monomer units aligned/stretched along the direction of c [47]. Our data confirms the expectation that the molecular chains in the nanocrystalline regions are substantially parallel to the fiber axis. The degree of crystallinity and crystallite size was found 70% and 16.8 nm (Figure 3.11b). This high degree of crystallinity was caused by the stretching experienced by the fibers during the electrospinning and collection processes.

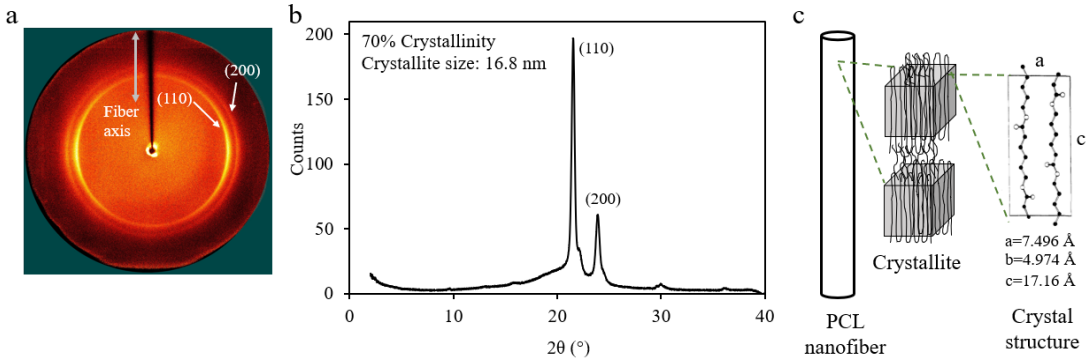

Figure 3.11. a) 2D-XRD pattern of aligned PCL fibers. b) X-ray diffraction pattern of aligned PCL fibers with crystallinity data. c) schematic representation of PCL fiber, crystallites, and lattice cell, showing the predominant relative orientation. (c) is adapted from Ref. [46].

Focused Ion Beam (FIB)

To determine whether the fibers were circular, we sectioned the fibers using a focused ion beam (FIB) FESEM instrument (FEI-Scios 2). A group of fibers was

attached to stainless steel support using silver paste (Figure 3.12a). The fibers were then coated with ~10 nm gold in the microscope, and then with a layer of platinum for stable cross-sectioning (Figure 3.12b). The area of the as-spun fiber was determined with $\pi D^2/4$. However, in order to make sure that the fiber was circular, we took cross-sectional images of the fiber. Please note that it is still possible to apply this method even if the fiber is not circular, but in that case, for the cross-sectional area determination, we would have needed to know what the cross-sectional shape is.

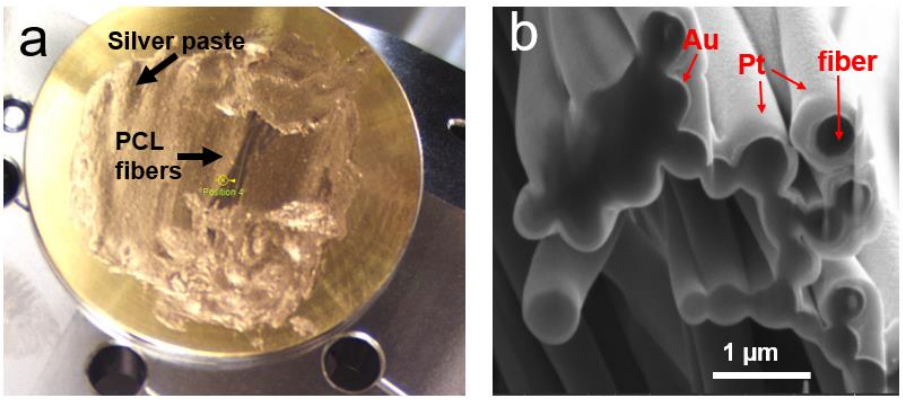

Figure 3.12. a) PCL nanofibers attached to stainless steel support using silver paste b) cross-section of PCL nanofibers

AFM sample, modes, and calibration

For the AFM half of the sample, it was needed to anneal the fibers until the point the pores collapse. It is not desirable to anneal the fibers until they melt and flow. After exceeding a temperature point or annealing it for too long, the fiber goes Rayleigh instability which is not desirable since it makes the average area determination statistically harder. Some Rayleigh instability and melted fiber examples are shown in Figure 3.13a (top view) and Figure 3.13b (3D view) It is critical to find the most appropriate temperature and annealing time for the fibers. In the case of excessive heating (Figure 13c) the fiber melts and flows which also makes the area computation more difficult. Therefore, the fiber should be heated

only until the point where the polymer softens and pores collapse, but not completely melted.

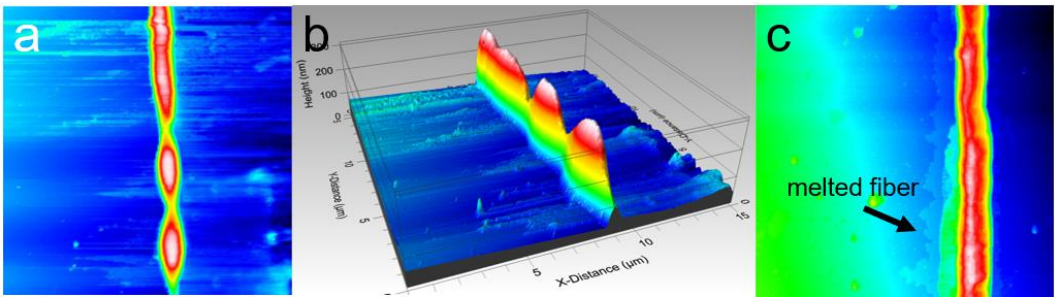

Figure 3.13. a) Rayleigh instability in annealed fiber b) 3D view of the same section. c) Melted fiber due to excessive heating.

AFM modes and calibration should be taken into consideration. The AFM tip we used in our measurements is shown in Figure 3.14. Due to the morphology of the AFM tip, it is expected that the tip would create artifacts with sharp shapes as shown in the calibration samples. However, this artifact is not expected when we have smooth objects like annealed fibers.

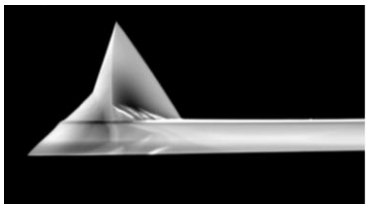

Figure 3.14. BudgetSensors Multi 75-G probe (10 nm radius, 17 µm height, 20°-25° along cantilever axis, 25°-30° from side, 10° at the apex).

We used two types of AFM calibration samples (pillars and squared holes) to ensure that the measurement was accurate. To analyze the AFM topography images we used the software Profilmonline (http://profilmonline.com) (accessed between March and December 2020). (Figure 3. 15) Please take note that these AFM scans belong to the same individual fiber, albeit captured at various locations.

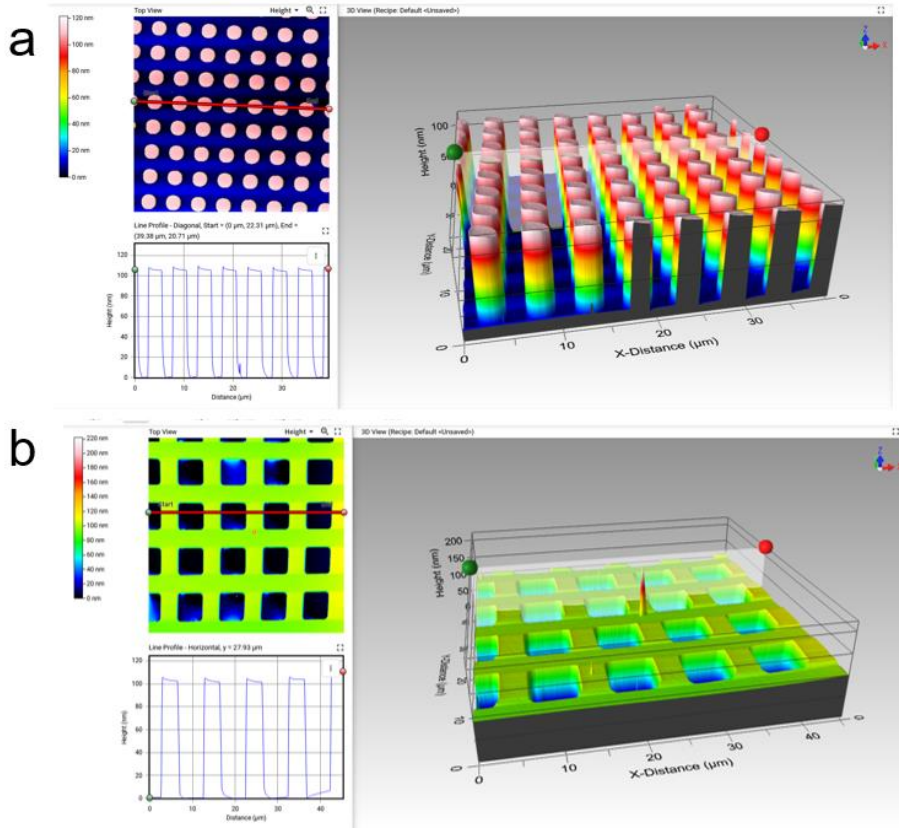

Figure 3.15. AFM calibration samples. a) cylindrical pillars. b) square holes.

Computation of the annealed PCL nanofiber area

The annealed fibers were scanned at different locations in an Agilent 5050 atomic force microscope using tapping mode with a BudgetSensors Multi 75-G probe (Figure 3.16).

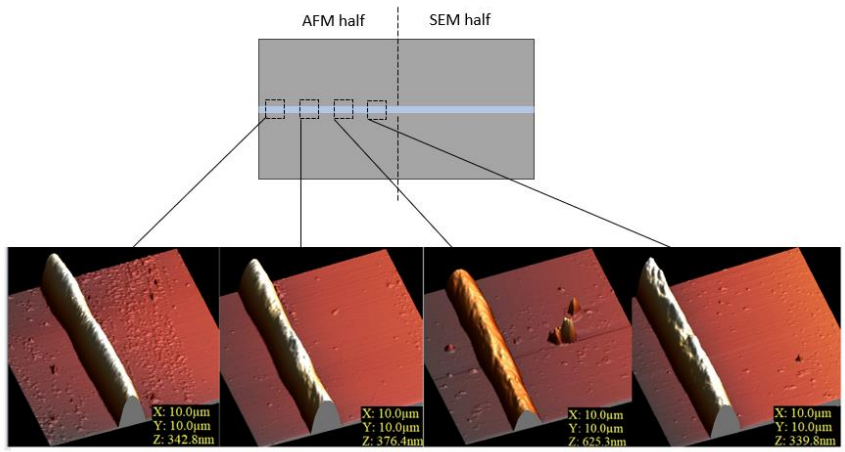

Figure 3.16. An example of fiber sections scans from the same individual fiber.

The AFM images were converted to gwy format using Gwyddion software (version 2.55), and the annealed fiber volume computation was done by Profilmonline and Matlab (R2020a) for a given fiber length. (Figure 3.17)

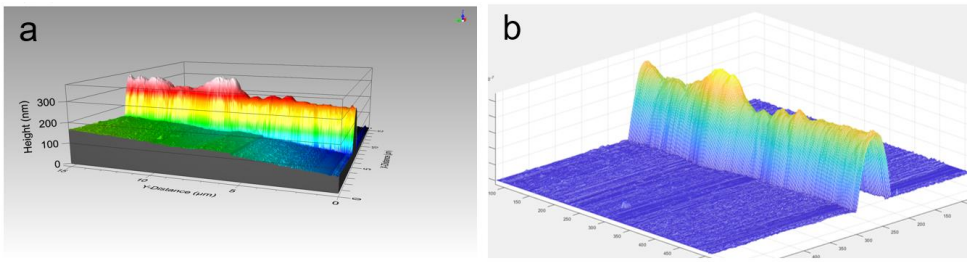

Figure 3.17. Example of a PCL nanofiber AFM data plotted by a) Profilmonline (without background subtraction) and MATLAB.

Table 3.1 shows an example of how the computation of annealed fiber was done. Both Matlab and Profilmonline results were considered (Figure 3.17). The MATLAB result was used to verify the Profilmonline result, and the final computation was done using the Profilmonline result since we performed a more successful background subtraction in Profilmonline most of the time (Figure 3.18).

However, if the background subtraction was not successful in Profilmonline, in that case, we used the MATLAB result.

Table 3.1. Measurement examples from the methodology followed for annealed fiber area computation. They represent the volume and area of the sections from one single fiber.

#fiber section	V(Profilm)	V(MatLab)	Length (µm)	Area (µm^2)
1	**2.704**	**2.559**	10	0.256
2	**2.853**	**2.940**	10	0.294
3	**2.819**	**2.727**	10	0.273
4	**2.836**	**2.769**	10	0.277

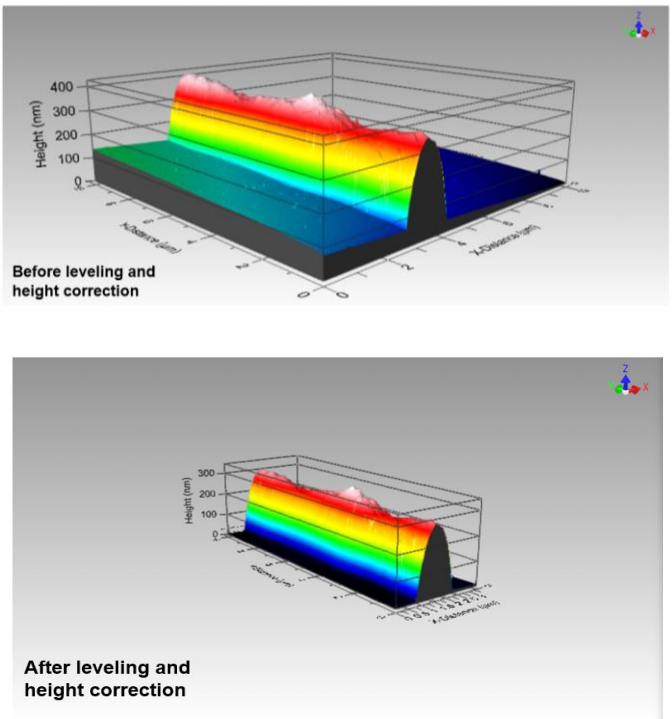

Figure 3.18. Example of a PCL nanofiber before and after subtracting the background. Before leveling and height correction and after leveling and height correction.

Scanning Electron Microscopy (SEM)

The half of the silicon wafer (where the individual fiber stands) was gold coated with a layer thickness of ~43 nm prior to imaging. Micrographs of the fibers were obtained with a JEOL JSM 6400 to obtain the diameter of the fibers collected for the purpose of determining individual fiber porosity. To prevent the stretching of these fibers during this operation, we cut them carefully around the silicon wafer. A precise determination of fiber width was obtained from single-fiber SEM images, which were post-processed with ImageJ's Ridge Detection plugin (http://fiji.sc/Ridge_Detection) [48], whereby a backbone ("skeleton") of the fiber was obtained on the binary image, and the fiber width was then automatically determined at discrete equidistant locations along the entire length of the backbone (Figure 3.19). The average width of the as-spun fiber was determined from several images which were taken from the same fiber and the average area of the fiber $A_{as\text{-}spun}$ was computed.

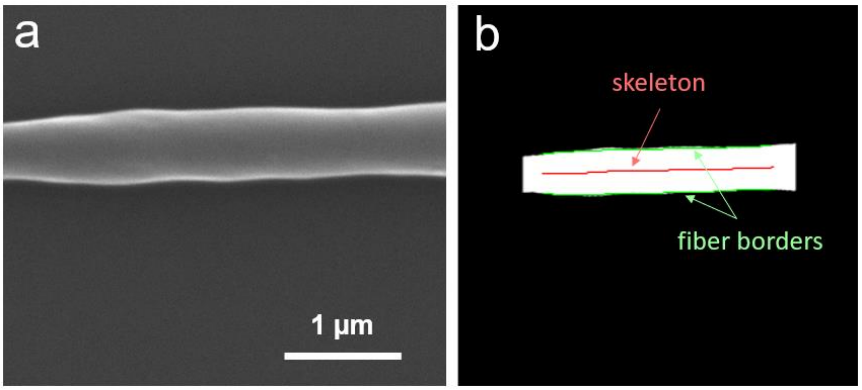

Figure 3.19. a) SEM image of an individual PCL fiber b) skeleton obtained by ridge detection tool on ImageJ.

Table 3.2. Example of results from ridge detection tool for *only one SEM image*. Computed area was averaged for all the SEM images in order to determine $A_{as\text{-}spun}$

# of the pixel measured for the same image	Diameter (μm) measured by Ridge Detection Tool (d)	Area (μm^2) computed ($\pi d^2/4$)
1	0.467	0.171
2	0.483	0.183
3	0.495	0.192
4	0.501	0.197
5	0.504	0.200
6	0.506	0.201
7	0.507	0.202
8	0.508	0.202
9	0.508	0.202
10	0.508	0.202
11	0.507	0.202
12	0.507	0.202
13	0.507	0.202
14	0.507	0.202
15	0.507	0.202
16	0.507	0.202
17	0.507	0.202
18	0.507	0.202
19	0.507	0.202
20	0.507	0.202
21	0.507	0.202
22	0.507	0.202
⋮	⋮	⋮
142	0.460	0.166
143	0.444	0.155
144	0.410	0.132

The overall IFP results of PCL are shown in Figure 3.20. There are two lines indicating the compact fibers where the porosity would be zero ($\Phi=0$). The red line represents the scenario where the as-spun and annealed fibers have the same density whereas the dark blue line represents the case where the annealed fiber has a lower density due to the change in crystallinity, caused by the rotating drum. Each data point corresponds to the average of many data points taken within the same experiment. The result indicates that the data falls around the compact line indicating that our PCL fibers are compact. Only one of them falls above the lines, meaning minus porosity. Since minus porosity is impossible, we assume that the fiber was not uniform along the length and the non-uniformity in diameter affected the $A_{as\text{-}pun}$ calculations.

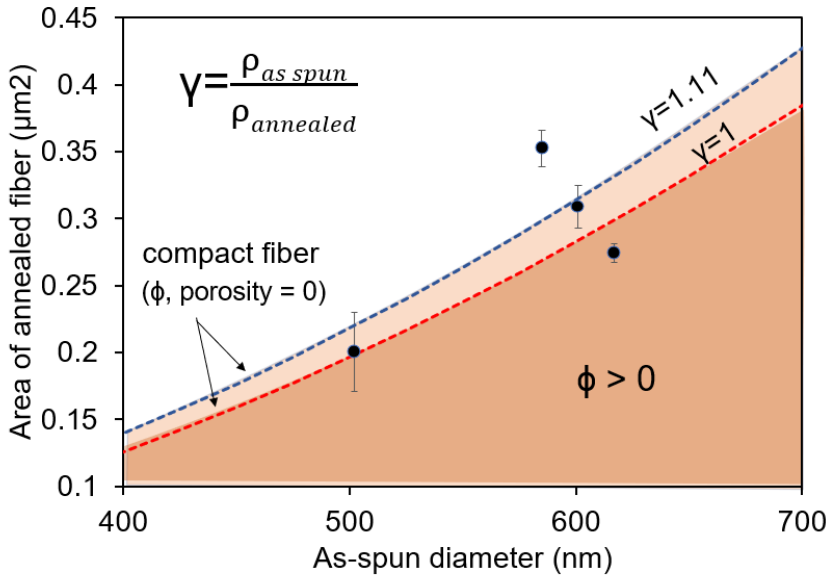

Figure 3.20. Porosity computation and results: annealed area versus SEM fiber diameter and theoretical compact fiber limit.

3.3.2. Porosity determination of polystyrene (PS) fibers

PS was dissolved in DMF and deposited onto a stationary collector with a window where we could collect the fibers until the electrospinning reached a steady state in a different place, then we opened the window and collected the stabilized fibers on the other side of the collector.

The interplay between the PS polymer and the DMF solvent is critical in determining the pore formation mechanism. The phase separation process, driven by the differential solubility of PS in DMF as the solvent evaporates, leads to the creation of pores within the fiber structure. The specific pore size, distribution, and properties can be controlled by adjusting parameters such as polymer concentration, solvent composition, electric field strength, and collector distance.

In the case of polystyrene (PS) and dimethylformamide (DMF), the phase diagram (Figure 3.21) would help in understanding how the polymer dissolves in the solvent at different concentrations and temperatures. This knowledge is crucial for processes like electrospinning, where the polymer solution undergoes phase

separation during fiber formation, leading to the creation of pores within the fiber structure.

Keep in mind that the actual phase behavior can be more complex than this simplified explanation, and the phase diagram can vary based on the specific characteristics of the polymer-solvent system. Detailed experimental studies and thermodynamic analysis are often required to accurately determine the phase diagram and the conditions under which phase separation and pore formation occur in PS fibers.

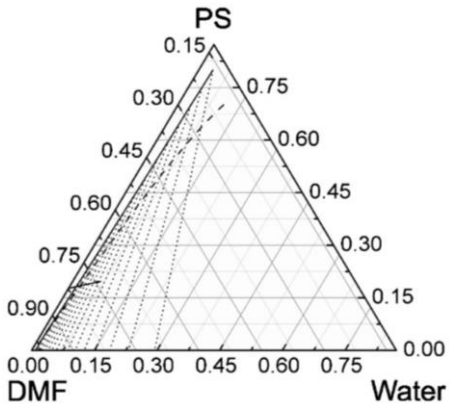

Figure 3.21. Phase diagram of PS/DMF/Water system at 40 ◦C. Solid line is the binodal curve, dashed line indicates the spinodal curve, and dotted line is the tie lines. Adapted with permission from Ref [37].

We prepared 25 wt.% PS in DMF solvent. The solution was left overnight on the stirring plate at moderate speed. The electrospinning was done without co-axial gas flow and at high relative humidity. Since DMF is a non-volatile solvent, it was possible to run electrospinning without any blockage on the needle. When the experiments were done at low relative humidity bead formation was observed. This behavior can be explained by polymer precipitation on the fiber skin. Water molecules act like a "non-solvent" and cause the polymer precipitation on the fiber shell.

Microscopy method for polystyrene individual fiber porosity determination

We used a half-covered collector for this experiment, as shown in Figure 3.22. During the first minutes of electrospinning, we let the fibers be collected on the open half of the collector, which we call *"transient collection"*. During transient collection, the electrospinning is not steady. After reaching a steady state, we opened the other half of the collector and ran the experiment for about 5 more seconds.

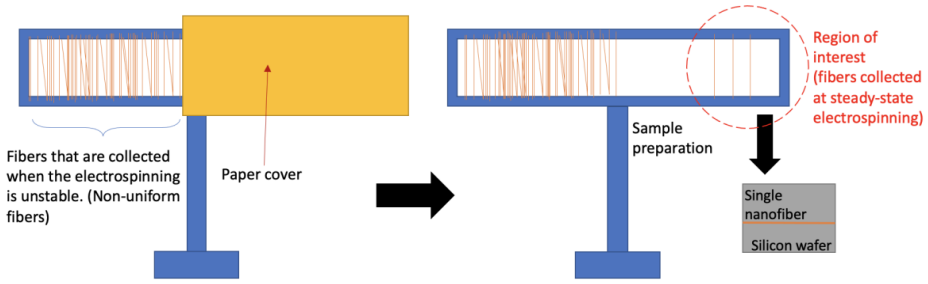

Figure 3.22. The process of single fiber collection.

For the microscopy method, the method was applied to one single fiber assuming the uniformity of the fiber size based on the steadiness of the electrospinning and the standard deviation of the fiber's diameters determined by SEM. The individual PS fiber was collected using a silicon wafer and cut into two halves. The purpose of cutting the single fiber into two halves is to subject one of the halves to heat in order to collapse its interior pores, as illustrated in Figure 3.23. The other half of the fiber (the as-spun fiber) was gold coated for 90 s in a gold-coater by applying a current of 30 mA. The as-spun fiber was then imaged by SEM (JSM- 6400 scanning electron microscope, JEOL Ltd., Tokyo, Japan) for diameter measurement using ImageJ software. Four to five images were uniformly obtained from the as-spun fiber for the average diameter measurement. The second half (the annealed fiber) was heated under 150 °C for 40 minutes. The length and volume of annealed fibers were obtained from AFM with contact mode. As-spun fiber's SEM images were treated using ImageJ, as seen in Figure 3.24a. The annealed part was imaged in the same way using AFM. Figure 3.24b shows the AFM image of the annealed fiber. Then the annealed fiber images were analyzed in Profilmonline. From the volumes and lengths, the annealed fiber's average

cross-sectional area is determined. The provided areas were used for internal porosity computation.

Using the equation $\Phi=1-A_{annealed}/A_{as\text{-}spun}$, the individual fiber porosity was computed.

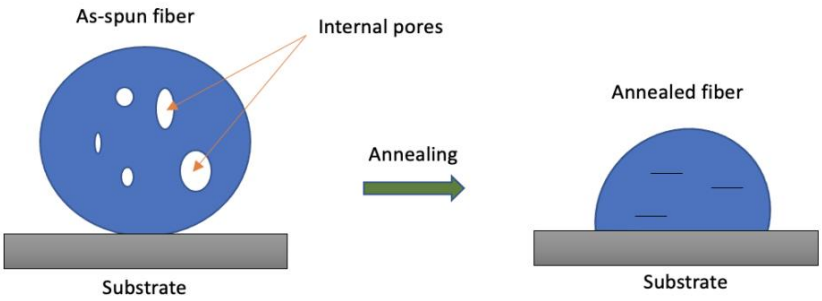

Figure 3.23. Pore collapsing mechanism.

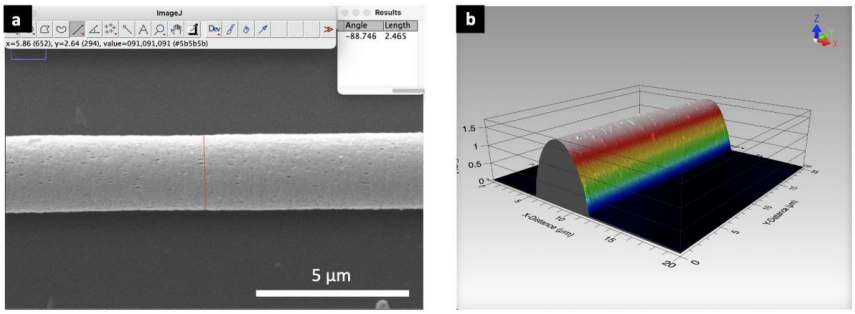

Figure 3.24. a) Diameter determination of individual PS fiber b) Area determination of annealed fiber

Pycnometry method for polystyrene individual fiber porosity determination

The fibers were collected from the aluminum foil by using a stationary collector. (Figure 2.4) The density of PS fibers was obtained using 1 mL (Unadjusted 1mL ACC DIN 12 - WITG3.900.001 and 5 mL (Borosilicate glass 3.3. DIN ISO 3507, type GayLussac) pycnometers. The density was computed by mixing highly liquid paraffin and PS fibers inside the pycnometer to form a homogenous mixture. Highly liquid paraffin was used due to its non-polar and hydrophobic properties, as its large molecules cannot penetrate inside the interior pores of the fibers. Using

the weight of each element in the mixture (pycnometer, fiber, paraffin), the fiber's volume was calculated. As a result, the fiber's density was defined as given by:

$$\rho_{fibers} = \frac{m_{fibers}}{V_{fibers}}$$

Where (ρ, m, V) represent density, mass, and volume, respectively. Individual fiber porosity was computed using fibers and PS densities, as shown in the equation:

$$\phi = 1 - \frac{\rho_{fibers}}{\rho_{polystyrene}}$$

Porosity results obtained by pycnometry method

5 mL pycnometers were used for the electrospun PS fibers (Figure 3.25). The use of two pycnometers allows the comparison of the computed porosity values and establishes a range. 25 mL, 20 mL, and 10 mL pycnometers were used as well at the beginning of the study. The use of bigger flasks resulted in nanofibers with masses in milligrams, while the paraffin's masses were in grams. This big difference provides misguided porosity values, as small errors in mass measurement could impact the porosity computation. Another important point is that small air bubbles can get stuck between the fibers. This means a small volume of air is occupied instead of paraffin and counted as air inside the fibers, which could remarkably affect the determination of individual fiber porosity. To help reduce the bubbles inside the pycnometer, the mixture was gently stirred using a small spatula without damaging the nanofibers.

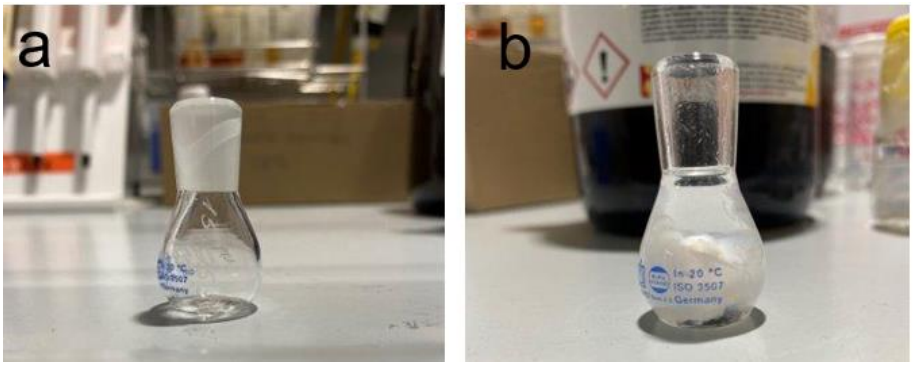

Figure 3.25. a)Pycnometry used in porosity determination experiments. b) Pyconometry filled with PS fibers paraffin.

Although this step was performed skillfully, it appeared that it did not eliminate the bubbles completely, as will be discussed later. As seen in Table 3.3, starting from experiment 4, experiments were run using 1 mL and 5 mL pycnometers. Both pycnometers provide similar porosity values. We conclude that the pycnometer volume (between 1 and 5 mL) is not affecting the result strongly and that the results can be consistent over a wide range of porosity values (although in one case the discrepancy was more than desirable).

As a result, we compared the IFP results obtained by microscopy and pycnometry methods. Although in one case (Experiment 6) the values are very different. We usually obtained similar values for similar fiber diameters. The reason for this discrepancy is unknown in the case of Experiment 6, but we assume that it could be due to trapped air between the fibers. Apart from that, we obtained very similar porosity values to Pai et al.'s results for similar fiber diameters [35]. They reported 46-55% porosity for their PS fibers which are about 4 μm. Our values by microscopy methods also fall in this range. It is expected that the porosity percentage will decrease with the decrease in fiber diameter. Consequently, we report lower porosity for smaller-diameter fibers.

Table 3.3. Individual porosity results from microscopy methods and pycnometry method. In all cases, the solution flow rate is 0.25 ml/h and the co-axial gas flow rate is 0.18 (m/s)

Experiment	Voltage (kV)	Relative humidity (%)	Method	Average diamter (μm)	Individual fiber porosity (%)	Remarks
1	13.89	57	Pycnometry	2.91	12.4	5 ml pycnometer
			Microscopy techniques	1.23	16.6	One single fiber
2	13.3	63	Pycnometry	3.12	37.9	5 ml pycnometer
			Microscopy techniques	3.12	48.6	One single fiber
3	8.77	64	Pycnometry	3.76	38.3	5 ml pycnometer
			Microscopy techniques	3.02	54.4	One single fiber
4	10.21	27	Pycnometry	4.1	14.1 and 12.8	5 ml and 1 ml pycnometer respectively
5	8.6	65	Pycnometry	2.71	50.4 and 52.3	5 ml and 1 ml pycnometer respectively
			Microscopy techniques	2.12	59.8	One single fiber
6	9.51	45	Pycnometry	2.46	15.5 and 25.1	5 ml and 1 ml pycnometer respectively
			Microscopy techniques	2.84	48.6 and 49.8	two single fibers
7	8.84	61	Pycnometry	2.6	37.2 and 31.7	5 ml and 1 ml pycnometer respectively
			Microscopy techniques	2.54	54.4 and 53.4	two single fibers

The outcomes of individual porosity experiments are illustrated in Figure 3.26 and Figure 3.27. The majority of data points are situated within the range of average fiber diameters spanning from 2 to 3 μm. This outcome is anticipated given that we generated the fibers employing identical electrospinning parameters. Concerning the microscopic techniques, porosity values tend to cluster around 50%. Notably, certain points display almost overlap. These instances correspond to fibers derived from the same experimental batch, highlighting the method's reliability when applied to uniform fibers.

In a specific case, where the average diameter measures 1.23 μm, the associated porosity registers at 12%. As anticipated, a reduction in diameter leads to a corresponding decrease in porosity. For the fibers from Experiment 1, computed using the pycnometry method, the porosity was determined to be 16%. This finding reinforces the absence of experimental errors in this disparity between calculations.

Conversely, the porosity values obtained through the pycnometry method exhibited greater variability across the chart. This illustrates the challenge of obtaining consistent data using the pycnometry approach, possibly attributed to the existence of air bubbles.

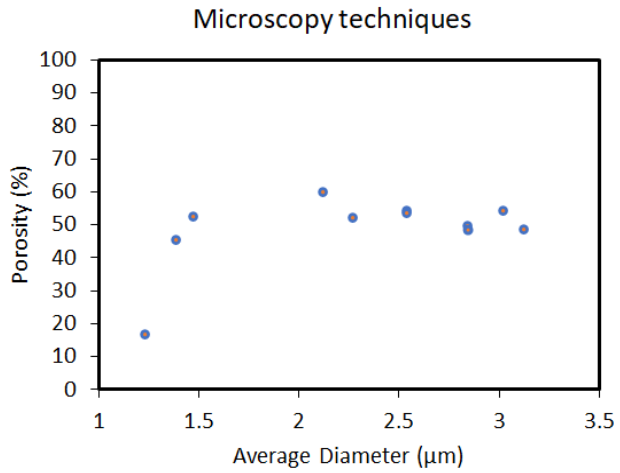

Figure 3.26. Individual fiber porosity vs. Average fiber diameter obtained by microscopy techniques.

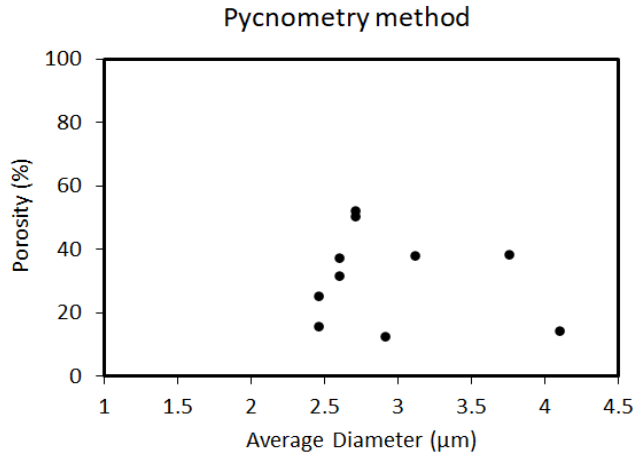

Figure 3.27. Individual fiber porosity vs. Average fiber diameter obtained by pycnometry method.

3.4. Conclusions

In conclusion, this work has introduced a novel technique for accurately computing the internal porosity of individual polymeric nanofibers. Leveraging the capabilities of both SEM and AFM imaging, we have devised a method that enables the determination of cross-sectional areas before and after thermal annealing. This approach offers a localized perspective on fiber porosity, setting it apart from the pycnometry-based method that provides a global porosity value, which also can be valuable in specific applications.

The application of our method to compute the individual fiber porosity of PCL and PS fibers has yielded insightful results. For PCL fibers, the observed compactness or near compactness indicates the absence of internal voids. This information was used in Chapter 4 for determining the tensile modulus. On the other hand, the computed porosity of approximately 50% for PS fibers with sizes ranging from 2 to 3 μm underscores the presence of significant internal voids within these fibers. Such detailed information about fiber porosity has the potential to guide material design and optimization for various applications.

The comparison between our microscopy-based method and the pycnometry-based method revealed the reliability and validity of our approach. By applying these techniques to PS electrospun fibers, we have demonstrated that the microscopy-based approach provides a local view of fiber internal porosity. This localized insight is particularly valuable in understanding the spatial distribution of porosity within individual fibers.

In summary, this study presents a new method as well as it bridges the gap between global and local porosity characterization of nanofibers, offering a powerful analytical tool for in-depth material analysis. The insights gained from this research can steer the development of novel materials with tailored properties, bringing us closer to harnessing the full potential of nanofibers in various cutting-edge applications.

3.5. References

[1] Rengasamy, R. S., Das, D., & Praba Karan, C. (2011). Study of oil sorption behavior of filled and structured fiber assemblies made from polypropylene, kapok and milkweed fibers. *Journal of Hazardous Materials*, *186*(1), 526–532. https://doi.org/10.1016/j.jhazmat.2010.11.031

[2] Jenkins, T. L., & Little, D. (2019). Synthetic scaffolds for musculoskeletal tissue engineering: cellular responses to fiber parameters. *Npj Regenerative Medicine*, *4*(1), 1–14. https://doi.org/10.1038/s41536-019-0076-5

[3] Ramos, C., Lanno, G.-M., Laidmäe, I., Meos, A., Härmas, R., & Kogermann, K. (2020). High humidity electrospinning of porous fibers for tuning the release of drug delivery systems. *International Journal of Polymeric Materials and Polymeric Biomaterials*, 1–13. https://doi.org/10.1080/00914037.2020.1765361

[4] Wang, H., Niu, H., Wang, H., Wang, W., Jin, X., Wang, H., Zhou, H., & Lin, T. (2021). Micro-meso porous structured carbon nanofibers with ultra-high surface area and large supercapacitor electrode capacitance. *Journal of Power Sources*, *482*(August 2020), 228986. https://doi.org/10.1016/j.jpowsour.2020.228986

[5] Fashandi, H., & Ghomi, A. (2015). Interplay of phase separation and physical gelation in morphology evolution within nanoporous fibers electrospun at high humidity atmosphere. *Industrial & Engineering Chemistry Research*, *54*(1), 240–253. https://doi.org/10.1021/ie503848v

[6] Lin, J., Shang, Y., Ding, B., Yang, J., Yu, J., & Al-Deyab, S. S. (2012). Nanoporous polystyrene fibers for oil spill cleanup. *Marine Pollution Bulletin*, *64*(2), 347–352. https://doi.org/10.1016/j.marpolbul.2011.11.002

[7] Bandegi, A., & Moghbeli, M. R. (2018). Effect of solvent quality and humidity on the porous formation and oil absorbency of SAN electrospun nanofibers. *Journal of Applied Polymer Science*, *135*(1). https://doi.org/10.1002/app.45586

[8] Isık, T., & Demir, M. M. (2018). Tailored electrospun fibers from waste polystyrene for high oil adsorption. *Sustainable Materials and Technologies*, *18*, e00084. https://doi.org/https://doi.org/10.1016/j.susmat.2018.e00084

[9] Zaarour, B., Zhu, L., Huang, C., & Jin, X. (2018). Controlling the Secondary Surface Morphology of Electrospun PVDF Nanofibers by Regulating the Solvent and Relative Humidity. *Nanoscale Research Letters*, *13*(1), 285. https://doi.org/10.1186/s11671-018-2705-0

[10] Chen, P.-Y., & Tung, S.-H. (2017). One-Step Electrospinning To Produce Nonsolvent-Induced Macroporous Fibers with Ultrahigh Oil Adsorption Capability. *Macromolecules*, *50*(6), 2528–2534. https://doi.org/10.1021/acs.macromol.6b02696

[11] Hou, H., Wang, L., Gao, F., Wei, G., Zheng, J., Tang, B., & Yang, W. (2014). Hierarchically porous TiO2/SiO2 fibers with enhanced photocatalytic activity. *RSC Advances*, *4*(38), 19939–19944. https://doi.org/10.1039/C4RA02285H

[12] Ning, J., Zhang, X., Yang, H., Xu, Z.-L., & Wei, Y.-M. (2016). Preparation of porous PVDF nanofiber coated with Ag NPs for photocatalysis application. *Fibers and Polymers*, *17*(1), 21–29. https://doi.org/10.1007/s12221-016-5705-7

[13] Moroni, L., Licht, R., de Boer, J., de Wijn, J. R., & van Blitterswijk, C. A. (2006). Fiber diameter and texture of electrospun PEOT/PBT scaffolds influence human mesenchymal stem cell proliferation and morphology, and the release of incorporated compounds. *Biomaterials*, *27*(28), 4911–4922. https://doi.org/10.1016/j.biomaterials.2006.05.027

[14] Liao, S., Nguyen, L. T. H., Ngiam, M., Wang, C., Cheng, Z., Chan, C. K., & Ramakrishna, S. (2014). Biomimetic nanocomposites to control osteogenic differentiation of human mesenchymal stem cells. *Advanced Healthcare Materials*, *3*(5), 737–751. https://doi.org/10.1002/adhm.201300207

[15] Mota, C., Wang, S.-Y., Puppi, D., Gazzarri, M., Migone, C., Chiellini, F., Chen, G.-Q., & Chiellini, E. (2017). Additive manufacturing of poly[(R)-3-hydroxybutyrate-co-(R)-3-hydroxyhexanoate] scaffolds for engineered bone development. *Journal of Tissue Engineering and Regenerative Medicine*, *11*(1), 175–186. https://doi.org/10.1002/term.1897

[16] Nguyen, T. T. T., Ghosh, C., Hwang, S. G., Chanunpanich, N., & Park, J. S. (2012). Porous core/sheath composite nanofibers fabricated by coaxial electrospinning as a potential mat for drug release system. *International Journal of Pharmaceutics*, *439*(1–2), 296–306. https://doi.org/10.1016/j.ijpharm.2012.09.019

[17] Sabetzadeh, N., Gharehaghaji, A. A., & Javanbakht, M. (2018). Porous PAN micro/nanofiber separators for enhanced lithium-ion battery performance. *Solid State Ionics*, *325*, 251–257. https://doi.org/10.1016/j.ssi.2018.08.013

[18] Yan, W., Miao, D., Babar, A. A., Zhao, J., Jia, Y., Ding, B., & Wang, X. (2020). Multi-scaled interconnected inter- and intra-fiber porous janus membranes for enhanced directional moisture transport. *Journal of Colloid and Interface Science*, *565*, 426–435. https://doi.org/https://doi.org/10.1016/j.jcis.2020.01.063

[19] Kim, W., Park, E., & Jeon, S. (2020). Performance Enhancement of a Quartz Tuning Fork Sensor Using a Cellulose Nanocrystal-Reinforced Nanoporous Polymer Fiber. *Sensors*, *20*(2). https://doi.org/10.3390/s20020437

[20] Nathani, A., & Sharma, C. S. (2019). Electrospun Mesoporous Poly(Styrene-Block-Methyl-Methacrylate) Nanofibers as Biosensing Platform: Effect of Fibers Porosity on Sensitivity. *Electroanalysis*, *31*(11), 2138–2144. https://doi.org/10.1002/elan.201800796

[21] Chen, S., Ding, C., Lin, Y., Wu, X., Yuan, W., Meng, X., Su, W., & Zhang, K. Q. (2020). SERS-active substrate assembled by Ag NW-embedded porous polystyrene fibers. *RSC Advances*, *10*(37), 21845–21851. https://doi.org/10.1039/d0ra01454k

[22] Huang, C., & Thomas, N. L. (2019). Fabrication of porous fibers via electrospinning: strategies and applications. *Polymer Reviews*, 1–53. https://doi.org/10.1080/15583724.2019.1688830

[23] Cacciotti, I., Calderone, M., & Bianco, A. (2013). Tailoring the properties of electrospun PHBV mats: Co-solution blending and selective removal of PEO. *European Polymer Journal*, *49*(10), 3210–3222. https://doi.org/10.1016/j.eurpolymj.2013.06.024

[24] Chen, H., Di, J., Wang, N., Dong, H., Wu, J., Zhao, Y., Yu, J., & Jiang, L. (2011). Fabrication of Hierarchically Porous Inorganic Nanofibers by a General Microemulsion Electrospinning Approach. *Small*, *7*(13), 1779–1783. https://doi.org/10.1002/smll.201002376

[25] Gao, J., Huang, X., Wang, L., Zheng, N., Li, W., Xue, H., Li, R. K. Y., & Mai, Y. W. (2017). Super-hydrophobic coatings based on non-solvent induced phase separation during electro-spraying. *Journal of Colloid and Interface Science*, *506*, 603–612. https://doi.org/10.1016/j.jcis.2017.07.089

[26] Jiang, Y., Fang, D., Song, G., Nie, J., Chen, B., & Ma, G. (2013). Fabrication of core-shell nanofibers by single capillary electrospinning combined with vapor induced phase separation. *New Journal of Chemistry*, *37*(9), 2917–2924. https://doi.org/10.1039/c3nj00654a

[27] Huang, C., & Thomas, N. L. (2018). Fabricating porous poly(lactic acid) fibres via electrospinning. *European Polymer Journal*, *99*(September 2017), 464–476. https://doi.org/10.1016/j.eurpolymj.2017.12.025

[28] Cheng, N., Miao, D., Wang, C., Lin, Y., Babar, A. A., Wang, X., Wang, Z., Yu, J., & Ding, B. (2023). Nanosphere-structured hierarchically porous PVDF-HFP fabric for passive daytime radiative cooling via one-step water vapor-induced phase separation. *Chemical Engineering Journal*, *460*(February), 141581. https://doi.org/10.1016/j.cej.2023.141581

[29] Xie, F., Wang, Y., Zhuo, L., Jia, F., Ning, D., & Lu, Z. (2020). Electrospun Wrinkled Porous Polyimide Nanofiber-Based Filter via Thermally Induced Phase Separation for Efficient High-Temperature PMs Capture. *ACS Applied Materials and Interfaces*, *12*(50), 56499–56508. https://doi.org/10.1021/acsami.0c18143

[30] Tian, Y., Wang, Z., & Wang, L. (2021). Hollow fibers: From fabrication to applications. *Chemical Communications*, *57*(73), 9166–9177. https://doi.org/10.1039/d1cc02991f

[31] McCann, J. T., Li, D., & Xia, Y. (2005). Electrospinning of nanofibers with core-sheath, hollow, or porous structures. *Journal of Materials Chemistry*, *15*(7), 735–738. https://doi.org/10.1039/b415094e

[32] Anka, F. H., & Balkus, K. J. (2013). Novel nanofiltration hollow fiber membrane produced via electrospinning. *Industrial and Engineering Chemistry Research*, *52*(9), 3473–3480. https://doi.org/10.1021/ie303173w

[33] Duan, G., & Greiner, A. (2019). Air-Blowing-Assisted Coaxial Electrospinning toward High Productivity of Core/Sheath and Hollow Fibers. *Macromolecular Materials and Engineering*, *304*(5), 2–6. https://doi.org/10.1002/mame.201800669

[34] Bhattarai, D. P., Tiwari, A. P., Maharjan, B., Tumurbaatar, B., Park, C. H., & Kim, C. S. (2019). Sacrificial template-based synthetic approach of polypyrrole hollow fibers for photothermal therapy. *Journal of Colloid and Interface Science*, *534*, 447–458. https://doi.org/10.1016/j.jcis.2018.09.047

[35] Pai, C.-L., Boyce, M. C., & Rutledge, G. C. (2009). Morphology of Porous and Wrinkled Fibers of Polystyrene Electrospun from Dimethylformamide. *Macromolecules*, *42*(6), 2102–2114. https://doi.org/10.1021/ma802529h

[36] Li, Y., Lim, C. T., & Kotaki, M. (2015). Study on structural and mechanical properties of porous PLA nanofibers electrospun by channel-based electrospinning system. *Polymer*, *56*, 572–580. https://doi.org/https://doi.org/10.1016/j.polymer.2014.10.073

[37] Fashandi, H., & Karimi, M. (2012). Pore formation in polystyrene fiber by superimposing temperature and relative humidity of electrospinning atmosphere. *Polymer*, *53*(25), 5832–5849. https://doi.org/https://doi.org/10.1016/j.polymer.2012.10.003

[38] Uyar, T., & Besenbacher, F. (2008). Electrospinning of uniform polystyrene fibers: The effect of solvent conductivity. *Polymer*, *49*(24), 5336–5343. https://doi.org/10.1016/j.polymer.2008.09.025

[39] Kang, M., Jung, R., Kim, H. S., & Jin, H. J. (2008). Preparation of superhydrophobic polystyrene membranes by electrospinning. *Colloids and Surfaces A: Physicochemical and Engineering Aspects*, *313–314*, 411–414. https://doi.org/10.1016/j.colsurfa.2007.04.122

[40] Wang, C., Hsu, C. H., & Lin, J. H. (2006). Scaling laws in electrospinning of polystyrene solutions. *Macromolecules*, *39*(22), 7662–7672. https://doi.org/10.1021/ma060866a

[41] Lin, J., Ding, B., Jianyong, Y., & Hsieh, Y. (2010). Direct fabrication of highly nanoporous polystyrene fibers via electrospinning. *ACS Applied Materials and Interfaces*, *2*(2), 521–528. https://doi.org/10.1021/am900736h

[42] Huan, S., Liu, G., Han, G., Cheng, W., Fu, Z., Wu, Q., & Wang, Q. (2015). Effect of experimental parameters on morphological, mechanical and hydrophobic properties of electrospun polystyrene fibers. *Materials*, *8*(5), 2718–2734. https://doi.org/10.3390/ma8052718

[43]Casper, C. L., Stephens, J. S., Tassi, N. G., Chase, D. B., & Rabolt, J. F. (2004). Controlling surface morphology of electrospun polystyrene fibers: Effect of humidity and molecular weight in the electrospinning process. *Macromolecules*, *37*(2), 573–578. https://doi.org/10.1021/ma0351975

[44] Zussman, E., Burman, M., Yarin, A. L., Khalfin, R., & Cohen, Y. (2006). Tensile deformation of electrospun nylon-6,6 nanofibers. *Journal of Polymer Science Part B: Polymer Physics*, *44*(10), 1482–1489. https://doi.org/10.1002/polb.20803

[45] Stachewicz, U., Dijksman, J. F., Soudani, C., Tunnicliffe, L. B., Busfield, J. J. C., & Barber, A. H. (2017). Surface free energy analysis of electrospun fibers based on Rayleigh-Plateau/Weber instabilities. *European Polymer Journal*, *91*, 368–375. https://doi.org/10.1016/j.eurpolymj.2017.04.017

[46] Hu, H., & Dorset, D. L. (1990). *Crystal Structure of Poly (€ -caprolactone)*. 4604–4607.

[47] Bittiger, H., Marchessault, R. H., & Niegisch, W. D. (1970). Crystal structure of poly-ε-caprolactone. *Acta Crystallographica Section B*, *26*(12), 1923–1927. https://doi.org/https://doi.org/10.1107/S0567740870005198

[48] Steger, G. (1998). An unbiased detector of curvilinear structures. *IEEE Transactions on Pattern Analysis and Machine Intelligence*, *20*(2), 113–125. https://doi.org/10.1109/34.659930

Chapter 4. Mechanical characterization of single nanofibers

4.1. Introduction

In most applications, the mechanical properties of the nanofibrous constructs determine their performance and durability. For example, cells in in-vitro models can "feel" the stiffness of the surrounding fibrous matrix or substrate. [1, 2, 3]. In Figure 4.1, we can see the different responses of the cells to different stiffness. In (a) the cell matrix is elongated whereas in (b) cell appears rounded and lacks pronounced stress fiber.

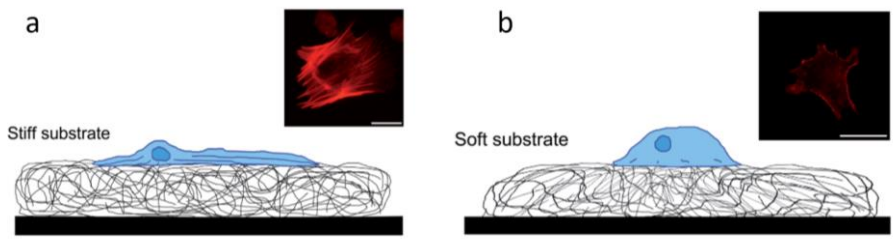

Figure 4.1. Different cell response to materials with different stiffness. a) cell response to a stiff substrate. b) cell response to a soft substrate. Adapted with permission from [2].

The mechanical properties of nanofibrous constructs depend critically on the mechanical properties (e.g., tensile properties) of individual nanofibers, as highlighted in constitutive models, which connect microstructure and macroscopic behavior [4, 5, 6], and in numerical simulations [7, 8, 9]. Therefore, whereas a mechanical test of the nanofibrous construct often suffices in practice, the mechanical characterization of individual nanofibers is critical to develop predictive models and gain fundamental knowledge.

The approaches used to date to determine the tensile properties of single nanofibers fall in two groups: *tensile testers* and *microtools* [4]. With tensile testers, ultra-sensitive load cells must be used to achieve accuracy and consistency [10, 11]. Otherwise, the force signal is noisy, especially for weak polymers of biomedical interest like polycaprolactone (PCL) [12, 13] and PVDF [14].

Furthermore, the issue of signal noise becomes worse as the fiber size gets smaller [15, 16, 17, 18]. With microtools, the fiber is typically pulled or bent by atomic force microscopy (AFM) cantilever tip [19, 20, 21, 22, 23, 24, 25, 26, 27]. Figure 4.2 shows several examples of AFM tools for tensile tests. Wingert et al. tested individual nylon-11 fibers by attaching them to the AFM cantilever via tungsten manipulator (Figure 4.2a) [23]. Zussman et al. followed a similar strategy and attached individual nylon-66 fibers between the AFM cantilever and stainless-steel wire (Figure 4.2c) [25]. Baker et al. used a different strategy that relies on stretching of the individual fibers that are anchored on a purpose-made substrate (Figure 4.2b) [20].

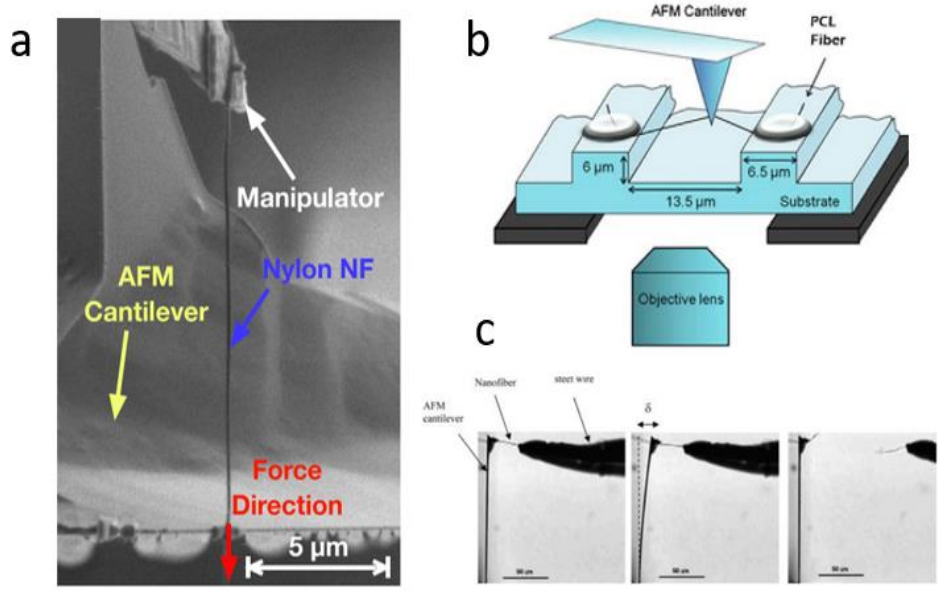

Figure 4.2. Use of AFM tools for single fiber tensile modulus determination. a) Nylon-11 fiber tested by attaching them to the AFM cantilever via tungsten manipulator. Adapted with permission from [23]. b) . The anchored fiber to the grooves of the striated substrate and lateral stretching of the fiber AFM probe. Adapted with permission from [20]. c) Mechanical testing of an individual nylon-66 fiber attached between AFM cantilever and stainless steel wire. Adapted with permission from [25].

A complementary approach was presented by Wang et al. where AFM nanoindentation provides local nano-mechanical information [28]. The tensile modulus has also been determined from the resonant frequency of the fiber on which a small weight hangs (Figure 4.3) [29]. However, these measurements were done on very strong materials such as nylon-66. These methods could be more challenging with weaker or rubbery materials.

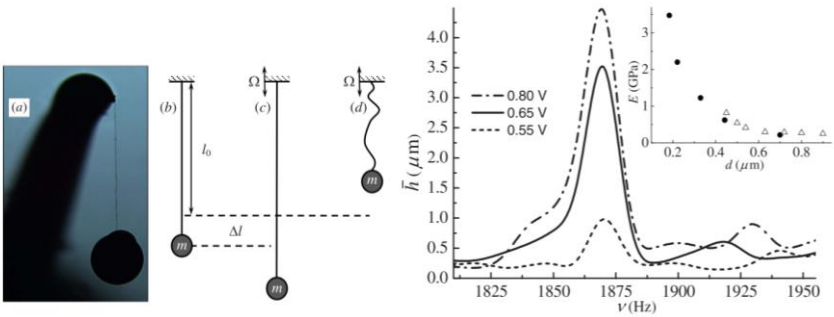

Figure 4.3. Resonant frequency method for single fiber tensile modulus determination. Adapted with permission from [29].

These single-fiber testing methods, however, suffer from several shortcomings. First, isolating individual nanofibers is inherently difficult [30], and this may be why many studies focused on strong polymers like silk, nylon, polyimide, PA(6)3T, PS, Chitosan, Polyimide, and PAN (Table 4.1). Second, the sensitivity of the force-sensing device (e.g. load cell or AFM cantilever) must be ultrahigh to be able to match the tiny tension in the fiber. In a few cases, bundles of aligned nanofibers have been used to mitigate these challenges (Figure 4.4); however, this approach only works if the number of fibers is low enough to be counted (for the cross-

sectional area computation, as explained below), and only a modest gain (~2-10) in force-sensing is achieved [31].

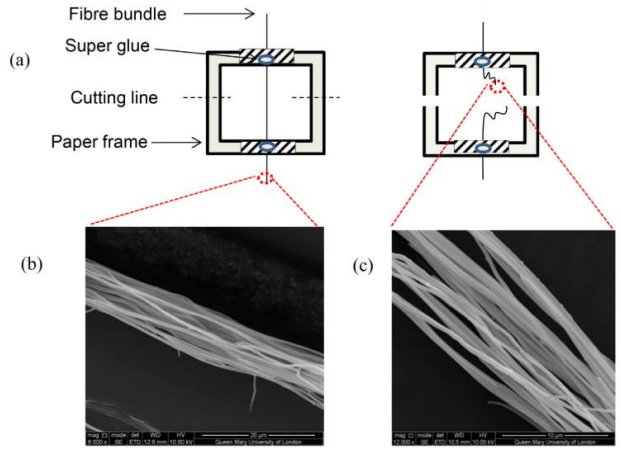

Figure 4.4. Tensile testing of fiber bundles. Adapted with permission from [31].

The third challenge in single-fiber testing is the determination of the initial fiber size before the mechanical test, which usually requires electron microscopy, where the fiber can be damaged by the electron beam. Instead, the size of the fiber has been determined by optical microscopy [32], but this can lead to big errors due to the optical resolution limit at close to 1 μm. Another method commonly used to determine the size of nanofibers was inspecting the undeformed section of the fiber by scanning electron microscopy (SEM) after the mechanical test. [30] However, this method also remains unclear since the unbroken part of the fiber might undergo plastic deformation. Finally, by single-fiber measurements it is difficult to obtain enough measurements (on different fibers) to obtain statistically averaged data which can represent a particular nanofibrous construct. Table 4.1 shows a summary of single fiber mechanical tests in electrospinning literature.

Here, we describe an approach that overcomes these issues. We investigate the individual fiber properties from tensile tests carried on samples of nearly identical electrospun fibers. The fibers are collected in aligned orientation on rotating substrates [33]. To go from the sample data (force versus displacement) to the

individual-fiber information (stress vs. strain) we need the total cross-sectional area of the entire fibers sample. We determine this area by a method that does not involve counting the fibers in the sample, but the mass and internal porosity of the nanofibers. Such individual fiber porosity (IFP) is not usually quantified in electrospinning, despite being critical to the mechanical behavior of the nanofibers and their constructs. [34, 35] Here, to determine the IFP, we use a method which we previously described in Chapter 3 that combines imaging of the fibers by SEM and imaging of thermally annealed fibers by Atomic Force Microscopy (AFM). Figure 4.5 illustrates the electrospinning, sample preparation and tensile testing steps.

We demonstrate this method using poly-ε-caprolactone (PCL), a biodegradable semi-crystalline aliphatic polyester. With a glass transition temperature of -60 °C, and a melting point of about 62 °C [36], it typically behaves as a leathery material and it is delicate, mechanically speaking. The term 'leathery' indicates the behavior observed between the glass transition temperature and the melting temperature for a semicrystalline thermoplastic polymer [37, Chapter 1]. PCL has been widely used in tissue engineering to build scaffolds that promote the regeneration of new tissue, for which the tensile behavior of the nanofiber can be critical during use [38, 39, 40].

Table 4.1. Single fiber studies in literature

Testing Method	First author	year	Reference	Material	M_w (kDa)	Fiber selected from polydisperse mat?	Diameter, average
AFM	Zussman	2006	[25]	Nylon	N/A	No	570 nm and 550 nm
AFM	Wingert	2017	[23]	Nylon	N/A	Yes	65 nm to 516 nm
AFM	Baker	2016	[20]	PCL	120-300	Yes	440 to 1040 nm
AFM	Baker	2012	[19]	Fibrinogen	N/A	Yes	95
AFM	Carlisle	2009	[21]	Fibrin	N/A	Yes	200
AFM	Sharpe	2020	[22]	PCL- Fibrinogen	120-300	Yes	230 +/-90
AFM-3-point	Song	2018	[27]	PVP/mullite	Mn = 130,000	Yes	589 nm
AFM-3-point	Croisier	2012	[24]	PCL	80	Yes	250 to 700 nm
AFM-3-point	Shin	2006	[26]	PAMPS	2000	Yes	60 to 250
AFM nanoindentation	Wang	2004	[28]	silk/PEO	900	Yes	800 +/- 50 nm
Oscillating string	Burman	2008	[29]	Nylon	N/A	Yes	below 500 nm
Tensile Tester	Szewczyk	2020	[63]	PVDF	275	N/A	N/A
Tensile Tester	Tan	2005	[12]	PCL	80	Yes	1.4(+/- 0.3) µm
Tensile Tester	Chew	2006	[18]	PCL	60	Yes	from 200 nm to 5µm
Tensile Tester	Lim	2008	[13]	PCL	80	Yes	from 200 to 1200 nm
Tensile Tester	Wong	2008	[11]	PCL	80	Yes	250 nm to 2.5 µm
Tensile Tester	Pai	2011	[16]	PA(6)3T	N/A	No	from 170 to 3643 nm
Tensile Tester	Silberstein	2012	[6]	PA(6)3T	N/A	N/A	1.2 µm
Tensile Tester	Pai	2009	[34]	Polystyrene	280 and 2000	N/A	1.17 to 3.93 µm
Tensile Tester	Bazbouz	2010	[30]	Nylon 6	N/A	N/A	800 nm
Tensile Tester	Chen	2009	[64]	Collagen-Chitosan	80-100	Yes	between 950 nm 11 µm
Tensile Tester	Chen	2008	[15]	Polyamic acid/Polyimide	270	Yes	221 to 289 nm
Tensile Tester	Papkov	2013	[17]	PAN	N/A	No	262 to 1280 nm

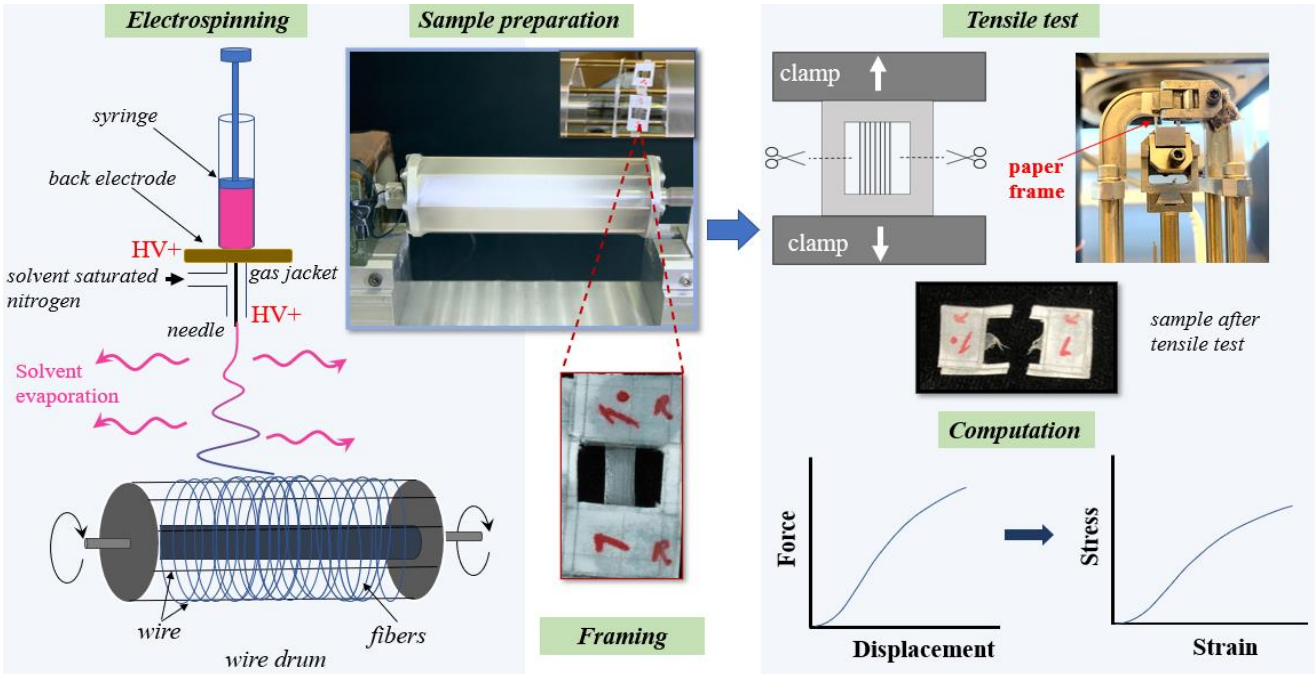

Figure 4.5. Schematic showing the electrospinning, sample preparation and tensile testing steps.

4.2. Experimental Methods

Polycaprolactone (PCL) (Mw 80 kDa; Mw/Mn < 2; ~3 mm pellets; <0.5% water; density 1.145 g/mL at 25 °C) was purchased from Sigma-Aldrich (P/N 440744). Chloroform (≥99%, Alfa Aesar) and methanol (reagent grade, Scharlau) were used as solvents for PCL. A 12% (w/v) PCL solution in chloroform and methanol (3:1 by volume) was prepared under slow stirring on a magnetic stir plate at room temperature. The solution was prepared by first dissolving PCL pellets in chloroform and, after overnight stirring, methanol was added, and the mixture was stirred for two additional hours to obtain a homogeneous and clear solution. PCL solutions based on methanol-chloroform mixtures have been previously electrospun [41, 42, 43, 44].

4.2.1 Electrospinning with a coaxial gas jacket

Electrospinning was performed in a sealed chamber (50 x 50 x 45 cm; see Figure 2.7). A 1 mL glass syringe (Hamilton 81320) was filled with the liquid solution and placed horizontally on an infusion syringe pump (New Era Pump System Ink, NE-300) which was adjacent to the chamber. A syringe needle (0.390 mm ID; 0.685 mm OD) (Figure 4.6) was attached to the syringe and introduced through a hole on a chamber side wall and was then coaxially fitted inside the chamber with a glass tube (7.9 mm ID).

Figure 4.6. The needle used in our experiments. The scale bar is 0.5 mm.

This tube supplied chloroform-saturated nitrogen gas coaxially (as a gas jacket) at 0.35 mL/s to the end of the needle to prevent premature drying by solvent evaporation during electrospinning [45, 46] (following the vial design of Lübbert & Peukert [47]. This flow had a plug-flow speed of 7.2 mm/s, which was intentionally kept far below the fiber speed. (In preliminary tests, we realized that methanol in this coflow was detrimental. As chloroform evaporates faster than methanol, only this solvent's vapor was needed in the gas jacket.) The needle end protruded ~30 mm from a small hole at the center of a 50 mm OD brass disk ("back electrode"), situated behind the glass tube end (Figure 2.7). This configuration helped reduce the amplitude of fiber whipping during electrospinning [33]. The needle and the back electrode were connected to the same high voltage power supply (Ultravolt HV-RACK-2-250-00228). A rotating wire drum collector was centered in the chamber 15 cm away from the needle [48]. The collector consists of eight thin brass rods ("wires") distributed along a 30 mm radius and straddled between two aluminum discs separated by 27 cm (Figure 2.7). This configuration was chosen instead of the commonly used solid cylinder collector to facilitate harvesting the fibers without damage. The wire drum was rotated at 1966 rpm (7.2 m/s equivalent collection speed).

Two independent electrospinning collection runs were performed (named "Experiment 1" and "Experiment 2"), both within chamber temperature and humidity ranges of 23.3-25 °C and 20-24% RH. The electrospinning was kept stable with minor adjustments in the infusion flow rate. The needle voltage was adjusted between 9.86 and 13.1 kV in Experiment 1 and was kept constant at 14.4 kV in Experiment 2. The top plate electrode voltage was 6.12 kV in Experiment 1 and 6.57 kV in Experiment 2. The wire drum was Earth grounded through its supporting structure. The collection time was about 90 minutes.

4.2.3. Samples preparation for mechanical testing

Fiber samples for mechanical testing were prepared as aligned fibers cemented between two paper frames, as shown in Figure 4.7. First, a strand of fibers at a selected location on the wire drum was isolated using a razor blade by separating the neighboring fibers away on either side. Second, a paper frame with a thin layer of epoxy applied to its top and bottom was adhered to the back side of the strand of isolated fibers (still on the wire drum). Third, immediately after the first paper frame was glued, a second paper frame (also with epoxy) was placed over the first frame from the front side. After letting the epoxy cure for 24 hrs, we cut the fibers outside of the frame to release the sample, as shown in Figure 4.7 (Framing). The samples prepared in this way had a uniform distribution of fibers and were easy to handle. These steps are similar, although not precisely equal to the guidelines of ASTM D3822 / Designation D3822M -14 [49]. For each Experiment (1 and 2), several samples were taken from the drum at two axial locations between different wires (Figure 4.7). The samples were inspected and those free of imperfections (excessive epoxy or damaged fibers) were set aside for mechanical testing.

The weight of the exposed part of the fibers in each test sample, M, was typically below 0.2 mg, and was determined as follows: The larger mass of a reference sample taken from the same axial position on the wire drum was determined. The dimensions of this reference sample were larger so that the error on its weight could be acceptably low. The reference sample had a similar width as that of the test sample but was longer (by a factor of about 3). We then scaled its mass down by the ratios of frontal areas (width × length) of the test and reference samples. This proportion must be fulfilled because the fiber properties and width-over-area density must be the same for a given position on the rotating drum. A Mettler Toledo XS205DU balance with 0.01 mg resolution was used. Therefore, the uncertainty in the test sample mass was reduced to about 5%.

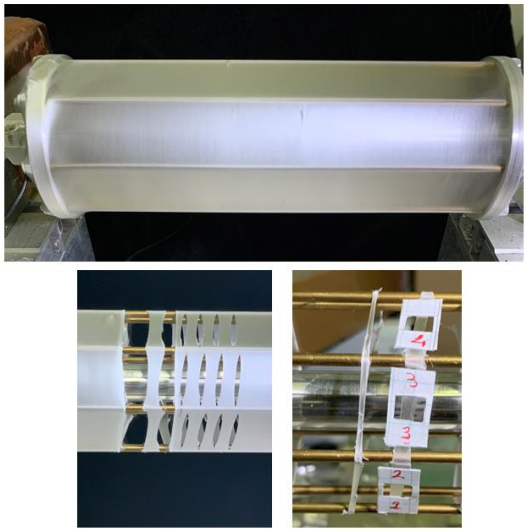

Figure 4.7. Aligned fibers collected on a wire drum and sample preparation.

4.2.4. Mechanical testing

Tensile tests were performed at 30 °C in a dynamic mechanical analyzer (DMA) (TA Instruments, Q800) equipped with an 18 N load cell (resolution of 1 mN), fitted with a film tension clamp. The paper-framed samples were placed in the DMA by clamping the top and down grip areas (where epoxy is present). Next, the sides of the paper frames were cut with fine scissors, and the automated chamber closing, and tensile test routines were initiated, and the corresponding force (N)-displacement (μm) curves were obtained. The tests were run at a constant force ramp rate of 0.1 N/min.

Converting the displacement data to strain involves knowing the initial fiber length L0. It was determined from photos of the frames before the tensile testing, as the length of fiber in the open space of the frame which was free of any epoxy. The initial fiber length of each test sample was determined on the sample photo as the average of the lengths obtained at 10 positions along the width of the sample, determined by means of ImageJ (Figure 4.8).

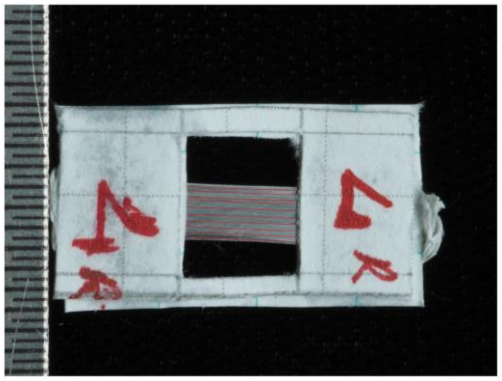

Figure 4.8. Representation of ImageJ lines (red) for the initial sample length measurement

4.2.5. Individual fiber porosity (IFP) determination

The individual fiber porosity (Φ) was computed as $\Phi=1-A_{annealed}/A_{as\text{-}spun}$. The details of the method are previously explained in Chapter 3.2.

4. 2.6. Scanning Electron Microscopy (SEM)

All SEM samples were gold coated with a layer thickness of ~43 nm prior to imaging. Micrographs of the fibers were obtained with a JEOL JSM 6400 apparatus and were used for determining their diameter. After electrospinning, we sampled fibers from the wire drum by approaching from behind the aluminum SEM sample support with carbon tape affixed. These fibers were from the exact same axial location on the wire drum as that of the fibers used in the mechanical test; although were taken between different drum wires than the samples used in the mechanical test. To prevent the stretching of these fibers during this operation, we cut them carefully around the SEM support. The fiber diameter measurements were made "manually" on the images with the aid of ImageJ (version 1.52p).

4.2.9. TGA

A Perkin-Elmer TGA7 thermogravimetric analyzer apparatus was used to investigate the presence of any residual solvent in the fibers. The analysis was performed at 2 °C/min in a nitrogen atmosphere to prevent fiber oxidation. A specific batch of fiber was made for this purpose. The fibers were left in a Petri dish for 24 hours before the TGA analysis.

4.3. Results and Discussion

4.3.1. Production and characterization of aligned PCL nanofibers

We prepared aligned nanofibers of polycaprolactone (PCL) by electrospinning a solution of this polymer in a mixture of chloroform and methanol (see Experimental Section). We have specifically chosen this challenging material to better demonstrate the capabilities of our mechanical testing method since leathery materials do not exhibit a clear linear elastic (Hookean) region in their stress-strain curves. Figure 4.5 summarizes the electrospinning process and subsequent steps needed to obtain the stress versus strain curve from a given sample of fibers. Such a curve reflects the average mechanical behavior for the fibers in a sample, and is dependent on the microstructure of the fibers and the molecular arrangements of the polymer chains in that structure. The electrospinning process conditions can result in changes in fiber microstructure. For example, smaller fiber sizes typically result in higher polymer chain orientation, resulting in a stronger mechanical response [11, 13, 16, 23, 26].

During electrospinning, the PCL fiber whipped in the air while solvent evaporated (Figure 4.5). The PCL fiber was collected on a wire drum composed of parallel wires, which rotated at a constant speed (Figure 4.5). The fibers directly harvested from the wire drum displayed high alignment and smooth walls, as demonstrated by SEM images (Figures 4.9a,c). Alignment of the fibers during collection is possible despite the whipping motion when the rotation speed at the collection

point (or fiber take-up speed) (7.2 m/s in our case) is comparable to the fiber production speed (length of fiber arriving at the collector per unit time). Much higher fiber alignment would require take-up speeds greatly exceeding the fiber production speed. This would cause the fibers to stretch while suffering structural, morphological -and thus mechanical- changes [33, 50, 51, 52]. Only when the fiber whipping can be suppressed, can very high fiber alignment be achieved at the critical condition of speed matching [33]. For these reasons, in our experiments, in which the fibers whipped, we sought a moderate take-up speed condition, for which the fiber alignment was high enough to be able to consider the fibers as having equivalent orientation, but not so high as to cause mechanical stretching which would cause a diameter change as well as profound structural changes.

Figures 4.9b,d show the histograms of fiber widths determined from several SEM images. The fibers' widths are submicron with a narrow dispersion, with a sample average diameter of 665 nm in Experiment 1 and 605 nm in Experiment 2, and standard deviations of 147 and 114 nm, respectively. Although the difference between the two averages is small, it has statistical significance by Student's t-test. The smoothness of the fiber wall is an indication that the fibers are circular. PCL fibers by electrospinning were reported to be circular in several works [39, 53] . We confirmed the circularity of our PCL fibers by imaging the cross-sections of fibers cut by FIB (Figure 11b in Chapter 3). As the presence of solvent can drastically change the mechanical behavior of polymeric materials [54], we analyzed a sample thermo-gravimetrically (Figure 4.10). Heating the sample up to 200 °C resulted in only 1% mass loss, proving that no solvent residue is significantly present in the polymer matrix. Further confirming this conclusion, the melting peak of PCL in the heat flow curve is observed at 62 °C.

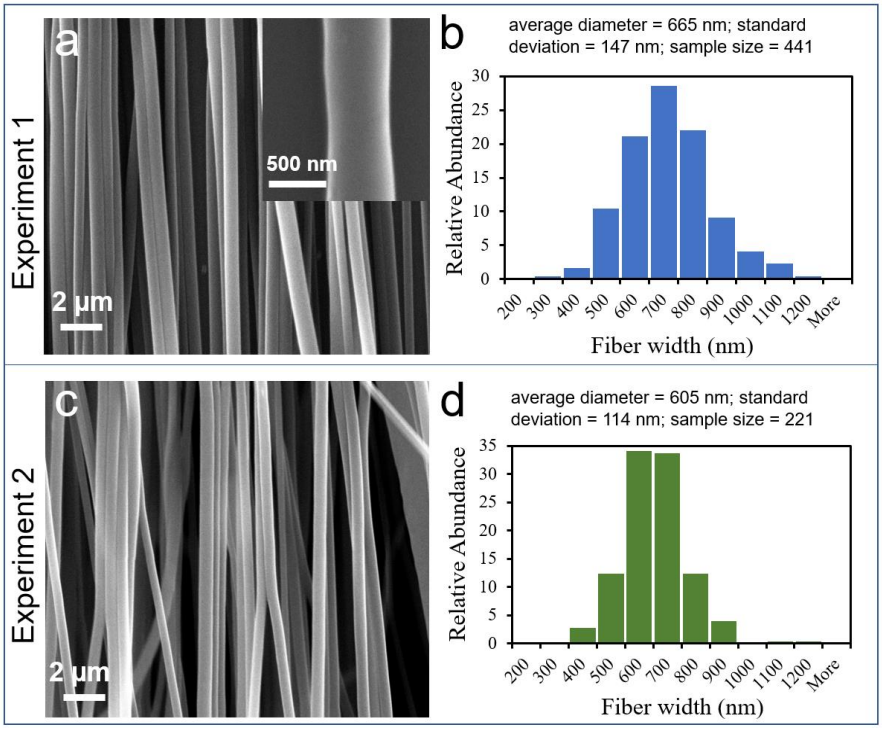

Figure 4.9. a) SEM image of the fibers obtained from Experiment 1. The inset shows the smooth wall of the fiber. b) SEM image of the fibers obtained from Experiment 2. c) Size distribution histogram of PCL nanofibers from Experiment 1 (average diameter = 665 nm; standard deviation = 147 nm; sample size = 441). (Experiment 1) and d) from Experiment 2 (average diameter = 605 nm; standard deviation = 114 nm; sample size = 221).

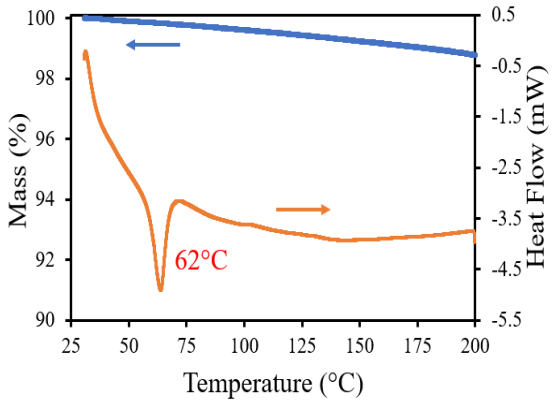

Figure 4.10. TGA curve of PCL/Chloroform/Methanol fibers

Note that observing smooth-walled circular fibers by SEM does not imply that the fibers are compact inside, e.g. polystyrene nanofibers spun from DMF solutions [33, 55]. Therefore, we investigated the individual fiber porosity (IFP) of PCL fibers. (Chapter 3)

Sample rejection criteria

Samples with damaged fibers or visibly non-uniform fiber coverage were rejected because we aimed to have as uniform load distribution as possible. Figure 4.11 shows examples of rejected samples. These situations were either caused by errors in sample preparation. One of the errors was caused by non-uniform ingress of epoxy into the fibers window. Epoxy was used to glue the fibers to the paper frame (both frame halves). The presence of epoxy in the fibers window was not cause of sample rejection, only if the extent of the epoxy varied too much. For each valid sample, the stretchable length of the fibers (initial fiber length, L_0) was determined excluding the length occupied by any excessive epoxy visible in the frame window. The tensile testing did not alter the part of the fibers which was covered with epoxy, as shown in Figure 4.12b,c. We determined the length of the epoxy ingress into the fibers in the frame window (Figure 4.12a) before and after the mechanical test. We showed that the length of the epoxy remained the same before and after the mechanical test, thus proving that the epoxy did not contribute to the mechanical test. After this was verified, in the fiber length determination of each sample, we determined the sample's fiber length as the average of 10 measurements of fiber length, excluding the length occupied by the epoxy, which were approximately evenly distributed across the sample (Figure 4.8).

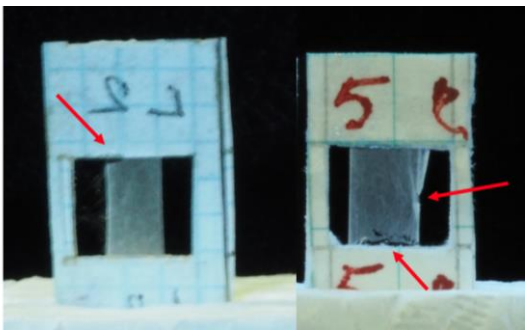

Figure 4.11. Examples of rejected samples. Imperfections (fiber sample damage) are indicated with red arrows and were caused by errors during sample preparation.

During the mechanical tests, the fibers in most samples broke in the middle between the clamping points, and this was taken as a criterion for validity of the test. However, in three cases out of 20 framed samples (all 3 in Experiment 2), the test was rejected due to incorrect procedure. This includes the cases of Figure 4.11, which underwent mechanical testing, and only afterwards we noticed their imperfections in the initial sample, shown in the figure. In another sample tested, the fibers broke near the clamp where the epoxy overflowed non-uniformly. In another test, the frame slipped out of the clamp due to poor clamping.

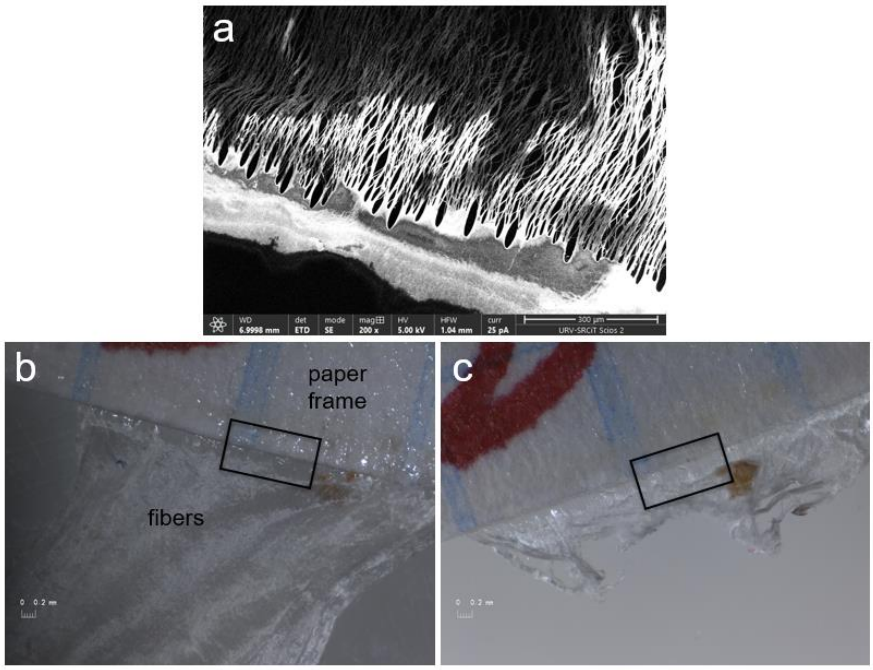

Figure 4.12. a) SEM images of the edge of a sample after mechanical testing, showing the overflow of epoxy. b) Epoxy length before the mechanical test (c) and after the mechanical test

4.3.2. Tensile stress-strain behavior

We determined the tensile behavior of single nanofibers by axially pulling large collections of nearly identical aligned fibers. The fibers had an extremely large

aspect ratio individually (~10^4). In this way, the load was uniformly distributed across all the aligned fibers in the sample.

Dynamic Mechanical Analyzer (DMA) uniaxial tensile tests were performed in two independent electrospinning experiments (1 and 2) with a total of 17 samples. The corresponding force-displacement curves are shown in Figures 4.13a, b. As expected, the curves are distinct because the number of fibers (N) and average initial fiber length (L_0) varied from sample to sample (see Table 2). To determine the stress-strain curves from the force F versus displacement ΔL curves obtained, the force F was converted to engineering stress σ by dividing F by the aggregate initial cross-sectional area of the fibers in the sample S, while the engineering strain ε is the ratio of the displacement ΔL by L_0:

$$\sigma = F/S \qquad \varepsilon = \Delta L / L_0 \qquad (1,2)$$

S is the sum of individual cross-sectional areas of all the fibers in the sample before stretching and is computed as the average cross-sectional area (s_1) of a single fiber in the sample times number of fibers in the sample N [31]. However, in our case N is tens of thousands; therefore, we obtained S from the ratio of the aggregate volume of the fibers V and the average length of the fibers L in reference samples (see section 4.2.3) as:

$$S = V / L = \frac{M}{L\rho_p(1-\Phi)} \qquad (3)$$

where V is obtained from the mass of the fibers M and their density $\rho_p(1-\Phi)$, where ρ_p is the known density of the bulk polymer, and Φ is the fibers' average porosity (which we established as Φ=0; section 3.5.1). After combining equations (1) and (3), the stress can be expressed as a function of known quantities:

$$\sigma = F / S = F\ L\ [\rho_p(1-\Phi)] / M \qquad (4)$$

Although the number of fibers in each sample N was not needed to compute the stress, it was nonetheless computed. It was obtained by dividing S by the mean cross-sectional area of a single fiber $s_1 = \frac{\sum_{i=1}^{n} \frac{\pi}{D^2}/4}{n}$, where d is the diameter of the individual fibers determined by SEM which were used in the size histogram (Figure 9b,d), as:

$$N = S / s_1 = M / (s_1 L [\rho_p(1-\Phi)]) \quad (5)$$

Sample parameters N, L_0, widths are listed in Table 1.

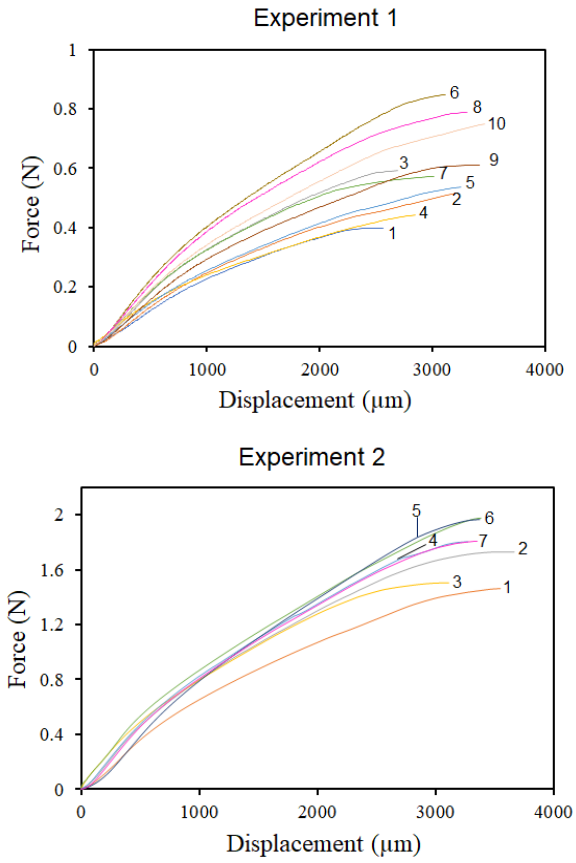

Figure 4.13. Force-Displacement curves for the samples from Experiments 1 and 2. The curves are labeled with the sample number.

The stress-strain curves for the two experiments are obtained from Figure 4.13 using equations (4) and (2) are shown in Figures 4.14. The curves overlap, with a narrow spread, indicating consistency between the different samples from a single experiment. At the same time, such consistency proves that the proper normalizing factors for the force and the displacement (in Equations (1) and (2)) have been considered. Additionally, a good agreement exists between the two experiments.

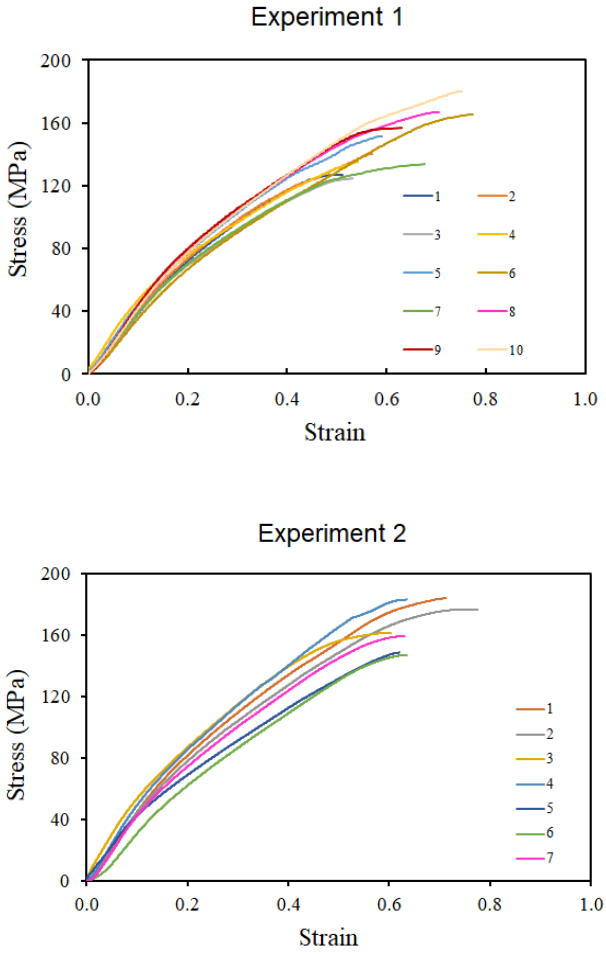

Figure 4.14. Stress-strain curves for the samples from Experiments 1 and 2. The legends show the sample number.

For each stress-strain curve in Figure 4.14, we extracted the following mechanical parameters, listed in Table 1: Maximum slope (MS) stress (stress at the tangent point), MS strain (strain at the tangent point), tangent modulus (slope at the tangent point), stress at break, strain at break, and the energy absorbed per volume of material (toughness). The combined stress-strain curves of experiment 1 and 2 are shown in Figure 4.15. It shows that the curves for single fibers are very similar from different experiments and samples with different numbers of fibers. The standard deviations for these variables were small, indicating that the data clustered around their mean values. Both experiments (1 and 2) exhibit similar means for all the variables, despite some statistical differences according to the Student's t-test's p-values (Table 1). The tangent modulus was 480 and 506 MPa for experiments 1 and 2, respectively. These values are anticorrelated with fiber size (Figure 4.9), a trend which has been reported in previous tensile studies on single PCL electrospun fibers below ~1-micron diameter [11, 12, 13]. Similar size dependence of the tensile modulus has also been found for single nanofibers of other polymers by various methods: tensile testing [16, 17], AFM-based mechanical testing [23, 26] and by other techniques [29]. It has been associated with the increased molecular orientation of the polymer chains as the fiber becomes smaller in electrospinning. [4]

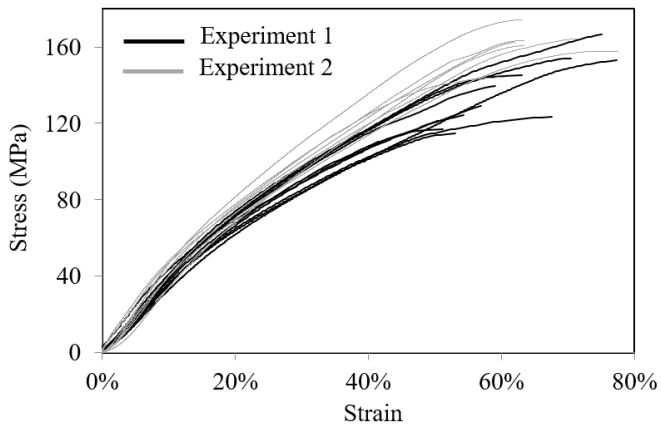

Figure 4.15. Combined stress-strain curves for Experiments 1 and 2.

A point of interest is how contacts between fibers may influence the result of the tensile test. A large number of fibers in each sample leads to numerous contact points between the fibers. Such points give mechanical cohesiveness to the fiber set, as revealed in the hourglass shape adopted by the sample during stretching. Hypothetically, two perfectly aligned fibers that are in contact along their lengths will stretch uniaxially in solidarity, provided both fibers have a uniform diameter and mechanical moduli along their lengths (even if the fibers have different diameters and moduli). In such an idealized case, the "contact point" is, in fact, a line of contact, and the contact stresses have a zero net contribution to the force along the axial direction. In our real samples, the lack of perfect alignment between the fibers precludes such lines of contact, but will inevitably result in a multitude of small contact regions, instead. In either case, the contact regions occupy a negligible fraction of the aggregate cross-sectional area *S*, and play a negligible role in the mechanical response of the sample during the tensile test. The breaking of the aligned fibers is shown in a supporting video, which shows that the fibers' stretch homogeneously, indicating that the contact points played a negligible role in the fiber stretching. (This test was not performed in the DMA, where the fibers cannot be visualized, but in a separate tester; see the QR code). The video shows that the sample did not display any kind of global behavior while stretching, of the kind which is typically observed in bulk samples, where an hourglass shape is developed.

Table 4.2. Sample dimensions, number of fibers and tensile properties of tested samples.

Sample	Width (mm)	Initial length (mm)	Number of fibers /10^3 Eq. 5	Maximum slope stress (MPa)	Maximum slope strain (%)	Tangent modulus (MPa)	Stress at break (MPa)	Strain at break (%)	Toughness (kJ/m3)
Experiment 1									
1	2.42	5.00	8.62	30.0	7.5	454	137	51	82
2	2.83	5.63	10.1	21.8	6.6	509	151	57	90
3	3.66	5.08	13.0	26.2	7.1	475	134	53	68
4	2.52	5.24	9.0	26.2	4.5	551	145	54	89
5	2.72	5.50	9.7	24.9	5.1	513	163	59	90
6	3.62	4.03	14.1	19.5	5.2	420	173	77	111
7	3.03	4.46	11.8	23.7	5.9	421	140	68	91
8	3.35	4.69	13.0	27.3	5.9	461	174	70	108
9	2.74	5.42	10.7	19.4	4.7	510	164	63	102
10	2.93	4.61	11.4	30.9	7.2	483	188	75	127
Mean				25.0	6.0	480	157	63	96
STDEV				3.6	0.9	43	18	9	17
Experiment 2									
1	3.56	4.98	26.6	28.8	6.8	547	184	71	91
2	4.38	4.73	32.8	18.9	4.6	516	177	78	97
3	4.17	5.15	31.3	26.2	4.2	547	162	60	72
4	4.41	5.16	33.1	15.9	3.5	564	183	63	79
5	5.00	5.45	36.5	24.9	5.3	456	149	62	59
6	5.03	5.32	36.7	25.6	7.3	404	147	63	59
7	4.26	5.32	31.1	18.9	4.1	504	159	63	67
Mean				22.7	5.1	506	166	66	75
STDEV				4.8	1.4	57.3	15.8	6.2	15.0
p-value (two-tail)				0.33	0.21	0.34	0.295	0.43	0.02

The tangent modulus from our samples (Table 4.2 and Figure 4.14) is compared to tensile moduli on single electrospun nanofibers, from studies which reported low noise curves obtained using high sensitivity load cells [11, 13]. Our tangent moduli are slightly higher than Lim et al.'s (fiber diameter = 350 nm) [13], and about twice those reported by Wong et al.'s (fiber diameter = 900 nm) [11]. Differences between studies are not unexpected due to various factors, particularly crystallinity and polymer chains' alignment, which can be enhanced by stretching from the collecting drum in our case (as no drum was used in any of the single-fiber works). Another unknown factor is whether the fibers in those works had any individual fiber porosity, whereas our fibers' porosity is inexistent or very low.

The tangent modulus from our samples can also be compared to tensile moduli obtained from macroscopic PCL samples. Data different such studies vary from 216 to 440 MPa (see Table 4.3). This variability is not unexpected as differences in tensile modulus can arise from various factors, such as polymer molecular weight, crystallinity, manufacturing, and testing conditions (e.g. strain rate, temperature). Our moduli (480 and 506 MPa, from Table 4.2) fall above the macroscopic-sample moduli. This is not surprising, as the polymeric chains are strongly aligned uniaxially in the direction of the fiber, as was revealed by the XRD data (Section 3.2).

Besides tensile modulus, bulk and electrospun PCL samples differ greatly in the plastic deformation region of the stress-strain curves. Figure 4.16 displays two bulk-PCL studies, corresponding to injection and compression molding [56, 57], as well as three electrospun fiber samples, one from this study plus two single-fiber studies with low noise [11, 13]. The two bulk-PCL samples display viscoplastic behavior with extreme elongations due to necking, where a strain-hardened neck region develops whose width remains nearly constant with increasing strain [37, Chapter 9]. This phenomenon allows for very large sample elongations before the break (ranging from several times to over 10 times the original sample length) and has been found in other studies (Table 4.3). On the other hand, the stress vs. strain curves for the fibers made by electrospinning in Figure 4.16 show much different behavior. The fibers sustain much higher stresses before breaking than PCL bulk samples, suggesting that they undergo significant strain hardening without necking. Nonetheless, necking has been observed by SEM in electrospun fiber mats (including PCL), typically occurring at multiple locations along the fiber [58, 59, 60, 61,62].

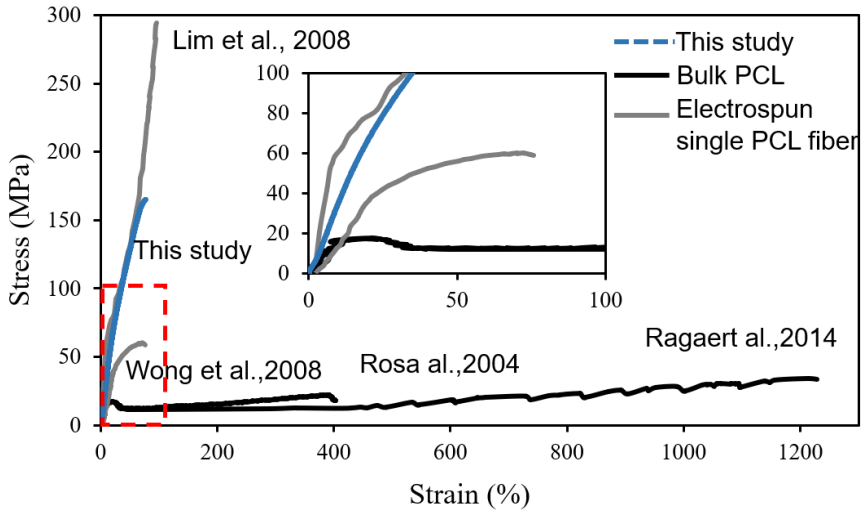

Figure 4.16. Comparison of the engineering stress-strain curves from this study and from others for electrospun and bulk PCL from the literature (Lim 2008, Wong 2008, Rosa 2004, Ragaert 2014). All studies except ours were performed at constant strain rate (whereas constant stress rate was used in our case). The trace shown for our study corresponds to sample 6 from Experiment 1.

Table 4.3. Bulk tensile mechanical properties and test conditions of PCL reported in the literature.

First Author	Year	Reference	Fabrication method	Mw (kDa)	Strain rate (% /min)	Stress at break (MPa)	E (MPa)	Tensile strength (MPa)	Specimen length (mm)	Elongation rate (mm/min)	Elongation rate (% /s)	Crystallinity (wt %)
Rosa	2004	[57]	Compression molding	80	143	18	425	16.9	35	50	2.38	11
Lepoittevin	2002	[65]	Compression molding	50	-	-	216	37	-	50	-	52.4
Ragaert	2014	[56]	Injection molding	84.5	278	35	440	34	36	100	4.63	56
Correlo	2005	[66]	Injection molding	124	25	-	378	27.3	20	5	0.42	-
Granado	2008	[67]	Injection molding	80	-	-	300	14	-	-	-	42
Eshraghi	2010	[68]	Laser Sintering (∥)	73*	88	-	363	10.5	57	50	-	-
Eshraghi	2010	[68]	Laser Sintering (⊥)	73*	88	-	343	16.1	57	50	1.46	56
Pitt	1981	[69]	Melt extrusion	84.5	-	-	265	-	200	-	-	45
Feng	1983	[70]	-	50.4	-	-	-	273	-	-	-	-

*M_n

4.4 Conclusions

We presented a new method to characterize the tensile properties of nanofibers made by electrospinning. The method considers a large collection of similar fibers which are collected in an aligned fashion. Such collections of fibers are much easier to manipulate than single fibers, as done in previous studies. In addition, the new method does not require obtaining the size (cross-section) of the single fiber for the force-to-stress conversion. In our method, instead, the cross-section for each sample is computed from the mass of the fibers and their density. This method is very robust and was demonstrated on PCL nanofibers, to show that it can be used even with rubbery and weak materials, for which methods based on isolating single fibers become extremely challenging. We obtained consistent tensile properties across different samples made of fibers produced in the same electrospinning experiment. Two independent experiments led to slight differences in such properties.

In summary, the method presented in this study introduces a new dimension to the characterization of nanofiber tensile properties. Its robustness, simplicity, and ability to provide consistent results across varying experimental conditions highlight its potential for becoming a standard in the field of nanofiber research. As nanofibers continue to find applications in an array of industries, ranging from biomedical engineering to advanced materials, this method opens doors for more accurate material assessment and design, ultimately driving progress and innovation.

4.7. References

[1] Pelham, R. J., & Wang, Y. (1997). Cell locomotion and focal adhesions are regulated by substrate flexibility. Proceedings of the National Academy of Sciences, 94(25), 13661– 13665.

[2] Evans, N. D., & Gentleman, E. (2014). The role of material structure and mechanical properties in cell-matrix interactions. *Journal of Materials Chemistry B*, *2*(17), 2345–2356.

[3] Davidson, M. D., Song, K. H., Lee, M.-H., Llewellyn, J., Du, Y., Baker, B. M., Wells, R. G., & Burdick, J. A. (2019). Engineered Fibrous Networks To Investigate the Influence of Fiber Mechanics on Myofibroblast Differentiation. *ACS Biomaterials Science & Engineering*, *5*(8), 3899–3908.

[4] Richard-Lacroix, M., & Pellerin, C. (2013). Molecular Orientation in Electrospun Fibers: From Mats to Single Fibers. *Macromolecules*, *46*(24), 9473–9493.

[5] Rashid, T. U., Gorga, R. E., & Krause, W. E. (2021). Mechanical Properties of Electrospun Fibers—A Critical Review. *Advanced Engineering Materials*, *n/a*(n/a), 2100153.

[6] Silberstein, M. N., Pai, C.-L., Rutledge, G. C., & Boyce, M. C. (2012). Elastic–plastic behavior of non-woven fibrous mats. *Journal of the Mechanics and Physics of Solids*, *60*(2), 295–318.

[7]Durville, D. (2010). Simulation of the mechanical behaviour of woven fabrics at the scale of fibers. *International Journal of Material Forming*, *3*(SUPPL. 2), 1241–1251. https://doi.org/10.1007/s12289-009-0674-7

[8]Stylianopoulos, T., Bashur, C. A., Goldstein, A. S., Guelcher, S. A., & Barocas, V. H. (2008). Computational predictions of the tensile properties of electrospun fibre meshes: Effect of fibre diameter and fibre orientation. *Journal of the Mechanical Behavior of Biomedical Materials*, *1*(4), 326–335. https://doi.org/10.1016/j.jmbbm.2008.01.003

[9]Wei, X., Xia, Z., Wong, S. C., & Baji, A. (2009). Modelling of mechanical properties of electrospun nanofibre network. *International Journal of Experimental and Computational Biomechanics*, *1*(1), 45. https://doi.org/10.1504/ijecb.2009.022858

[10] Singh, U., Prakash, V., Abramson, A. R., Chen, W., Qu, L., & Dai, L. (2006). Mechanical characterization device for in situ measurement of nanomechanical properties of micro/nanostructures. *Applied Physics Letters*, *89*(7), 73103. https://doi.org/10.1063/1.2271576

[11] Wong, S. C., Baji, A., & Leng, S. (2008). Effect of fiber diameter on tensile properties of electrospun poly(ε-caprolactone). *Polymer*, *49*(21), 4713–4722. https://doi.org/10.1016/j.polymer.2008.08.022

[12] Tan, E. P. S., Ng, S. Y., & Lim, C. T. (2005). Tensile testing of a single ultrafine polymeric fiber. *Biomaterials*, *26*(13), 1453–1456.

[13] Lim, C. T., Tan, E. P. S., & Ng, S. Y. (2008). Effects of crystalline morphology on the tensile properties of electrospun polymer nanofibers. *Applied Physics Letters*, 92(14), 141908.

[14] Stachewicz, U., Dijksman, J. F., Soudani, C., Tunnicliffe, L. B., Busfield, J. J. C., & Barber, A. H. (2017). Surface free energy analysis of electrospun fibers based on Rayleigh-Plateau/Weber instabilities. *European Polymer Journal*, *91*, 368–375.

[15] Chen, F., Peng, X., Li, T., Chen, S., Wu, X. F., Reneker, D. H., & Hou, H. (2008). Mechanical characterization of single high-strength electrospun polyimide nanofibres. *Journal of Physics D: Applied Physics*, *41*(2), 25308.

[16] Pai, C.-L., Boyce, M. C., & Rutledge, G. C. (2011). Mechanical properties of individual electrospun PA 6(3)T fibers and their variation with fiber diameter. *Polymer*, *52*(10), 2295–2301.

[17] Papkov, D., Zou, Y., Andalib, M. N., Goponenko, A., Cheng, S. Z. D., & Dzenis, Y. A. (2013). Simultaneously Strong and Tough Ultrafine Continuous Nanofibers. *ACS Nano*, *7*(4), 3324–3331. https://doi.org/10.1021/nn400028p

[18] Chew, S. Y., Hufnagel, T. C., Lim, C. T., & Leong, K. W. (2006). Mechanical properties of single electrospun drug-encapsulated nanofibres. *Nanotechnology*, *17*(15), 3880–3891.

[19] Baker, S., Sigley, J., Helms, C. C., Stitzel, J., Berry, J., Bonin, K., & Guthold, M. (2012). The mechanical properties of dry, electrospun fibrinogen fibers. *Materials Science and Engineering: C*, *32*(2), 215–221.

[20] Baker, S. R., Banerjee, S., Bonin, K., & Guthold, M. (2016). Determining the mechanical properties of electrospun poly-ε-caprolactone (PCL) nanofibers using AFM and a novel fiber anchoring technique. *Materials Science and Engineering C*, *59*, 203–212.

[21] Carlisle, C. R., Coulais, C., Namboothiry, M., Carroll, D. L., Hantgan, R. R., & Guthold, M. (2009). The mechanical properties of individual, electrospun fibrinogen fibers. *Biomaterials*, *30*(6), 1205–1213.

[22] Sharpe, J. M., Lee, H., Hall, A. R., Bonin, K., & Guthold, M. (2020). Mechanical Properties of Electrospun, Blended Fibrinogen: PCL Nanofibers. In *Nanomaterials* (Vol. 10, Issue 9, p. 1843). https://doi.org/10.3390/nano10091843

[23] Wingert, M. C., Jiang, Z., Chen, R., & Cai, S. (2017). Strong size-dependent stress relaxation in electrospun polymer nanofibers. *Journal of Applied Physics*, *121*(1), 15103.

[24] Croisier, F., Duwez, A.-S., Jérôme, C., Léonard, A. F., van der Werf, K. O., Dijkstra, P. J., & Bennink, M. L. (2012). Mechanical testing of electrospun PCL fibers. *Acta Biomaterialia*, *8*(1), 218–224.

[25] Zussman, E., Burman, M., Yarin, A. L., Khalfin, R., & Cohen, Y. (2006). Tensile deformation of electrospun nylon-6,6 nanofibers. *Journal of Polymer Science Part B: Polymer Physics*, *44*(10), 1482–1489.

[26] Shin, M. K., Kim, S. I., Kim, S. J., Kim, S.-K., Lee, H., & Spinks, G. M. (2006). Size-dependent elastic modulus of single electroactive polymer nanofibers. *Applied Physics Letters*, *89*(23), 231929.

[27] Song, X., Liu, W., Wang, J., Xu, S., Liu, B., Cai, Q., & Ma, Y. (2018). Highly aligned continuous mullite nanofibers: Conjugate electrospinning fabrication, microstructure and mechanical properties. *Materials Letters*, *212*, 20–24.

[28] Wang, M., Jin, H.-J., Kaplan, D. L., & Rutledge, G. C. (2004). Mechanical Properties of Electrospun Silk Fibers. Macromolecules, 37(18), 6856–6864.

[29] Burman, M., Arinstein, A., & Zussman, E. (2008). Free flight of an oscillating string pendulum as a tool for the mechanical characterization of an individual polymer nanofiber. *Applied Physics Letters*, *93*(19), 193118.

[30] Bazbouz, M. B., & Stylios, G. K. (2010). The tensile properties of electrospun nylon 6 single nanofibers. *Journal of Polymer Science, Part B: Polymer Physics*, *48*(15), 1719–1731.

[31] Yao, J., Pantano, M. F., Pugno, N. M., Bastiaansen, C. W. M., & Peijs, T. (2015). High-performance electrospun co-polyimide nanofibers. *Polymer*, *76*, 105–112.

[32] Tan, E. P. S., & Lim, C. T. (2004). Novel approach to tensile testing of micro- and nanoscale fibers. *Review of Scientific Instruments*, *75*(8), 2581–2585. https://doi.org/10.1063/1.1775309

[33] Kiselev, P., & Rosell-Llompart, J. (2012). Highly aligned electrospun nanofibers by elimination of the whipping motion. *Journal of Applied Polymer Science*, *125*(3), 2433–2441.

[34] Pai, C.-L., Boyce, M. C., & Rutledge, G. C. (2009). Morphology of Porous and Wrinkled Fibers of Polystyrene Electrospun from Dimethylformamide. *Macromolecules*, *42*, 2102–2114. https://doi.org/10.1021/ma802529h

[35] Fashandi, H., & Karimi, M. (2012). Pore formation in polystyrene fiber by superimposing temperature and relative humidity of electrospinning atmosphere. *Polymer*, *53*(25), 5832–5849.

[36] Woodruff, M. A., & Hutmacher, D. W. (2010). The return of a forgotten polymer - Polycaprolactone in the 21st century. *Progress in Polymer Science*, *35*(10), 1217–1256. https://doi.org/10.1016/j.progpolymsci.2010.04.002

[37] J.L. Halary; F. Lauprêtre; L. Monnerie (2011). *Polymer Materials: Macroscopic Properties and Molecular Interpretations*. Wiley.

[38] Rahmati, M., Mills, D. K., Urbanska, A. M., Saeb, M. R., Venugopal, J. R., Ramakrishna, S., & Mozafari, M. (2021). Electrospinning for tissue engineering applications. *Progress in Materials Science*, *117*, 100721.

[39] Cipitria, A., Skelton, A., Dargaville, T. R., Dalton, P. D., & Hutmacher, D. W. (2011). Design, fabrication and characterization of PCL electrospun scaffolds - A review. *Journal of Materials Chemistry*, *21*(26), 9419–9453

[40] Shahin-Shamsabadi, A., Hashemi, A., Tahriri, M., Bastami, F., Salehi, M., & Mashhadi Abbas, F. (2018). Mechanical, material, and biological study of a PCL/bioactive glass bone scaffold: Importance of viscoelasticity. *Materials Science and Engineering C*, *90*, 280–288.

[41] Lee, K. H., Kim, H. Y., Khil, M. S., Ra, Y. M., & Lee, D. R. (2003). Characterization of nano-structured poly(ε-caprolactone) nonwoven mats via electrospinning. *Polymer*, *44*(4), 1287–1294

[42] Nisbet, D. R., Rodda, A. E., Horne, M. K., Forsythe, J. S., & Finkelstein, D. I. (2009). Neurite infiltration and cellular response to electrospun polycaprolactone scaffolds implanted into the brain. *Biomaterials*, *30*(27), 4573–4580.

[43] Karuppuswamy, P., Reddy Venugopal, J., Navaneethan, B., Luwang Laiva, A., & Ramakrishna, S. (2015). Polycaprolactone nanofibers for the controlled release of tetracycline hydrochloride. *Materials Letters*, *141*, 180–186.

[44] Kuzelova Kostakova, E., Meszaros, L., Maskova, G., Blazkova, L., Turcsan, T., & Lukas, D. (2017). Crystallinity of Electrospun and Centrifugal Spun Polycaprolactone Fibers: A Comparative Study. *Journal of Nanomaterials*, *2017*, 8952390.

[45] Bodnár, E., Grifoll, J., & Rosell-Llompart, J. (2018). Polymer solution electrospraying: A tool for engineering particles and films with controlled morphology. *Journal of Aerosol Science*, *125*, 93–118.

[46] Larsen, G., Spretz, R., & Velarde-Ortiz, R. (2004). Use of coaxial gas jackets to stabilize Taylor cones of volatile solutions and to induce particle-to-fiber transitions. *Advanced Materials*, *16*(2), 166–169.

[47] C. Lübbert, W. Peukert, The mass transfer at Taylor cones, J. Aerosol Sci. 123 (2018) 39–51.

[48] Teo, W. E., & Ramakrishna, S. (2006). A review on electrospinning design and nanofibre assemblies. *Nanotechnology*, *17*(14), R89–R106.

[49] ASTM D3822 / Designation D3822M -14, Standard Test Method for Tensile Properties of Single Textile Fibers, 2007

[50] Inai, R., Kotaki, M., & Ramakrishna, S. (2005). Structure and properties of electrospun PLLA single nanofibres. *Nanotechnology*, *16*(2), 208–213. https://doi.org/10.1088/0957-4484/16/2/005

[51] Chan, K. H. K., Wong, S. Y., Li, X., Zhang, Y. Z., Lim, P. C., Lim, C. T., Kotaki, M., & He, C. Bin. (2009). Effect of Molecular Orientation on Mechanical Property of Single Electrospun Fiber of Poly[(R)-3-hydroxybutyrate-co-(R)-3-hydroxyvalerate]. *The Journal of Physical Chemistry B*, *113*(40), 13179–13185.

[52] Zhang, X., Nakagawa, R., Chan, K. H. K., & Kotaki, M. (2012). Mechanical Property Enhancement of Polylactide Nanofibers through Optimization of Molecular Weight, Electrospinning Conditions, and Stereocomplexation. *Macromolecules*, *45*(13), 5494–5500.

[53] S. Metwally, J. E. Karbowniczek, P. K. Szewczyk, M. M. Marzec, A. Gruszczyński, A. Bernasik, U. Stachewicz, Adv. Mater. Interfaces 2019, 6, 1801211.

[54] Chen, M., Zhang, Y., Dong, C., & Xiao, Z. (2016). On-Line Auto Mass Measurement of Residual Solvent Mass and its Influence on Mechanical Properties of Propellants. *Propellants, Explosives, Pyrotechnics*, *41*(6), 972–977. https://doi.org/https://doi.org/10.1002/prep.201600053

[55] Demir, M. M. (2010). Investigation on glassy skin formation of porous polystyrene fibers electrospun from DMF. *Express Polymer Letters*, *4*(1), 2–8.

[56] Ragaert, K., De Baere, I., Degrieck, J., & Cardon, L. (2014). Bulk Mechanical Properties of Thermoplastic Poly-e-caprolactone. *Conferentie: 6e Polymers & Molds Innovations Conference*, *January 2015*.

[57] Rosa, D. S., Neto, I. C., Calil, M. R., Pedroso, A. G., Fonseca, C. P., & Neves, S. (2004). Evaluation of the thermal and mechanical properties of poly(ε-caprolactone), low-density polyethylene, and their blends. *Journal of Applied Polymer Science*, *91*(6), 3909–3914.

[58] Zussman, E., Rittel, D., & Yarin, A. L. (2003). Failure modes of electrospun nanofibers. *Applied Physics Letters*, *82*(22), 3958–3960. https://doi.org/10.1063/1.1579125

[59] Andersson, R. L., Ström, V., Gedde, U. W., Mallon, P. E., Hedenqvist, M. S., & Olsson, R. T. (2014). Micromechanics of ultra-toughened electrospun PMMA/PEO fibres as revealed by in-situ tensile testing in an electron microscope. *Scientific Reports*, *3*, 6335. https://doi.org/10.1038/srep06335

[60] Fischer, T., Möller, M., & Singh, S. (2019). Approach to Obtain Electrospun Hydrophilic Fibers and Prevent Fiber Necking. *Macromolecular Materials and Engineering*, *304*(12), 1900565. https://doi.org/https://doi.org/10.1002/mame.201900565

[61] Bayram, F. C., Kapçı, M. F., Yuruk, A., Isoglu, I. A., & Bal, B. (2021). Investigations of strain rate, size, and crack length effects on the mechanical response of polycaprolactone electrospun membranes. *Proceedings of the Institution of Mechanical Engineers, Part E: Journal of Process Mechanical Engineering*, 09544089211024065. https://doi.org/10.1177/09544089211024065

[62] Delp, A., Becker, A., Hülsbusch, D., Scholz, R., Müller, M., Glasmacher, B., & Walther, F. (2021). In Situ Characterization of Polycaprolactone Fiber Response to Quasi-Static Tensile Loading in Scanning Electron Microscopy. In *Polymers* (Vol. 13, Issue 13). https://doi.org/10.3390/polym13132090

[63] Szewczyk, P. K., Ura, D. P., & Stachewicz, U. (2020). Humidity controlled mechanical properties of electrospun polyvinylidene fluoride (Pvdf) fibers. *Fibers, 8*(10), 1–9.

[64] Chen, Z., Wei, B., Mo, X., Lim, C. T., Ramakrishna, S., & Cui, F. (2009). Mechanical properties of electrospun collagen–chitosan complex single fibers and membrane. *Materials Science and Engineering: C*, *29*(8), 2428–2435. https://doi.org/https://doi.org/10.1016/j.msec.2009.07.006

[65] Lepoittevin, B., Devalckenaere, M., Pantoustier, N., Alexandre, M., Kubies, D., Calberg, C., Jérôme, R., & Dubois, P. (2002). Poly(ε-caprolactone)/clay nanocomposites prepared by melt intercalation: mechanical, thermal and rheological properties. *Polymer*, *43*(14), 4017–4023.

[66] Correlo, V. M., Boesel, L. F., Bhattacharya, M., Mano, J. F., Neves, N. M., & Reis, R. L. (2005). Hydroxyapatite Reinforced Chitosan and Polyester Blends for Biomedical Applications. *Macromolecular Materials and Engineering*, *290*(12), 1157–1165.

[67] Granado, A., Eguiazábal, J. I., & Nazábal, J. (2008). Structure and mechanical properties of blends of poly(ε-caprolactone) with a poly(amino ether). *Journal of Applied Polymer Science*, *109*(6), 3892–3899. https://doi.org/https://doi.org/10.1002/app.28615

[68] Eshraghi, S., & Das, S. (2010). Mechanical and microstructural properties of polycaprolactone scaffolds with one-dimensional, two-dimensional, and three-dimensional orthogonally oriented porous architectures produced by selective laser sintering. *Acta Biomaterialia*, *6*(7), 2467–2476.

[69] Pitt, C. G., Chasalow, F. I., Hibionada, Y. M., Klimas, D. M., & Schindler, A. (1981). Aliphatic polyesters. The degradation of poly(ϵ-caprolactone) in vivo. *Journal of Applied Polymer Science*, *26*(11), 3779–3787.

[70] Feng (S. T. Voong), X. D., Song, C. X., & Chen, W. Y. (1983). Synthesis and evaluation of biodegradable block copolymers of ε-caprolactone and DL-lactide. *Journal of Polymer Science: Polymer Letters Edition*, *21*(8), 593–600. https://doi.org/https://doi.org/10.1002/pol.1983.130210802

[71] Engelberg, I., & Kohn, J. (1991). Physico-mechanical properties of degradable polymers used in medical applications: A comparative study. *Biomaterials*, *12*(3), 292–304. https://doi.org/10.1016/0142-9612(91)90037-B

Chapter 5. Use of nanofibers in Tissue Engineering, 3D rendering, and mechanical simulation.

"The possession of knowledge does not kill the sense of wonder and mystery.
There is always more mystery."
-Anais Nin

5.1. Aims and objectives of this work

In this chapter, we focused on vascular tissue engineering scaffolds made by electrospinning as well as we give an outlook on electrospun scaffolds in tissue engineering and regenerative medicine. We fabricated polyglycerol sebacate (PGS) and tropoelastin (TE) scaffolds at different ratios to observe their potential as small diameter blood vessels. To investigate the distribution of the materials used in the scaffold (PGS and TE) throughout the scaffold we did 3D rendering of multiphoton microscopy images and confirm if the ratio used in the electrospinning solution remains the same in the scaffold.

This work was performed during a research stay in Sydney during COVID pandemic. Due to the lockdown, we focused on the in-depth analysis of the data we previously obtained (provided by Weiss research group). However, thanks to the disposition of Prof. Weiss, Ziyu Wang and Dr. Suzanne M. Mithieux I felt welcome and was readily integrated into the research team's work and was able to contribute on the work described in this chapter.

5.2. Introduction to Tissue Engineering and Scaffolds

Tissue engineering is an interdisciplinary field that combines principles from biology, engineering, and medicine to create functional biological tissues for therapeutic and research purposes. It aims to regenerate or repair damaged or diseased tissues by utilizing a combination of cells, biomaterials, and biochemical factors [1,2].

One crucial aspect of tissue engineering is the use of scaffolds. Scaffolds provide a supportive framework for cells to attach, proliferate, and organize into functional tissue structures. These structures mimic the natural extracellular matrix (ECM) found in the body, which provides structural and biochemical cues to guide cell behavior. The extracellular matrix (ECM) is a complex and dynamic network of molecules that surrounds and supports cells within tissues and organs in multicellular organisms. It's a three-dimensional structure composed of various proteins, glycoproteins, proteoglycans, and polysaccharides secreted by cells themselves. Some examples of ECM are shown in Figure 5.1. The ECM provides structural integrity, mechanical support, and communication cues for cells, influencing their behavior and function. [3, 4]

Functions of the extracellular matrix include:

- Structural Support: The ECM forms a scaffold that helps maintain the structural integrity and shape of tissues and organs. It acts as a foundation upon which cells can organize and interact.
- Cell Adhesion: The ECM provides attachment sites for cells through specialized proteins called integrins. These adhesion sites are essential for cell anchoring and migration.
- Cell Signaling: The ECM contains signaling molecules that guide cell behavior, growth, and differentiation. These signals influence processes like cell proliferation, migration, and tissue repair.
- Barrier and Filtration: In certain tissues, the ECM can function as a barrier, preventing the movement of cells or molecules between

different compartments. It can also play a role in filtration processes, allowing specific molecules to pass through.

- Mechanical Support: The ECM contributes to the mechanical properties of tissues and organs. It helps absorb mechanical forces and distribute them throughout the tissue, contributing to overall tissue strength and flexibility.
- Tissue Development and Remodeling: During tissue development, the ECM plays a vital role in guiding cell differentiation and tissue organization. It also supports tissue repair and regeneration by providing a framework for new tissue formation.
- Homeostasis Maintenance: The ECM helps maintain tissue homeostasis (a self-regulating process by which a living organism can maintain internal stability while adjusting to changing external conditions) by regulating the concentration of growth factors, cytokines, and other signaling molecules. This contributes to balanced cell behavior and function.

The composition and properties of the ECM vary across different tissues and organs, adapting to the specific needs and functions of each tissue type. Overall, the extracellular matrix is a critical component of multicellular life, contributing to tissue structure, function, and regulation.

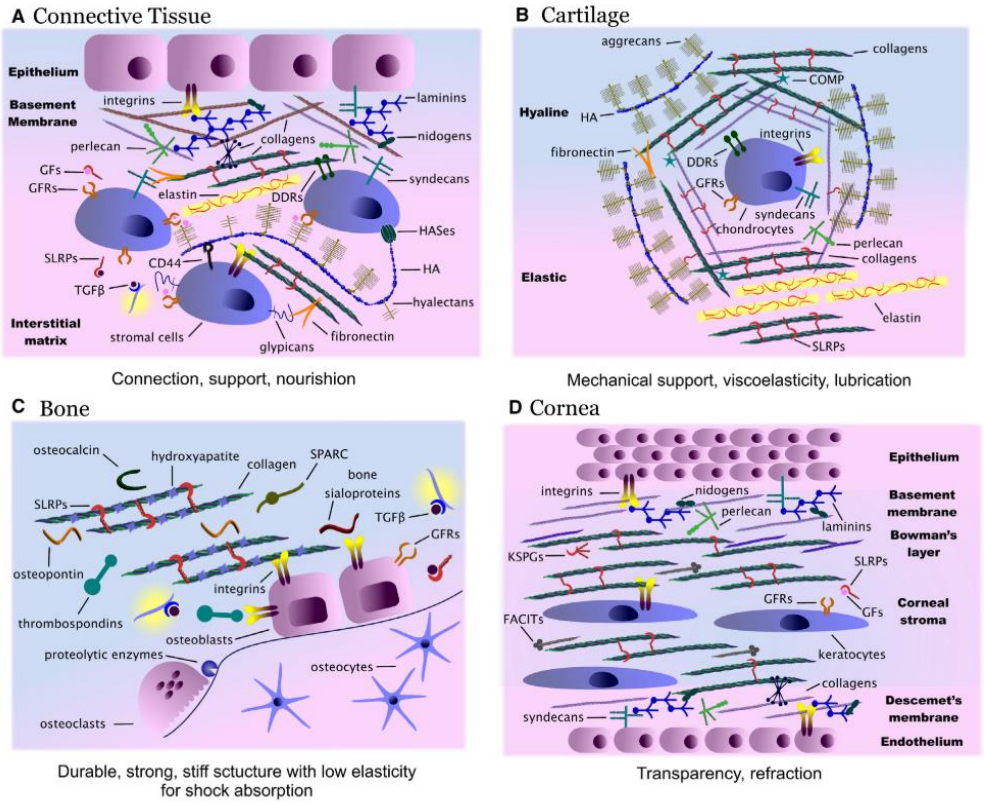

Figure 5.1. Examples of extracellular matrix. Adapted with permission from [3].

In tissue engineering applications, fibrous scaffolds have been utilized in various tissue types, including skin, bone, cartilage, nerve, and blood vessels [5, 6, 7, 8, 9]. Researchers have successfully demonstrated the ability of fibrous scaffolds to support cell attachment, proliferation, and differentiation, leading to the formation of functional tissues.

Nanofibrous scaffolds are a popular choice in tissue engineering due to their unique characteristics. Firstly, their high surface area-to-volume ratio allows for efficient nutrient and oxygen exchange, promoting cell viability and growth. Additionally, the fibrous structure can mimic the native tissue's mechanical properties, providing mechanical support to the developing tissue. They are composed of fibers arranged in a three-dimensional architecture, resembling the natural ECM. These fibers can be made from various materials, such as synthetic

polymers (e.g., polyglycolic acid, polyglycerol sebacate, polylactic acid, polycaprolactone), natural polymers (e.g., collagen, fibrin), or a combination of both [10, 11, 12, 13, 14].

Moreover, fibrous scaffolds can be engineered to possess specific characteristics that promote tissue regeneration. For instance, the fiber diameter, porosity, and surface chemistry can be tailored to control cell adhesion, migration, and differentiation [15]. Functionalization of the fibers with bioactive molecules, growth factors, or signaling molecules further enhances their ability to guide cellular behavior and tissue development [16].

Overall, nanofibrous scaffolds play a critical role in tissue engineering by providing a suitable microenvironment for cells to regenerate and develop into functional tissues. Continued research and advancements in scaffold design and fabrication techniques hold great promise for the future of tissue engineering, offering potential solutions for tissue repair and replacement in a wide range of clinical applications.

5.1.1. Concept of cell adhesion and proliferation

Cell adhesion refers to the process by which cells attach and bind to the extracellular matrix (ECM) or other neighboring cells. It is a fundamental step in tissue formation, as it provides structural integrity and allows cells to communicate with each other and the surrounding environment. Cell adhesion involves interactions between specific cell surface receptors, such as integrins, and proteins present in the ECM, including fibronectin and collagen [17].

To promote cell proliferation in tissue engineering, several factors are considered. First, providing a suitable microenvironment is crucial. This includes optimizing the scaffold properties, such as pore size, mechanical strength, and surface chemistry, to support cell growth and proliferation. The scaffold should also allow the diffusion of nutrients and oxygen while facilitating the removal of waste products [18, 19].

Secondly, the addition of growth factors or cytokines in the scaffold can stimulate cell proliferation. Growth factors are signaling molecules that regulate cell behavior, including proliferation. By incorporating growth factors into the scaffold or delivering them in a controlled manner, tissue engineers can influence cell proliferation rates and guide tissue development [20, 21].

Furthermore, the mechanical forces experienced by cells, such as fluid shear stress or mechanical stretching, can also impact cell proliferation. Applying appropriate mechanical cues to the engineered tissues can mimic the physiological conditions and stimulate cell growth and division. [22, 23, 24]

In summary, cell adhesion and proliferation are crucial aspects of tissue engineering. Promoting cell adhesion ensures proper cell-substrate and cell-cell interactions, while facilitating cell proliferation enables the formation of functional tissues. By understanding and manipulating these processes, tissue engineers aim to create artificial tissues and organs that can effectively restore or replace damaged or diseased tissues in the human body.

5.1.1. Other techniques to manufacture artificial scaffolds

There are several techniques used to produce artificial scaffolds for tissue engineering. The choice of technique depends on factors such as the desired scaffold structure, material properties, and the specific tissue engineering application. Here are some commonly employed techniques:

- **Porogen-based techniques:** Porogen-based techniques involve the use of sacrificial materials that are mixed with the scaffold material and subsequently removed to create a porous structure. One approach is the salt-leaching method, where salt particles are mixed with the polymer, and subsequent leaching with a solvent dissolve the salt, leaving behind interconnected pores. Another method is the use of gas-foaming agents, where gas bubbles generated during scaffold fabrication create voids upon the solidification of the polymer [25].

- **3D Bioprinting/Additive Manufacturing:** 3D printing or additive manufacturing techniques allow the precise layer-by-layer deposition of materials to create complex 3D structures. Various 3D printing methods are employed, including stereolithography, fused deposition modeling, and selective laser sintering. These techniques enable the fabrication of scaffolds with intricate geometries and controlled pore size and architecture, tailored to specific tissue needs [26, 27, 28, 29]. Types of bioprinting is shown in Figure 5.2.

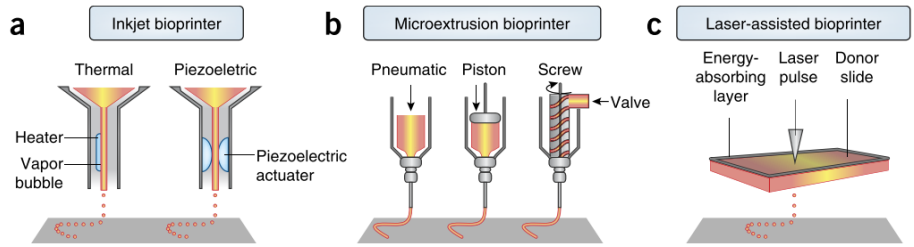

Figure 5.2. Types of bioprinting. Adapted with permission from [26].

- **Self-Assembly:** Self-assembly techniques exploit the inherent properties of certain materials to form organized structures without external intervention (Figure 5.3). For example, peptides or proteins with self-assembling properties can be designed to spontaneously form nanofibrous scaffolds when exposed to physiological conditions. Self-assembly techniques offer simplicity and reproducibility in scaffold fabrication [30, 31] .

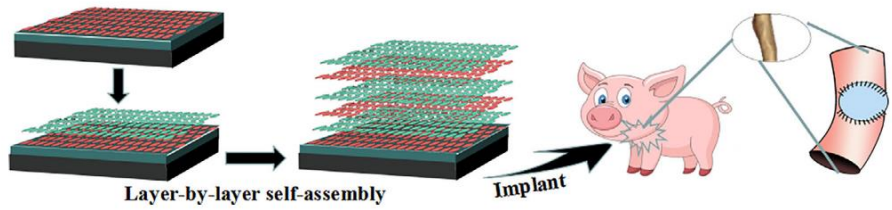

Figure 5.3. Layer-by-layer scaffold assembly. Adapted with permission from [30].

- **Solvent Casting/Particulate Leaching:** Solvent casting involves the creation of a polymer solution or suspension that is cast into a mold and then solidified by solvent evaporation or crosslinking. Particulate

leaching involves incorporating particulate materials, such as sugar or salt particles, into the polymer solution, followed by their removal to generate pores. This technique allows the production of scaffolds with controlled porosity and pore size distribution [32].

- **Electrospun Fiber Meshes:** In addition to electrospinning, electrospun fiber meshes can be created by using various collectors or mandrels with specific geometries. By manipulating the collector or mandrel design, such as using rotating drums or cylinders, fibers can be collected in aligned or oriented patterns, mimicking the organization of native tissues such as muscle or nerve. [33, 34, 35]
- **Decellularized Tissue Scaffolds:** Decellularization involves removing cellular components from native tissues, leaving behind the extracellular matrix (ECM). These decellularized tissue scaffolds retain the structural and biochemical cues of the native tissue and can serve as scaffolds for cell seeding and tissue regeneration. This technique is particularly useful for complex tissues such as heart valves or blood vessels [36, 37].

5.3. Electrospun scaffolds for tissue engineering of vascular grafts

Every year, around 1.4 million patients in the United States require arterial prostheses due to vascular issues. Unfortunately, the current options available for replacing these vascular grafts have shown limited success in clinical applications, amounting to a cost exceeding US$25 billion [38]. Notably, diseases affecting small and medium-sized blood vessels contribute significantly to mortality rates [39]. Atherosclerosis, a severe condition, leads to plaque buildup beneath the intimal layer, reducing the available cross-sectional area for blood circulation. This results in diminished blood flow to tissues downstream of the plaque [40]. Ultimately, patients often need cardiac and peripheral bypass surgeries, involving the replacement of a section of blood vessels.

In cases like "blue baby syndrome," where only one of an infant's ventricles functions properly, a procedure called the "Fontan operation" becomes imperative [41]. This operation requires the creation of an engineered blood vessel to link the right pulmonary artery with the inferior vena cava. This redirection allows deoxygenated blood to bypass the heart and directly reach the lungs. Similarly, conditions such as coronary artery diseases and peripheral vascular diseases frequently necessitate the replacement of damaged native blood vessels [42].

Vascular scaffolds specifically focus on creating scaffolds that mimic blood vessels. They are designed to support the growth and organization of endothelial cells, smooth muscle cells, and other cell types found in blood vessel walls (Figure 5.4). The electrospun nanofiber-based vascular scaffolds can provide mechanical support and serve as a template for the formation of new blood vessels in tissue engineering applications.

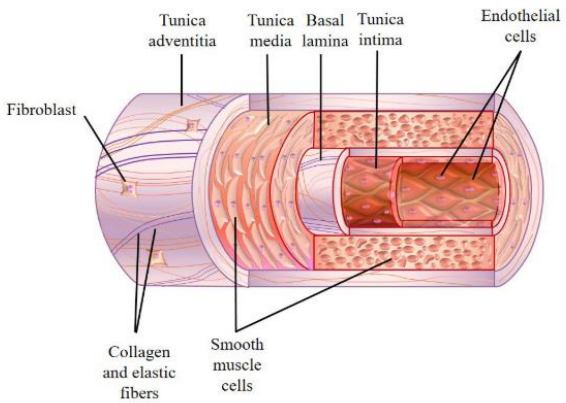

Figure 5.4. General structure of a blood vessel (Ng 2018)

Currently, the available choices for these types of transplants include autologous grafts (e.g., coronary artery bypass graft using the patient's own mammary arteries and saphenous veins), allografts (from donors or cadavers), xenografts (like bovine or porcine pulmonary valve conduits), artificial prostheses, or synthetic vascular grafts constructed from materials such as expanded polytetrafluoroethylene

(ePTFE) and polyethylene terephthalate (PET) [44]. Limitation of commercially available vascular grafts can be listed as:

- Thrombosis: All types of vascular grafts can be prone to blood clot formation (thrombosis), which can lead to graft failure and potentially serious complications.
- Aneurysm Formation: Some grafts can lead to aneurysm formation due to various factors such as porosity, graft material, and blood flow dynamics.
- Immune Reactions: Biologic grafts, allografts, and xenografts (grafts from animals) can trigger immune responses, potentially leading to graft rejection.
- Compliance Mismatch: Synthetic grafts may have different compliance (elasticity) compared to natural blood vessels, which can impact blood flow dynamics and lead to complications.
- Size Limitations: Some grafts may not be suitable for very small or very large vessels, limiting their application. Although these materials are available and provide clinical efficiency, they have a low ratio of patency when employed for small diameter blood vessels (<6 mm). The reported patency rates are 40% after six months and 25% after three years [45].

Electrospun nanofibers for tissue engineering, specifically for vascular scaffolds, hold great potential in advancing regenerative medicine and providing solutions for tissue and organ replacement therapies. According to the literature search done by Leal et al, electrospinning holds 49% of the entire vascular tissue engineering studies [46]. Several efforts have been undertaken to create scaffolds for blood vessels using diverse strategies and polymers. Figure 5.5 shows some of the frequently utilized polymers in these attempts. Researchers continue to explore and refine this technique to develop functional and clinically relevant tissue-engineered constructs.

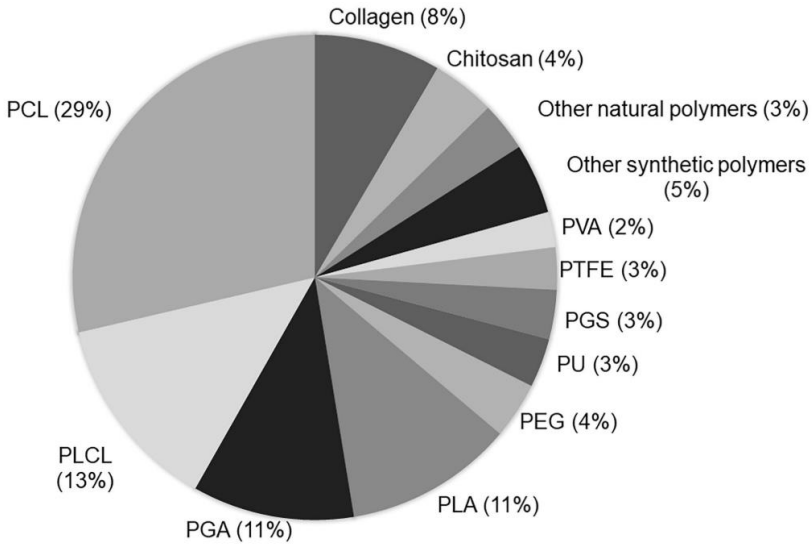

Figure 5.5. Polymers used in vascular tissue engineering. Adapted with permission from [46].

5.1.1. Tropoelastin (The Building block Elastin) nanofibers and blood vessel tissue engineering

Elastic fibers exist within the extracellular matrix of connective tissue, furnishing tissues with the capacity to undergo repetitive and reversible deformation while maintaining resilience. It stands out as one of the most hydrophobic proteins known, with more than 75% of its sequence comprising only four nonpolar amino acids: glycine, valine, alanine, and proline. Elastin is widespread in numerous tissues, constituting a significant portion of their composition. For instance, it constitutes up to 57% of the aorta, 50% of elastic ligaments, 32% of major vascular vessels, 7% of lung tissue, and contributes 5% to the overall dry weight of the skin [47]. These fibers exhibit diverse arrangements based on the tissue type: forming compact, cord-like networks in the lung, skin, and ligaments; adopting thin, concentric layers in blood vessels; and creating expansive, three-dimensional

honeycomb patterns in elastic cartilage [48]. Presence of elastic fibers provides these tissues with the ability to rebound and recover. (Figure 5.6) Mechanically, elastic fibers operate akin to a collection of entropic springs. These fibers store a fraction of mechanical energy while the heart undergoes systolic expansion, subsequently releasing this stored energy during diastole. This released energy serves to facilitate the continuous flow of blood.

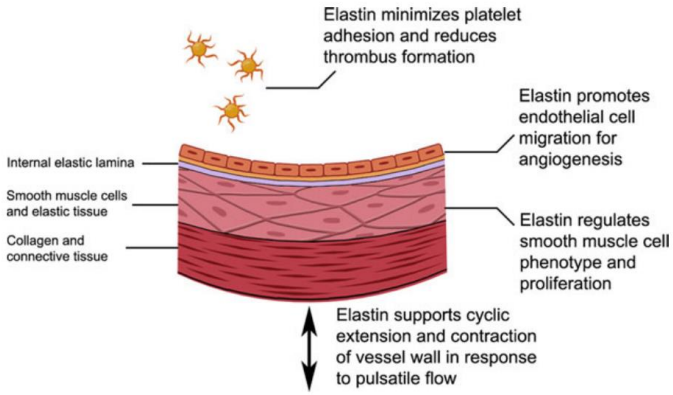

Figure 5.6. Schematic for the mechanical and biological roles of elastin in natural blood vessels. Adapted with permission [43].

Elastin is an insoluble protein composed of the soluble monomer *tropoelastin* [49]. Elastin-forming cells, such as smooth muscle cells (SMCs), endothelial cells, and fibroblasts, produce tropoelastin in the form of a protein weighing around 60 to 70 kDa [50, 51]. A tropoelastin monomer is illustrated in Figure 5.7.

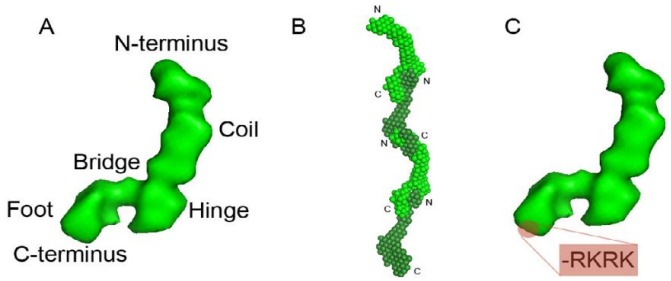

Figure 5.7. a) Structural features of the tropoelastin monomer; b) cell interactive C- terminal sequence – RKRK; and c) assembly model showing the N- to C-terminal interaction. Adapted with permission from [52].

The production of elastin fibers is most prominent in the initial stages of development, particularly in the late fetal and early neonatal periods [53, 54]. Tropoelastin, beyond its traditional function in providing elasticity as the building block for the ECM protein elastin, has now been recognized for its crucial involvement in cell attachment, spreading, signaling, and tissue regeneration [56]. During elastin synthesis, cells within the ECM come into contact with tropoelastin. However, in mature tissue where elastogenesis is limited, the levels of tropoelastin decrease accordingly. Nevertheless, injury to mature elastic tissue leads to the release of proteolytic elastin fragments, which retain functional cell-interacting sequences found in tropoelastin. Consequently, tropoelastin plays a signaling role, promoting angiogenesis (the growth of blood vessels from the existing vasculature) in vivo. It remains unclear whether endothelial cells directly respond to these elastic sequences or if the effects are mediated indirectly. The angiogenic potential of tropoelastin was initially identified in an in vivo study that employed tropoelastin within a dermal regeneration template. Furthermore, recent evidence shows that heat-stabilized pure tropoelastin implants enhance the healing of full-thickness wounds in pigs. This improvement is accompanied by evidence of perfusion in pink tissue, leading to enhanced dermal growth and accelerated re-epithelialization. These consistent yet not fully understood findings from multiple animal models highlight the role of tropoelastin as a promoter of blood vessel formation in vivo. [56]

5.4. Fabrication and 3D rendering of PGS/TE scaffolds, what information do we get from 3D reconstruction? (This Study)

5.2.1. Fabrication of PGS/TE scaffolds (This Study)

In our work, multiphoton microscopy (Leica SP8 Dive) was used to examine the microstructures of the heat-stabilized scaffolds composed of TE and PGS (shown in Figure 5.8). In the case of TE30, a combination of TE aggregates and fibers was found within a PGS matrix. For TE50, TE fibers were uniformly

dispersed throughout a PGS matrix, with a denser fiber network compared to TE30. The structure of TE70 was entirely fibrous, with both TE and PGS present in the same fibers, and a notable concentration of the PGS component at the interconnecting fiber regions. A similar fibrous network structure was evident in TE100 as well. The findings from both SEM and multiphoton analysis revealed that electrospun TE-PGS scaffolds exhibit a range of microstructures, varying from matrices where fibers are embedded in a non-porous manner to complete fibrous networks. The specific microstructure observed is contingent on the ratio of TE to PGS. [57]

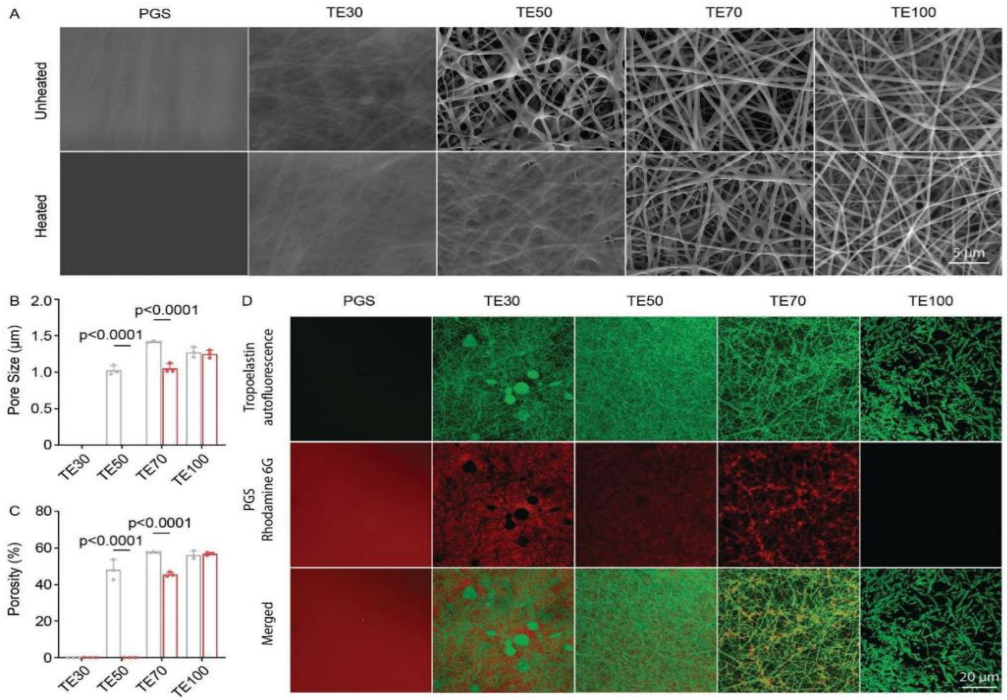

Figure 5.8. Prepared electrospun PGS/TE scaffolds a) SEM images of heated and unheated fibrous mats b) average pore size of produced scaffolds at different ratios c) average porosity of the scaffolds. d) multiphoton microscopy images of cells through the scaffold at different ratios. Adapted with permission from [57]

Creating a 3D rendering of nanofibrous multiphoton microscopy images involves visualizing intricate structures and details captured using advanced microscopy techniques. The images are obtained from the nanofibrous multiphoton microscopy images using a suitable microscope equipped with multiphoton capabilities. This technique allows deeper imaging within samples, such as biological tissues, by using near-infrared light.

3D rendering usually involves four main steps:

- Image Segmentation: Segment the nanofibrous structures from the background using image processing methods. This could involve thresholding, edge detection, or machine learning-based techniques to isolate the nanofibers.
- Image Reconstruction: For each plane of the microscopy data, create a 2D image stack that represents the nanofibers in that plane. These 2D slices will form the basis for constructing the 3D rendering.
- Volume Rendering: Utilize software tools capable of volume rendering, such as ImageJ, Fiji, Imaris, or specialized microscopy software provided by the microscope manufacturer. These tools allow you to stack the 2D slices and render them into a 3D structure.
- Visualization: Interact with the 3D-rendered structure using software tools. Rotate, zoom, and pan to explore the nanofibrous structure from different angles.

In order to make 3D rendering of TE70 and TE50, we used Dragonfly (version 2021.1, accessed from July 2021 to November 2021) The first step was separating the images of TE and PGS (50:50) taken by different detectors (Figure a and b). We used ImageJ software with the Bio-Format plugin in order to process the images.. In this case, there were 50 slices of microscopy images of TE50 and they were separated as 25 (PGS) and 25(TE) slices. From Figure 5.8a and b, we made one segmented image adjusted manually (Figure 5.8c and d), then the same conditions were applied to the rest 49 slices automatically. Finally, all the images were stacked together in order to visualize the 3D image (Figure

5.8d). We made several "imaginary" cuts in order to investigate the internal morphology of the overall structure (Figure 5.8f), as well as the cross-section (Figure 5.8g). TE50 showed homogeneously distributed TE fibers dispersed throughout a PGS matrix with a higher fiber network density Same process for TE50 was tried for 90 slices as well. Similar results were obtained. This ratio of PGS:TE seemed to give homogenous distribution consistently.

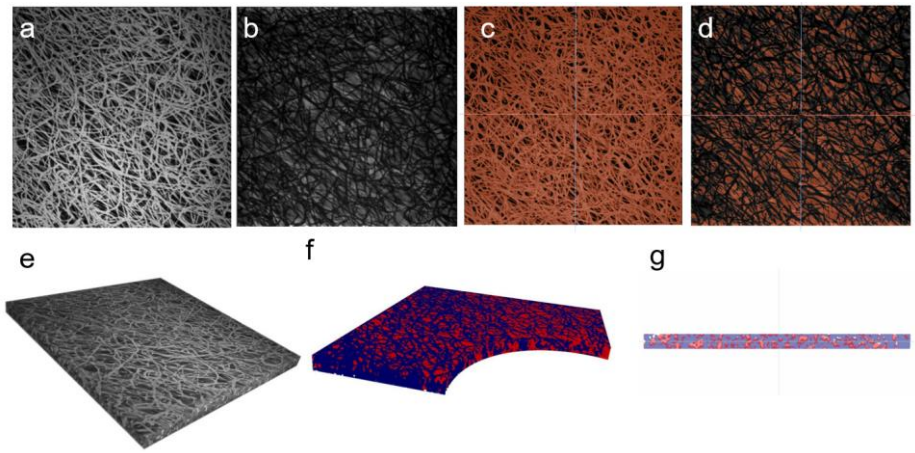

Figure 5.9. a) multiphoton microscope image of TE fibers b) multiphoton microscope image of PSG matrix. c) segmented image of TE fibers d) segmented image of PGS matrix. e) microscope images combined to create a 3D object f) segmented images of TE and PGS combined (showing the internal structure) g) cross-section of the stacked images

The same 3D rendering processing conditions were applied to TE70 images that had 128 slices (Figure 5.10). In this case, inhomogeneity and aggregates of PGS were observed throughout the mat. We also made an area determination study. (Figure 5.11) Region of interest was determined for each slice. The results suggested that TE/PGS ratios in the scaffold were not the same as in the solution. This might be because unstable electrospinning causes some material loss.

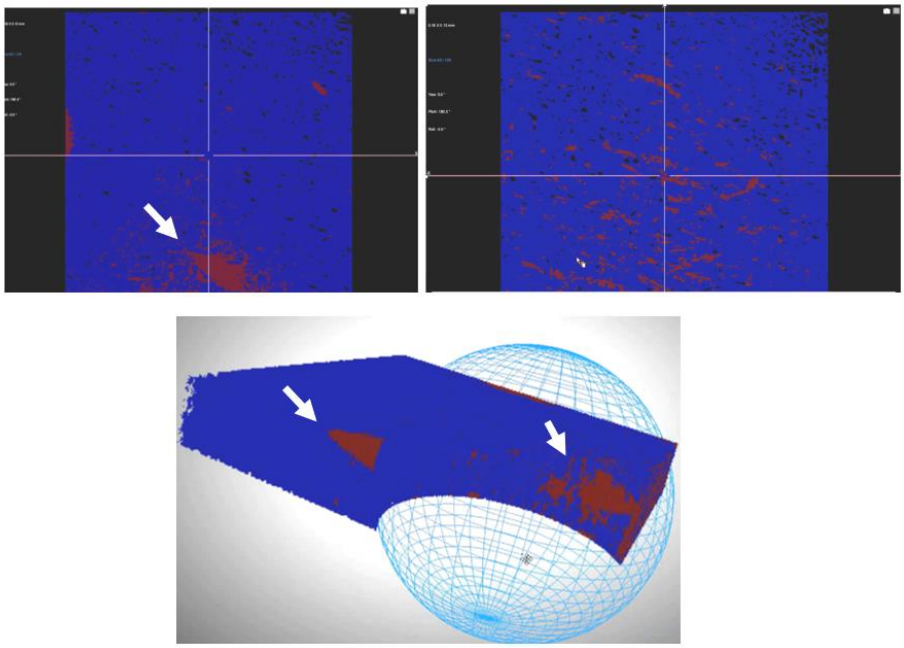

Figure 5.10. 3D rendering of 70TE scaffolds. White arrows show the accumulated PGS regions.

a

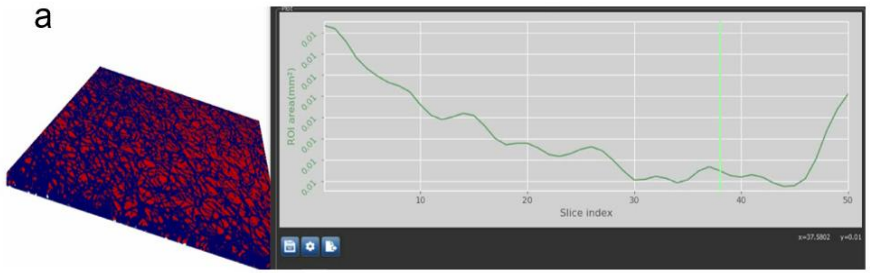

b

Slice	ROI Area(mm²)
1	0.0141
2	0.0141
3	0.0141
4	0.0140
5	0.0139
6	0.0139
7	0.0139
8	0.0138
9	0.0138
10	0.0138
11	0.0137
12	0.0137
13	0.0137
14	0.0137
15	0.0137
16	0.0137
17	0.0136
18	0.0136
19	0.0136
20	0.0136
21	0.0136
22	0.0135
23	0.0135
24	0.0135
25	0.0135
26	0.0136
27	0.0135
28	0.0135
⋮	
43	0.0134
44	0.0134
45	0.0134
46	0.0134
47	0.0135
48	0.0136
49	0.0137
50	0.0138

c

50TE_1

50 slices	TE ROI AREA (mm^2)	PGS ROI AREA (mm^2)	TE/PGS
Average	0.014	0.005	2.890

50TE_2

90 slices	TE ROI AREA (mm^2)	PGS ROI AREA (mm^2)	TE/PGS
Average	0.006	0.007	0.743

70TE_1

128 slices	TE ROI AREA (mm^2)	PGS ROI AREA (mm^2)	TE/PGS
Average	0.015	0.001	19.295

Figure 5.11. a) 3D object ROI area determination for one of the components. b) Example of exported values from the graph. This was done for both components (TE and PGS) c) comparison between the mats and TE/PGS ratios.

5.5. Mechanical simulation of electrospun mats, why is it important, future works

Electrospun mats are commonly used in various applications, including tissue engineering, filtration, and drug delivery. The mechanical properties of these mats, such as stiffness, elasticity, and strength, play a crucial role in their performance. Mechanical simulation allows researchers and engineers to predict these properties without the need for extensive experimental testing, saving time and resources. By simulating the mechanical behavior of electrospun mats, researchers can explore different design parameters, such as fiber alignment, density, and composition, to optimize the material's performance for specific applications. This helps in tailoring the material's properties to meet desired requirements. Simulations can guide the manufacturing process of electrospun mats by predicting how different processing parameters, such as electric field strength, solution flow rate, and collector distance, affect the final mechanical properties. This helps in achieving consistent and desired material properties. Mechanical simulations can be used to validate experimental results. If the simulated mechanical properties closely match the experimental values, it provides confidence in the accuracy of the simulation model.

In our study, we simulated the tensile test behavior of randomly oriented 350 nm TE fibers that are about 350 nm. (This value was obtained experimentally) The fibers were drawn in SolidWorks and mechanically analyzed in Abacus software. Baldock et al. reported the young modulus of TE protein as 2.9 kPa [58]. We used this value in our simulations as the young modulus of one single fiber to simulate the overall young modulus of the TE mats. We did 2 mats, one with fewer fibers (Figure 5.12) and another with more fibers (Figure 5.13). This was the first attempt to see the stretching of TE nanofibers and stress concentration regions within the electrospun mat. However, in order to get meaningful stress-strain data, further investigation is required.

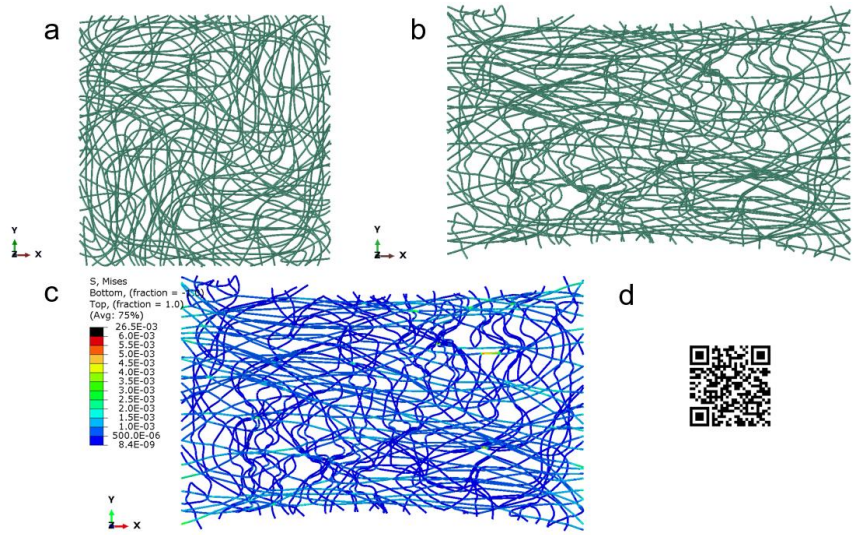

Figure 5.12. Tensile test simulation of fewer number of electrospun TE fibers.

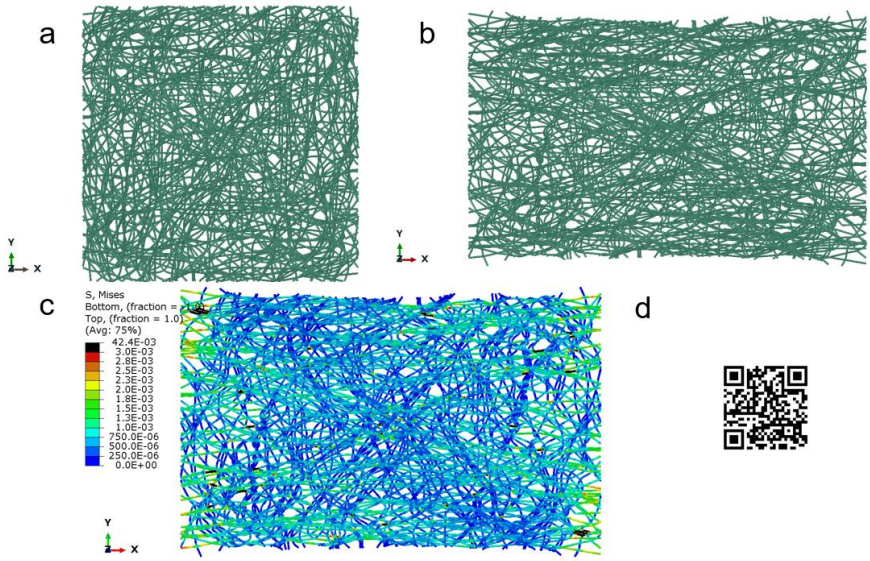

Figure 5.13. Tensile test simulation of electrospun TE fibers with more number of fibers.

5.6. Conclusions

In conclusion, the utilization of Dragonfly 3D rendering in this study has provided valuable insights into the structural characteristics of electrospun scaffolds and their correlation with real-world samples. The analysis of the 3D rendering results revealed a consistent and logical pattern that aligns with the physical attributes of the electrospun scaffolds.

One noteworthy observation from the 3D rendering analysis is the similarity in distribution patterns exhibited by the scaffolds produced using different parameters. Specifically, the scaffolds generated with a 50TE configuration consistently displayed the most uniform distribution for both components. This consistency across different samples underscores the reliability and accuracy of the Dragonfly 3D rendering method in capturing the inherent characteristics of the electrospun scaffolds.

However, it is crucial to acknowledge that the investigation into material distribution did reveal some intriguing and potentially important disparities. The utilization of image stacking and subsequent region of interest computations exposed a phenomenon where the material ratios within the 3D images deviated from the expected ratios in the original solution. This incongruity raises questions about the electrospinning process itself and suggests the presence of material loss during the fabrication process.

One plausible explanation for this discrepancy could be attributed to the instability of the electrospinning process. Electrospinning is a complex and multifaceted procedure influenced by numerous variables such as voltage, flow rate, and solution viscosity. The interaction of these factors may lead to non-uniformities in the deposition of materials on the collector, resulting in material loss that is not adequately captured by the 3D rendering method. The volatility of the electrospinning process could account for the observed disparities between the material ratios in the 3D images and the anticipated ratios in the solution.

In light of these findings, it is apparent that while Dragonfly 3D rendering offers a comprehensive visualization of the electrospun scaffolds' structures, it may not provide an exhaustive account of the material distribution, particularly when facing intricate processing techniques like electrospinning. Therefore, future research endeavors should not only continue to leverage the power of advanced imaging techniques like Dragonfly 3D rendering but also collaborate with other analytical methods to comprehensively capture the intricacies of material distribution during fabrication.

5.5. References

[1] Keirouz, A., Chung, M., Kwon, J., Fortunato, G., & Radacsi, N. (2020). 2D and 3D electrospinning technologies for the fabrication of nanofibrous scaffolds for skin tissue engineering: A review. *Wiley Interdisciplinary Reviews: Nanomedicine and Nanobiotechnology*, *12*(4), 1–32. https://doi.org/10.1002/wnan.1626

[2] Rahmati, M., Mills, D. K., Urbanska, A. M., Saeb, M. R., Venugopal, J. R., Ramakrishna, S., & Mozafari, M. (2021). Electrospinning for tissue engineering applications. *Progress in Materials Science*, *117*(July 2020), 100721. https://doi.org/10.1016/j.pmatsci.2020.100721

[3] Karamanos, N. K., Theocharis, A. D., Piperigkou, Z., Manou, D., Passi, A., Skandalis, S. S., Vynios, D. H., Orian-Rousseau, V., Ricard-Blum, S., Schmelzer, C. E. H., Duca, L., Durbeej, M., Afratis, N. A., Troeberg, L., Franchi, M., Masola, V., & Onisto, M. (2021). A guide to the composition and functions of the extracellular matrix. *FEBS Journal*, *288*(24), 6850–6912. https://doi.org/10.1111/febs.15776

[4] Chaudhuri, O., Cooper-White, J., Janmey, P. A., Mooney, D. J., & Shenoy, V. B. (2020). Effects of extracellular matrix viscoelasticity on cellular behaviour. *Nature*, *584*(7822), 535–546. https://doi.org/10.1038/s41586-020-2612-2

[5] Hosseini, M., & Shafiee, A. (2021). Engineering Bioactive Scaffolds for Skin Regeneration. *Small*, *17*(41). https://doi.org/10.1002/smll.202101384

[6] Lin, W., Chen, M., Qu, T., Li, J., & Man, Y. (2020). Three-dimensional electrospun nanofibrous scaffolds for bone tissue engineering. *Journal of Biomedical Materials Research Part B: Applied Biomaterials*, *108*(4), 1311–1321. https://doi.org/https://doi.org/10.1002/jbm.b.34479

[7] Barbosa, F., Ferreira, F. C., & Silva, J. C. (2022). Piezoelectric Electrospun Fibrous Scaffolds for Bone, Articular Cartilage and Osteochondral Tissue Engineering. *International Journal of Molecular Sciences*, *23*(6). https://doi.org/10.3390/ijms23062907

[8] Babaie, A., Bakhshandeh, B., Abedi, A., Mohammadnejad, J., Shabani, I., Ardeshirylajimi, A., Reza Moosavi, S., Amini, J., & Tayebi, L. (2020). Synergistic effects of conductive PVA/PEDOT electrospun scaffolds and electrical stimulation for more effective neural tissue engineering. *European Polymer Journal*, *140*(June), 110051. https://doi.org/10.1016/j.eurpolymj.2020.110051

[9] Jia, W., Li, M., Kang, L., Gu, G., Guo, Z., & Chen, Z. (2019). Fabrication and Comprehensive Characterization of Biomimetic Extracellular Matrix Electrospun Scaffold for Vascular Tissue Engineering Applications. *Journal of Materials Science*, *54*(15), 10871–10883. https://doi.org/10.1007/s10853-019-03667-6

[10] Budak, K., Sogut, O., & Aydemir Sezer, U. (2020). A review on synthesis and biomedical applications of polyglycolic acid. *Journal of Polymer Research*, *27*(8). https://doi.org/10.1007/s10965-020-02187-1

[11] Zulkifli, Z., Tan, J. J., Ku Marsilla, K. I., Rusli, A., Abdullah, M. K., Shuib, R. K., Shafiq, M. D., & Abdul Hamid, Z. A. (2022). Shape memory poly (glycerol sebacate)-based electrospun fiber

scaffolds for tissue engineering applications: A review. *Journal of Applied Polymer Science*, *139*(22), 1–16. https://doi.org/10.1002/app.52272

[12] Liu, S., Qin, S., He, M., Zhou, D., Qin, Q., & Wang, H. (2020). Current applications of poly(lactic acid) composites in tissue engineering and drug delivery. *Composites Part B: Engineering*, *199*(June), 108238. https://doi.org/10.1016/j.compositesb.2020.108238

[13] Sanz-horta, R., Matesanz, A., Gallardo, A., Reinecke, H., Jorcano, J. L., Acedo, P., Velasco, D., & Elvira, C. (2023). *Technological advances in fibrin for tissue engineering*. https://doi.org/10.1177/20417314231190288

[14] Copes, F., Pien, N., Van Vlierberghe, S., Boccafoschi, F., & Mantovani, D. (2019). Collagen-based tissue engineering strategies for vascular medicine. *Frontiers in Bioengineering and Biotechnology*, *7*(JUL), 1–15. https://doi.org/10.3389/fbioe.2019.00166

[15] Cai, S., Wu, C., Yang, W., Liang, W., Yu, H., & Liu, L. (2020). Recent advance in surface modification for regulating cell adhesion and behaviors. *Nanotechnology Reviews*, *9*(1), 971–989. https://doi.org/10.1515/ntrev-2020-0076

[16] Chen, L., Liu, J., Guan, M., Zhou, T., Duan, X., & Xiang, Z. (2020). Growth factor and its polymer scaffold-based delivery system for cartilage tissue engineering. *International Journal of Nanomedicine*, *15*, 6097–6111. https://doi.org/10.2147/IJN.S249829

[17] Anjum, S., Rahman, F., Pandey, P., Arya, D. K., Alam, M., Rajinikanth, P. S., & Ao, Q. (2022). Electrospun Biomimetic Nanofibrous Scaffolds: A Promising Prospect for Bone Tissue Engineering and Regenerative Medicine. *International Journal of Molecular Sciences*, *23*(16). https://doi.org/10.3390/ijms23169206

[18] Zhang, Y., Zhang, M., Cheng, D., Xu, S., Du, C., Xie, L., & Zhao, W. (2022). Applications of electrospun scaffolds with enlarged pores in tissue engineering. *Biomaterials Science*, *10*(6), 1423–1447. https://doi.org/10.1039/d1bm01651b

[19] Ameer, J. M., Anil Kumar, P. R., & Kasoju, N. (2019). Strategies to tune electrospun scaffold porosity for effective cell response in tissue engineering. *Journal of Functional Biomaterials*, *10*(3), 1–21. https://doi.org/10.3390/jfb10030030

[20] Yuan, Z., Sheng, D., Jiang, L., Shafiq, M., Khan, A. ur R., Hashim, R., Chen, Y., Li, B., Xie, X., Chen, J., Morsi, Y., Mo, X., & Chen, S. (2022). Vascular Endothelial Growth Factor-Capturing Aligned Electrospun Polycaprolactone/Gelatin Nanofibers Promote Patellar Ligament Regeneration. *Acta Biomaterialia*, *140*, 233–246. https://doi.org/10.1016/j.actbio.2021.11.040

[21] Wang, R., de Kort, B. J., Smits, A. I. P. M., & Weiss, A. S. (2019). Elastin in Vascular Grafts. In *Tissue-Engineered Vascular Grafts*. https://doi.org/10.1007/978-3-319-71530-8_13-1

[22] Argentati, C., Morena, F., Tortorella, I., Bazzucchi, M., Porcellati, S., Emiliani, C., & Martino, S. (2019). Insight into mechanobiology: How stem cells feel mechanical forces and orchestrate

biological functions. *International Journal of Molecular Sciences*, *20*(21). https://doi.org/10.3390/ijms20215337

[23] Guimarães, C. F., Gasperini, L., Marques, A. P., & Reis, R. L. (2020). The stiffness of living tissues and its implications for tissue engineering. *Nature Reviews Materials*, *5*(5), 351–370. https://doi.org/10.1038/s41578-019-0169-1

[24] Wei, Q., Wang, S., Han, F., Wang, H., Zhang, W., Yu, Q., Liu, C., Ding, L., Wang, J., Yu, L., Zhu, C., Li, B., Bl, Cz, Cz, Cz, Qw, Sw, Fh, … Qw. (2021). Cellular modulation by the mechanical cues from biomaterials for tissue engineering. *Biomaterials Translational*, *2*(4), 323–342. https://doi.org/10.12336/biomatertransl.2021.04.001

[25] Mondrinos, M. J., Dembzynski, R., Lu, L., Byrapogu, V. K. C., Wootton, D. M., Lelkes, P. I., & Zhou, J. (2006). *Porogen-based solid freeform fabrication of polycaprolactone – calcium phosphate scaffolds for tissue engineering*. *27*, 4399–4408. https://doi.org/10.1016/j.biomaterials.2006.03.049

[26] Murphy, S. V., & Atala, A. (2014). 3D bioprinting of tissues and organs. *Nature Biotechnology*, *32*(8), 773–785. https://doi.org/10.1038/nbt.2958

[27] Klammert, U., Gbureck, U., Vorndran, E., Rödiger, J., Meyer-Marcotty, P., & Kübler, A. C. (2010). 3D powder printed calcium phosphate implants for reconstruction of cranial and maxillofacial defects. *Journal of Cranio-Maxillofacial Surgery*, *38*(8), 565–570. https://doi.org/10.1016/j.jcms.2010.01.009

[28] Wang, P., Sun, Y., Shi, X., Shen, H., Ning, H., & Liu, H. (2021). 3D printing of tissue engineering scaffolds: a focus on vascular regeneration. *Bio-Design and Manufacturing*. https://doi.org/10.1007/s42242-020-00109-0

[29] Kabirian, F., Ditkowski, B., Zamanian, A., Heying, R., & Mozafari, M. (2018). An innovative approach towards 3D-printed scaffolds for the next generation of tissue-engineered vascular grafts. *Materials Today: Proceedings*, *5*(7, Part 3), 15586–15594. https://doi.org/https://doi.org/10.1016/j.matpr.2018.04.167

[30] Zhang, J., Wang, D., Jiang, X., He, L., Fu, L., Zhao, Y., Wang, Y., Mo, H., & Shen, J. (2019). Multistructured vascular patches constructed via layer-by-layer self-assembly of heparin and chitosan for vascular tissue engineering applications. *Chemical Engineering Journal*, *370*(October 2018), 1057–1067. https://doi.org/10.1016/j.cej.2019.03.270

[31] Liu, H., Lin, M., Liu, X., Zhang, Y., Luo, Y., Pang, Y., Chen, H., Zhu, D., Zhong, X., Ma, S., Zhao, Y., Yang, Q., & Zhang, X. (2020). Doping bioactive elements into a collagen scaffold based

on synchronous self-assembly/mineralization for bone tissue engineering. *Bioactive Materials*, *5*(4), 844–858. https://doi.org/10.1016/j.bioactmat.2020.06.005

[32] Thadavirul, N., Pavasant, P., & Supaphol, P. (2013). *Development of polycaprolactone porous scaffolds by combining solvent casting , particulate leaching , and polymer leaching techniques for bone tisse engineering*. 3379–3392. https://doi.org/10.1002/jbm.a.35010

[33] Ferreira, P., Santos, P., Alves, P., Carvalho, M. P., Sá, K. D. De, Miguel, S. P., Correia, I. J., & Coimbra, P. (2017). Photocrosslinkable electrospun fi ber meshes for tissue engineering applications. *European Polymer Journal*, *97*(September), 210–219. https://doi.org/10.1016/j.eurpolymj.2017.10.018

[34] Ferreira, P., Santos, P., Alves, P., Carvalho, M. P., Sá, K. D. De, Miguel, S. P., Correia, I. J., & Coimbra, P. (2017). Photocrosslinkable electrospun fi ber meshes for tissue engineering applications. *European Polymer Journal*, *97*(September), 210–219. https://doi.org/10.1016/j.eurpolymj.2017.10.018

[35] Zhu, Y., Cao, Y., Pan, J., & Liu, Y. (2009). *Macro-Alignment of Electrospun Fibers For Vascular Tissue Engineering*. 508–516. https://doi.org/10.1002/jbm.b.31544

[36] Dahl, S. L. M., Koh, J., Prabhakar, V., & Niklason, L. E. (2003). *Decellularized Native and Engineered Arterial Scaffolds for Transplantation*. *12*(919), 659–666.

[37] Agmon, G., & Christman, K. L. (2016). Controlling stem cell behavior with decellularized extracellular matrix scaffolds. *Current Opinion in Solid State & Materials Science*, *20*(4), 193–201. https://doi.org/10.1016/j.cossms.2016.02.001

[38] Browning, M. B., Dempsey, D., Guiza, V., Becerra, S., Rivera, J., Russell, B., Höök, M., Clubb, F., Miller, M., Fossum, T., Dong, J. F., Bergeron, A. L., Hahn, M., & Cosgriff-Hernandez, E. (2012). Multilayer vascular grafts based on collagen-mimetic proteins. *Acta Biomaterialia*, *8*(3), 1010–1021. https://doi.org/10.1016/j.actbio.2011.11.015

[39] Bergmeister, H., Strobl, M., Grasl, C., Liska, R., & Schima, H. (2013). Tissue engineering of vascular grafts. *European Surgery - Acta Chirurgica Austriaca*, *45*(4), 187–193. https://doi.org/10.1007/s10353-013-0224-x

[40] Stegemann, J. P., Kaszuba, S. N., & Rowe, S. L. (2007). Review: Advances in vascular tissue engineering using protein-based biomaterials. *Tissue Engineering*, *13*(11), 2601–2613. https://doi.org/10.1089/ten.2007.0196

[41] Dolgin, E. (2011). Taking tissue engineering to heart. *Nature Medicine*, *17*(9), 1035. https://doi.org/10.1038/nm0911-1032

[42] Gong, Z., & Niklason, L. E. (2006). Blood Vessels Engineered from Human Cells. *Trends in Cardiovascular Medicine*, *16*(5), 153–156. https://doi.org/10.1016/j.tcm.2006.02.006

[43] Wang, R., de Kort, B. J., Smits, A. I. P. M., & Weiss, A. S. (2019). Elastin in Vascular Grafts. In *Tissue-Engineered Vascular Grafts*. https://doi.org/10.1007/978-3-319-71530-8_13-1

[44] Bouten, C. V. C., Dankers, P. Y. W., Driessen-Mol, A., Pedron, S., Brizard, A. M. A., & Baaijens, F. P. T. (2011). Substrates for cardiovascular tissue engineering. *Advanced Drug Delivery Reviews*, *63*(4), 221–241. https://doi.org/10.1016/j.addr.2011.01.007

[45] Sayers, R. D., Raptis, S., Berce, M., & Miller, J. H. (1998). Long-term results of femorotibial bypass with vein or polytetrafluoroethylene. *The British Journal of Surgery*, *85*(7), 934–938. https://doi.org/10.1046/j.1365-2168.1998.00765.x

[46] Leal, B. B. J., Wakabayashi, N., Oyama, K., Kamiya, H., Braghirolli, D. I., & Pranke, P. (2020). Vascular Tissue Engineering: Polymers and Methodologies for Small Caliber Vascular Grafts. *Frontiers in Cardiovascular Medicine*, *7*, 592361. https://doi.org/10.3389/fcvm.2020.592361

[47] Wise, S. G., Mithieux, S. M., & Weiss, A. S. (2009). Engineered tropoelastin and elastin-based biomaterials. In *Advances in protein chemistry and structural biology* (First edit, Vol. 78, Issue 09). Elsevier. https://doi.org/10.1016/s1876-1623(08)78001-5

[48] Vrhovski, B., & Weiss, A. S. (1998). Biochemistry of tropoelastin. *European Journal of Biochemistry*, *258*(1), 1–18. https://doi.org/10.1046/j.1432-1327.1998.2580001.x

[49] Indik, Z., Abrams, W. R., Kucich, U., Gibson, C. W., Mecham, R. P., & Rosenbloom, J. (1990). Production of recombinant human tropoelastin: Characterization and demonstration of immunologic and chemotactic activity. *Archives of Biochemistry and Biophysics*, *280*(1), 80–86. https://doi.org/10.1016/0003-9861(90)90521-Y

[50] Pasquali-Ronchetti, I., Baccarani-Contri, M., Fornieri, C., Mori, G., & Quaglino, D. (1993). Structure and composition of the elastin fibre in normal and pathological conditions. *Micron*, *24*(1), 75–89. https://doi.org/10.1016/0968-4328(93)90016-T

[51] Debelle, L., & Tamburro, A. M. (1999). Elastin: Molecular description and function. *International Journal of Biochemistry and Cell Biology*, *31*(2), 261–272. https://doi.org/10.1016/S1357-2725(98)00098-3

[52] Wise, S. G., Yeo, G. C., Hiob, M. A., Rnjak-Kovacina, J., Kaplan, D. L., Ng, M. K. C., & Weiss, A. S. (2014). Tropoelastin: A versatile, bioactive assembly module. *Acta Biomaterialia*, *10*(4), 1532–1541. https://doi.org/10.1016/j.actbio.2013.08.003

[53] Parks, W. C., Secrist, h., Wu, L. C., & Mecham, R. P. (1988). Developmental regulation of tropoelastin isoforms. *Journal of Biological Chemistry*, *263*(9), 4416–4423. https://doi.org/10.1016/s0021-9258(18)68942-2

[54] Swee, M. H., Parks, W. C., & Pierce, R. A. (1995). Developmental regulation of elastin production: Expression of tropoelastin pre-mRNA persists after down-regulation of steady-state mRNA levels. *Journal of Biological Chemistry*, *270*(25), 14899–14906. https://doi.org/10.1074/jbc.270.25.14899

[55] Wise, S. G., Mithieux, S. M., & Weiss, A. S. (2009). Engineered tropoelastin and elastin-based biomaterials. In *Advances in protein chemistry and structural biology* (First edit, Vol. 78, Issue 09). Elsevier. https://doi.org/10.1016/s1876-1623(08)78001-5

[56] Aghaei-Ghareh-Bolagh, B., Mukherjee, S., Lockley, K. M., Mithieux, S. M., Wang, Z., Emmerson, S., Darzi, S., Gargett, C. E., & Weiss, A. S. (2020). A novel tropoelastin-based resorbable surgical mesh for pelvic organ prolapse repair. *Materials Today Bio*, *8*(October), 100081. https://doi.org/10.1016/j.mtbio.2020.100081

[57] Wang, Z., Mithieux, S. M., Vindin, H., Wang, Y., Zhang, M., Liu, L., Zbinden, J., Blum, K. M., Yi, T., Matsuzaki, Y., Oveissi, F., Akdemir, R., Lockley, K. M., Zhang, L., Ma, K., Guan, J., Waterhouse, A., Pham, N. T. H., Hawkett, B. S., … Weiss, A. S. (2022). Rapid Regeneration of a Neoartery with Elastic Lamellae. *Advanced Materials*, *34*(47). https://doi.org/10.1002/adma.202205614

[58] Baldock, C., Oberhauser, A. F., Ma, L., Lammie, D., Siegler, V., Mithieux, S. M., Tu, Y., Chow, J. Y. H., Suleman, F., Malfois, M., Rogers, S., Guo, L., Irving, T. C., Wess, T. J., & Weiss, A. S. (2011). Shape of tropoelastin, the highly extensible protein that controls human tissue elasticity. *Proceedings of the National Academy of Sciences of the United States of America*, *108*(11), 4322–4327. https://doi.org/10.1073/pnas.1014280108

General Conclusions

To conclude, this study has introduced an innovative method to precisely compute the internal porosity of individual polymeric nanofibers. By combining SEM and AFM imaging, we've developed a technique that determines cross-sectional areas before and after thermal annealing, offering localized insight into fiber porosity. This localized approach differs from the pycnometry-based method that provides a global porosity value, which can be valuable in specific applications.

Applying our method to analyze PCL and PS fibers has yielded valuable outcomes. PCL fibers exhibit compactness, implying the absence of internal voids, while PS fibers show approximately 50% porosity, highlighting significant internal voids. This detailed porosity information can guide material design for various applications. Comparing our microscopy-based method with pycnometry-based approach validates our method's reliability. Applying these techniques to PS electrospun fibers demonstrates that the microscopy-based approach offers a local view of fiber porosity distribution, particularly useful for understanding individual fiber porosity distribution. Insights gained can drive tailored material development. The study also introduces a new method for characterizing tensile properties of electrospun nanofibers in a practical way. This method's robustness and consistency across varying conditions highlight its potential as a standard in nanofiber research. Utilizing Dragonfly 3D rendering offers insights into electrospun scaffold structures. In our work, consistent distribution patterns are observed, notably with the 50TE configuration. Discrepancies in material distribution within 3D images compared to original solutions raise questions about the electrospinning process and possible material loss.

UNIVERSITAT
ROVIRA i VIRGILI